International Journal of Photoenergy

Solid-State Lighting with High Brightness, High Efficiency, and Low Cost

Guest Editors: Ray-Hua Horng, Kei May Lau, Hao-Chung Kuo, and Nelson Tansu

Solid-State Lighting with High Brightness, High Efficiency, and Low Cost

International Journal of Photoenergy

Solid-State Lighting with High Brightness, High Efficiency, and Low Cost

Guest Editors: Ray-Hua Horng, Kei May Lau, Hao-Chung Kuo, and Nelson Tansu

Editorial Board

Contents

Hindawi Publishing Corporation
International Journal of Photoenergy
Volume 2014, Article ID 278263, 3 pages
http://dx.doi.org/10.1155/2014/278263

Editorial

Solid-State Lighting with High Brightness, High Efficiency, and Low Cost

Ray-Hua Horng,[1] Kei May Lau,[2] Hao-Chung Kuo,[3] and Nelson Tansu[4]

[1] *Graduate Institute of Precision Engineering, National Chung Hsing University, Taichung 402, Taiwan*
[2] *Photonics Technology Center, Department of Electronic and Computer Engineering, Hong Kong University of Science and Technology, Clear Water Bay, Kowloon, Hong Kong*
[3] *Department of Photonics and Institute of Electro-Optical Engineering, National Chiao Tung University, Hsinchu 30010, Taiwan*
[4] *Center for Photonics and Nanoelectronics, Department of Electrical and Computer Engineering, Lehigh University, Bethlehem, PA 18015, USA*

Correspondence should be addressed to Ray-Hua Horng; huahorng@nchu.edu.tw and Nelson Tansu; tansu@lehigh.edu

Received 21 August 2014; Accepted 21 August 2014; Published 7 September 2014

In order to achieve the advanced lighting with the energy-saving and environmental-protecting capabilities, the technologies of solid-state lighting have been developed rapidly. In all solid-state lighting applications, light-emitting diode (LED) is the most popular technique due to its advantages of small volume, long lifetime, high reliability, low power consumption, and nonpollution.

The progress in solid-state lighting has been driven by innovations in wide range of technologies in materials, devices, and novel concepts [1–5]. In addition to the progress in visible InGaN-based light-emitting diodes (LEDs) based on III-nitride based semiconductor, the improved understanding in the AlGaN-based LEDs [6, 7] has also resulted in new understanding on the device physics of III-nitride semiconductor physics which in turn results in new concept and approaches to handle the limitation in the fields of nitride-based LEDs. Several of these concepts have resulted in new approaches to suppress the charge separation effect [8, 9], carrier leakage process [10–14], light extraction issue [15–17], and Auger processes [18–21] in the InGaN-based LEDs. The improved understanding on the fundamental properties of InGaN as active regions has resulted in the ability to advance this field into practical technologies being implemented in the daily technologies used in our society.

In this special issue, the editors attempt to bring some of the recent advances in the field of device engineering and applications of III-nitride based LEDs with the goals of achieving high brightness and low-cost approaches. Up to now, the nitride-based materials are maturely developed to apply for LED applications. However, to obtain the LED devices with high brightness, high efficiency, and low cost, there are still some techniques to be improved, especially for the nitride-epilayer growth with low defect density and device fabrication with high heat dissipation.

In this special issue, there are seven contributed papers to discuss these issues from the LED epilayer quality to the high efficiency package. The implementation and test of LED-based lamp for lighthouse application were discussed at the system level (*"Implementation and test of a LED-based lamp for a lighthouse"* by L. Mercatelli et al.). Such applications of LED in lighthouse have different requirement from those used in general illumination. The important new application from LED will broaden the new potential innovations required in enabling this technology to be suitable for implementation.

The investigation of novel phosphor material for converting blue/UV LEDs into white LEDs was also discussed specifically for investigating the color rendering index and its thermal stability (*"Color rendering index thermal stability improvement of glass-based phosphor-converted white light-emitting diodes for solid-state lighting"* by C.-C. Tsai).

Phosphor-based materials are important, and the understanding of its stability at high temperature for ensuring stability in color rendering index in white LEDs is crucial for low-cost white LED.

The use of ZnO:YAG based metal-insulator-sem-iconductor (MIS) white LEDs was also reported with various insulator designs ("*Low-cost ZnO:YAG-based metal-insulator-semiconductor white light-emitting diodes with various insulators*" by L.-C. Chen et al.). Specifically, the authors investigated the effect of various thicknesses of the silica and MnZnO based insulator on the MIS structure for LED applications.

Recent works have shown the importance of growing GaN-based LEDs on nanopatterned substrates [22–24], and the two related works were reported in this special issue ("*Performance of InGaN light-emitting diodes fabricated on patterned sapphire substrates with modified top-tip cone shapes*" by H.-H. Hsueh et al. and "*Void shapes controlled by using interruption-free epitaxial lateral overgrowth of GaN films on patterned SiO_2 AlN/sapphire template*" by Y.-A. Chen et al.). The use of shape-engineered patterned sapphire substrate and patterned silica mask for achieving improved epitaxy in GaN LEDs was reported ("*Performance of InGaN light-emitting diodes fabricated on patterned sapphire substrates with modified top-tip cone shapes*" by H.-H. Hsueh et al. and "*Void shapes controlled by using interruption-free epitaxial lateral overgrowth of GaN films on patterned SiO_2 AlN/sapphire template*" by Y.-A. Chen et al.). The thermal management is an important issue for high power LEDs, and the use of diamond-like carbon heat-spreading layer was reported ("*Thermal characteristics of InGaN/GaN flip-chip light emitting diodes with diamond-like carbon heat-spreading layers*" by P.-Y. Tsai et al.).

The investigations of high-voltage LEDs in flip chip configurations have tremendous interests and potential impact for enabling reduced droop operation up to high power operation ("*Efficiency and droop improvement in GaN-based high-voltage flip chip LEDs*" by Y.-C. Chiang et al.). The use of high voltage design enables the low current density while the total output power can be accomplished. The droop issue has been one of the key limitations in LED development for low-cost applications, and the high voltage LED has the potential for addressing this droop issue from the circuit and systems level innovation in new solid-state lighting device systems.

We hope that the special issue will be of value for the research community in particular in driving this important topic on solid-state lighting. The great potential and promise of solid-state lighting are coming to reality, and the drive for innovation for achieving high brightness at low cost is important for enabling market penetration of this technology.

Ray-Hua Horng
Kei May Lau
Hao-Chung Kuo
Nelson Tansu

References

[1] M. H. Crawford, "LEDs for solid-state lighting: performance challenges and recent advances," *IEEE Journal on Selected Topics in Quantum Electronics*, vol. 15, no. 4, pp. 1028–1040, 2009.

[2] N. Tansu, H. Zhao, G. Liu et al., "III-nitride photonics," *IEEE Photonics Journal*, vol. 2, no. 2, pp. 236–243, 2010.

[3] J. J. Wierer, J. Y. Tsao, and D. S. Sizov, "Comparison between blue lasers and light-emitting diodes for future solid-state lighting," *Laser & Photonics Reviews*, vol. 7, pp. 963–993, 2013.

[4] N. Tansu, "Photonics—advances in fundamental sciences and engineering technologies of light," *Photonics*, vol. 1, no. 1, pp. 1–8, 2014.

[5] J. Han and A. V. Nurmikko, "Advances in AlGaInN blue and ultraviolet light emitters," *IEEE Journal on Selected Topics in Quantum Electronics*, vol. 8, no. 2, pp. 289–297, 2002.

[6] J. Zhang and N. Tansu, "Engineering of AlGaN-Delta-GaN quantum wells gain media for mid- and deep-ultraviolet lasers," *IEEE Photonics Journal*, vol. 5, no. 2, Article ID 2600209, 2013.

[7] Y. Taniyasu and M. Kasu, "Polarization property of deep-ultraviolet light emission from C-plane AlN/GaN short-period superlattices," *Applied Physics Letters*, vol. 99, no. 25, Article ID 251112, 2011.

[8] D. F. Feezell, J. S. Speck, S. P. Denbaars, and S. Nakamura, "Semipolar ($20^{-}2^{-}1$) InGaN/GaN light-emitting diodes for high-efficiency solid-state lighting," *Journal of Display Technology*, vol. 9, no. 4, pp. 190–198, 2013.

[9] H. P. Zhao, G. Y. Liu, J. Zhang, J. D. Poplawsky, V. Dierolf, and N. Tansu, "Approaches for high internal quantum efficiency green InGaN light-emitting diodes with large overlap quantum wells," *Optics Express*, vol. 19, no. S4, pp. A991–A1007, 2011.

[10] G. Liu, J. Zhang, C. K. Tan, and N. Tansu, "Efficiency-droop suppression by using large-bandgap AlGaInN thin barrier layers in InGaN quantum-well light-emitting diodes," *IEEE Photonics Journal*, vol. 5, no. 2, Article ID 2201011, 2013.

[11] H. J. Kim, S. Choi, S.-S. Kim et al., "Improvement of quantum efficiency by employing active-layer-friendly lattice-matched InAlN electron blocking layer in green light-emitting diodes," *Applied Physics Letters*, vol. 96, no. 10, Article ID 101102, 2010.

[12] B. C. Lin, K. J. Chen, C. H. Wang et al., "Hole injection and electron overflow improvement in InGaN/GaN light-emitting diodes by a tapered AlGaN electron blocking layer," *Optics Express*, vol. 22, pp. 463–469, 2014.

[13] N. F. Gardner, G. O. Müller, Y. C. Shen et al., "Blue-emitting InGaN-GaN double-heterostructure light-emitting diodes reaching maximum quantum efficiency above 200 A/cm^2," *Applied Physics Letters*, vol. 91, no. 24, Article ID 243506, 2007.

[14] J. Xie, X. Ni, Q. Fan, R. Shimada, U. Ozgur, and H. Morko, "On the efficiency droop in InGaN multiple quantum well blue light emitting diodes and its reduction with p -doped quantum well barriers," *Applied Physics Letters*, vol. 93, no. 12, Article ID 121107, 2008.

[15] K. McGroddy, A. David, E. Matioli et al., "Directional emission control and increased light extraction in GaN photonic crystal light emitting diodes," *Applied Physics Letters*, vol. 93, no. 10, Article ID 103502, 2008.

[16] J. J. Wierer Jr., A. David, and M. M. Megens, "III-nitride photonic-crystal light-emitting diodes with high extraction efficiency," *Nature Photonics*, vol. 3, no. 3, pp. 163–169, 2009.

[17] X. H. Li, R. Song, Y. K. Ee, P. Kumnorkaew, J. F. Gilchrist, and N. Tansu, "Light extraction efficiency and radiation patterns of

III-nitride light-emitting diodes with colloidal microlens arrays with various aspect ratios," *IEEE Photonics Journal*, vol. 3, no. 3, pp. 489–499, 2011.

[18] Y. C. Shen, G. O. Mueller, S. Watanabe, N. F. Gardner, A. Munkholm, and M. R. Krames, "Auger recombination in InGaN measured by photoluminescence," *Applied Physics Letters*, vol. 91, no. 14, Article ID 141101, 2007.

[19] K. T. Delaney, P. Rinke, and C. G. van de Walle, "Auger recombination rates in nitrides from first principles," *Applied Physics Letters*, vol. 94, no. 19, Article ID 191109, 2009.

[20] J. Iveland, L. Martinelli, J. Peretti, J. S. Speck, and C. Weisbuch, "Direct measurement of auger electrons emitted from a semiconductor light-emitting diode under electrical injection: identification of the dominant mechanism for efficiency droop," *Physical Review Letters*, vol. 110, no. 17, Article ID 177406, 2013.

[21] C.-K. Tan, J. Zhang, X.-H. Li, G. Liu, B. O. Tayo, and N. Tansu, "First-principle electronic properties of dilute-as GaNAs alloy for visible light emitters," *Journal of Display Technology*, vol. 9, no. 4, pp. 272–279, 2013.

[22] Y. K. Ee, J. M. Biser, W. Cao, H. M. Chan, R. P. Vinci, and N. Tansu, "Metalorganic vapor phase epitaxy of III-nitride light-emitting diodes on nanopatterned AGOG sapphire substrate by abbreviated growth mode," *IEEE Journal on Selected Topics in Quantum Electronics*, vol. 15, no. 4, pp. 1066–1072, 2009.

[23] Y. Li, S. You, M. Zhu et al., "Defect-reduced green GaInN/GaN light-emitting diode on nanopatterned sapphire," *Applied Physics Letters*, vol. 98, no. 15, Article ID 151102, 2011.

[24] Y.-J. Lee, C.-H. Chiu, C. C. Ke et al., "Study of the excitation power dependent internal quantum efficiency in InGaN/GaN LEDs grown on patterned sapphire substrate," *IEEE Journal on Selected Topics in Quantum Electronics*, vol. 15, no. 4, pp. 1137–1143, 2009.

Hindawi Publishing Corporation
International Journal of Photoenergy
Volume 2014, Article ID 959620, 4 pages
http://dx.doi.org/10.1155/2014/959620

Research Article

Low-Cost ZnO:YAG-Based Metal-Insulator-Semiconductor White Light-Emitting Diodes with Various Insulators

Lung-Chien Chen, Chih-Hung Hsu, Xiuyu Zhang, and Jia-Ren Wu

Department of Electro-Optical Engineering, National Taipei University of Technology, No. 1, Section 3, Chung-Hsiao E. Road, Taipei 106, Taiwan

Correspondence should be addressed to Lung-Chien Chen; ocean@ntut.edu.tw

Received 13 March 2014; Accepted 9 July 2014; Published 15 July 2014

Academic Editor: Hao-Chung Kuo

ZnO:YAG-based metal-insulator-semiconductor (MIS) diodes with various insulators were synthesized on an indium tin oxide (ITO) glass by ultrasonic spray pyrolysis. SiO_2 and MnZnO (MZO) were separately used as insulators. X-ray diffraction revealed the crystalline structure of the ZnO:YAG film. The photoluminescence (PL) properties of the ZnO:YAG film were studied and the color of photoluminescence was found to be almost white. The electrical properties of the diodes with different insulators and thicknesses were compared. The diode with the SiO_2 insulator had a lower threshold voltage, smaller leakage current, and a higher series resistance than that with the MZO insulator layer.

1. Introduction

Zinc oxide (ZnO) is II–VI compound semiconductor with a wide direct band gap (3.36 eV); it has a large exciton binding energy of 60 mV and a hexagonal wurtzite structure. These excellent physical properties and easy, low-cost synthesis make ZnO a promising material to replace III-nitride semiconductors for short-wavelength optoelectronic applications, such as blue/ultraviolet (UV) light emitting diodes (LED) [1–5]. Today, the most common white LED is fabricated from blue LEDs that are made of InGaN and coated with phosphors of different colors. ZnO is easier and cheaper to fabricate than the InGaN-based LED device. ZnO can be conveniently deposited over a large area for advanced lighting applications. Numerous ZnO nanorod-based or ZnO nanotube-based white LEDs have been developed in the past few years [6–9]. Most of the aforementioned devices require p-GaN to form a heterostructure and have a complex fabrication process. However, we have already demonstrated that the photoluminescence of ZnO:YAG is almost white [10]. Therefore, the ZnO:YAG film can be used to fabricate LEDs that emit white light using a simple ultrasonic spray process.

In this work, a ZnO:YAG-based MIS white LED is developed. SiO_2 and MnZnO (MZO) were used as insulators. The effects of various thicknesses of insulators were compared. The electrical properties and crystallinity of the ZnO:YAG film were examined by making Hall measurement and by X-ray diffraction (XRD) analysis. The PL measurements were carried out to study the luminescence of the prepared devices.

2. Experimental Details

Figure 1 schematically depicts the structure of the ZnO:YAG-based MIS LED. The ZnO:YAG layer with a thickness of 1 μm was deposited on a commercially available ITO/glass substrate by ultrasonic spray pyrolysis [10]. An aerosol of the precursor solution, which consisted of zinc acetate, ammonium acetate, and YAG phosphor (at 1 wt.%; NYAG4156 phosphor, INTEMATIX, Fremont, CA, USA) powder, was produced using a commercial ultrasonic nebulizer. Then, SiO_2 insulators with various thicknesses and ITO electrodes were deposited on the as-prepared ZnO:YAG films by RF sputtering for comparison. Table 1 presents the flow rate of argon, substrate temperature, sputtering power, and chamber pressure during the deposition by sputtering. The MZO insulator layer was also deposited by ultrasonic spray pyrolysis with a precursor solution that consisted of zinc acetate, ammonium acetate, and manganese chloride [11]. The

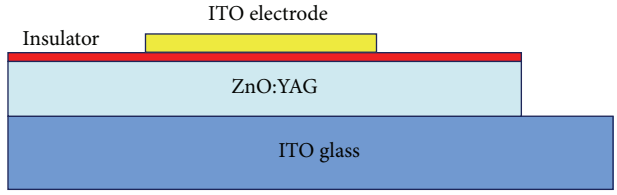

Figure 1: ITO/insulator/ZnO:YAG MIS structure on ITO/glass substrate.

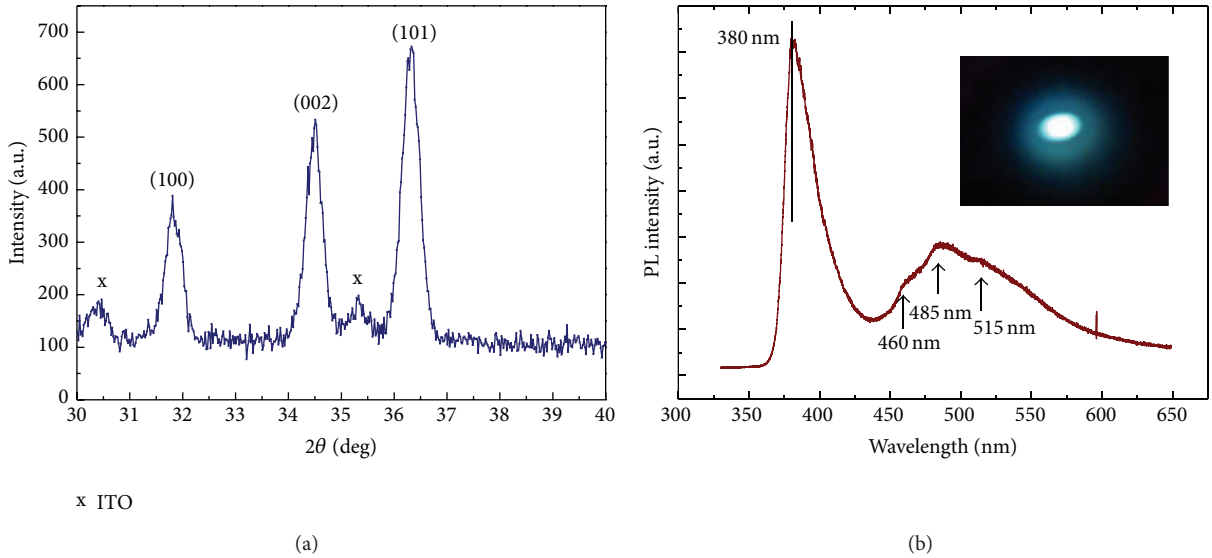

Figure 2: (a) XRD pattern and (b) RT PL spectrum of ZnO:YAG film on ITO/glass substrate deposited by ultrasonic spray pyrolysis. Inset shows photograph of photoexcited luminescence.

Table 1: Parameters of deposition of insulator and ITO electrode layers by sputtering.

	Flow rate of argon (sccm)	Substrate temperature (°C)	Sputtering power (W)	Chamber pressure (mTorr)
SiO_2	40	RT	60	4.23
ITO electrode	40	RT	50	3

Hall measurements revealed that ZnO:YAG exhibits n-type conduction with an electron concentration of approximately 10^{18} cm^{-3}. The current-voltage (I-V) characteristics of the devices were measured using a Keithley 2400 electrometer. The crystalline microstructure of the ZnO:YAG film was determined by X-ray diffraction with Cu-Kα radiation (λ = 0.1541 nm) in the scanning range of 2θ from 30° to 40°. The PL spectrum was obtained by a Dongwoo spectrophotometer (Dongwoo, Soule, Korea) at room temperature by exciting the ZnO:YAG using an He-Cd laser (325 nm).

3. Results and Discussion

Figure 2(a) shows a typical XRD pattern of the ZnO:YAG film that was deposited on an ITO/glass substrate that was prepared by the ultrasonic spray pyrolysis. The spectrum includes broad peaks at positions 31.82°, 34.52°, and 36.34°, which are strongly associated with the (100), (002), and (101) planes of the ZnO phase. This finding suggests that the thin film was polycrystalline and has a ZnO phase with a hexagonal wurtzite structure (by JCPDF no. 75-0576).

Figure 2(b) displays the room-temperature photoluminescence (RT PL) spectrumof the ZnO:YAG film. The dominant peak at 3.26 eV (380 nm) corresponds to the optical band gap of ZnO films with a wide band gap and can be attributed to the recombination of free excitons in an exciton-exciton collision process [12, 13]. The visible luminescence, emitted over a wide range from 450 nm to 600 nm, is composed of at least three broad peaks. The peaks at 460 nm, 480 nm, and 515 nm are attributed to electron transfer from the zinc interstitial level (Z_{ni}) to the oxygen vacancy (V_o) defect level, which may be caused by the incorporation of YAG phosphor [14]. The broad peak in the visible range may also include a peak at 540 nm, which is associated with emission by the YAG phosphor. The photoexcited luminescence of the ZnO:YAG film is almost white, as can be seen in the inset photograph in Figure 2(b). The 380 nm UV emission and the wide visible emission band ranging from 450 to 600 nm contribute together to the white light, as mentioned above such that the color of electroluminescence (EL) from the ZnO:YAG-based MIS LED should be white.

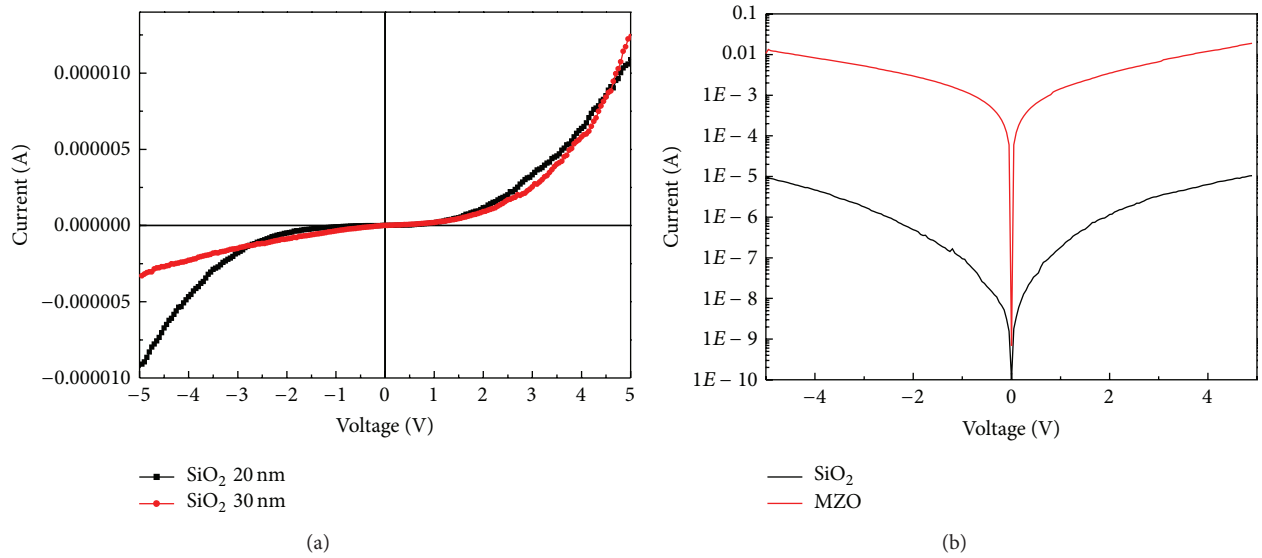

FIGURE 3: (a) *I-V* characteristics of ZnO:YAG-based MIS LED with SiO_2 insulator layer of varying thickness. (b) *I-V* characteristics of ZnO:YAG-based MIS LED with different insulator layers with a thickness of 200 nm.

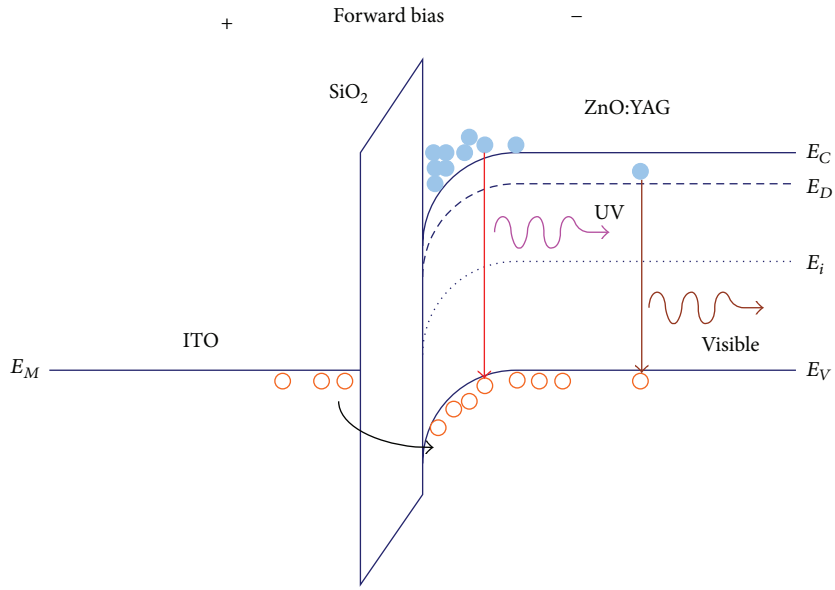

FIGURE 4: Energy band diagram of ZnO:YAG-based MIS LED with SiO_2 insulator layer under forward bias.

Figure 3 plots the *I-V* characteristics of the ZnO:YAG-based MIS LED with different insulator layers of various thicknesses. The device size is 3 mm × 3 mm. As presented in Figure 3(a), the *I-V* curves of the devices with SiO_2 insulator layers exhibit diode-like rectifying behavior to some extent. The forward threshold voltage is ~3 V. Figure 3(b) reveals that the ZnO:YAG-based MIS LED with the SiO_2 insulator layer has a lower leakage current and a higher series resistance than that with the MZO insulator layer. The forward threshold voltage of the device with the MZO insulator layer is ~2 V.

Figure 4 presents the energy band diagram of the ZnO:YAG-based MIS LED with an SiO_2 insulator layer under forward bias. The energy band of ZnO:YAG under the SiO_2 layer is bent downward under forward bias. Therefore, tunnel injection of holes from the ITO substrate into the valence band of ZnO:YAG film via surface states in the insulator layer occurs. The SiO_2 energy barrier is so large leading to induce an accumulation layer of electrons at the SiO_2/ZnO:YAG interface. Many of the holes that are injected from the ITO substrate are recombined with the electrons confined in the downward-bending region of the conduction band of ZnO:YAG film. The confined electrons and the defect levels (E_D) of ZnO:YAG film recombine radiatively with the injection holes in the valence band and then generate UV and visible emission, respectively. The white emission from the ZnO:YAG-based MIS LED can be theoretically understood

as being generated by blending UV and visible emission with YAG photoexcited emission.

4. Conclusion

The ZnO:YAG film herein has the hexagonal wurtzite structure and emits PL that is almost white. ZnO:YAG-based MIS LEDs with different insulator layers were successfully prepared using a low-cost, simple, but effective ultrasonic spray pyrolysis method. The diode with the SiO_2 insulator had a lower threshold voltage, smaller leakage current, and a higher series resistance than the one with the MNO insulator layer. The modal of the energy band of the device has been also addressed. The white emission from the ZnO:YAG-based MIS LED can be theoretically understood as being generated by blending UV and visible emission with YAG photoexcited emission. The study implies that the ZnO:YAG film is a promising material for fabricating white LED with low cost.

Conflict of Interests

The authors declare that there is no conflict of interests regarding the publication of this paper.

Acknowledgment

Financial support of this paper was provided by the National Science Council of the Republic of China under Contract no. NSC 102-2622-E-027-021-CC3.

References

[1] J.-H. Lim, C.-K. Kong, K.-K. Kim, I.-K. Park, D-K. Hwang, and S.-J. Park, "UV electroluminescence emission from ZnO light-emitting diodes grown by high-temperature radiofrequency sputtering," *Advanced Materials*, vol. 18, no. 20, pp. 2720–2724, 2006.

[2] H. Ohta, M. Orita, M. Hirano, and H. Hosono, "Fabrication and characterization of ultraviolet-emitting diodes composed of transparent p-n heterojunction, p-$SrCu_2O_2$ and n-ZnO," *Journal of Applied Physics*, vol. 89, no. 10, pp. 5720–5725, 2001.

[3] O. Lupan, T. Pauporté, and B. Viana, "Low-voltage UV-electroluminescence from ZnO-Nanowire array/p-CaN light-emitting diodes," *Advanced Materials*, vol. 22, no. 30, pp. 3298–3302, 2010.

[4] Q.-X. Yu, B. Xu, Q.-H. Wu et al., "Optical properties of ZnO/GaN heterostructure and its near-ultraviolet light-emitting diode," *Applied Physics Letters*, vol. 83, no. 23, pp. 4713–4715, 2003.

[5] M. T. Chen, M. P. Lu, Y. J. Wu et al., "Near UV LEDs made with in situ doped p-n homojunction ZnO nanowire arrays," *Nano Letters*, vol. 10, no. 11, pp. 4387–4393, 2010.

[6] J. R. Sadaf, M. Q. Israr, S. Kishwar, O. Nur, and M. Willander, "White electroluminescence using ZnO nanotubes/GaN heterostructure light-emitting diode," *Nanoscale Research Letters*, vol. 5, no. 6, pp. 957–960, 2010.

[7] S. Kishwar, K. Ul Hasan, N. H. Alvi, P. Klason, O. Nur, and M. Willander, "A comparative study of the electrodeposition and the aqueous chemical growth techniques for the utilization of ZnO nanorods on p-GaN for white light emitting diodes," *Superlattices and Microstructures*, vol. 49, no. 1, pp. 32–42, 2011.

[8] C.-H. Chen, S.-J. Chang, S.-P. Chang et al., "Fabrication of a white-light-emitting diode by doping gallium into zno nanowire on a p-gan substrate," *Journal of Physical Chemistry C*, vol. 114, no. 29, pp. 12422–12426, 2010.

[9] A. Wadeasa, S. L. Beegum, S. Raja, O. Nur, and M. Willander, "The demonstration of hybrid n-ZnO nanorod/p-polymer heterojunction light emitting diodes on glass substrates," *Applied Physics A*, vol. 95, no. 3, pp. 807–812, 2009.

[10] L. C. Chen and C. C. Huang, "Optoelectronic characteristics of YAG phosphor-incorporated ZnO films deposited by ultrasonic spray pyrolysis," *Nanoscale Research Letters*, vol. 7, article 627, 2012.

[11] L. Chen, C. Tien, and C. Fu, "Magneto-optical characteristics of Mn-doped ZnO films deposited by ultrasonic spray pyrolysis," *Materials Science in Semiconductor Processing*, vol. 15, no. 1, pp. 80–85, 2012.

[12] Y. C. Kong, D. P. Yu, B. Zhang, W. Fang, and S. Q. Feng, "Ultraviolet-emitting ZnO nanowires synthesized by a physical vapor deposition approach," *Applied Physics Letters*, vol. 78, no. 4, pp. 407–409, 2001.

[13] S. C. Lyu, Y. Zhang, H. Ruh et al., "Low temperature growth and photoluminescence of well-aligned zinc oxide nanowires," *Chemical Physics Letters*, vol. 363, no. 1-2, pp. 134–138, 2002.

[14] N. H. Alvi, K. Ul Hasan, O. Nur, and M. Willander, "The origin of the red emission in n-ZnO nanotubes/p-GaN white light emitting diodes," *Nanoscale Research Letters*, vol. 6, article 130, 2011.

Hindawi Publishing Corporation
International Journal of Photoenergy
Volume 2014, Article ID 385257, 7 pages
http://dx.doi.org/10.1155/2014/385257

Research Article

Efficiency and Droop Improvement in GaN-Based High-Voltage Flip Chip LEDs

Yen-Chih Chiang,[1] Bing-Cheng Lin,[2] Kuo-Ju Chen,[2] Sheng-Huan Chiu,[2] Chien-Chung Lin,[3] Po-Tsung Lee,[2] Min-Hsiung Shih,[4] and Hao-Chung Kuo[2]

[1] *Institute of Lighting and Energy Photonics, National Chiao Tung University, Tainan 71550, Taiwan*
[2] *Department of Photonics and Institute of Electro-Optical Engineering, National Chiao Tung University, Hsinchu 30010, Taiwan*
[3] *Institute of Photonics System, National Chiao Tung University, Tainan 71550, Taiwan*
[4] *Research Center for Applied Sciences, Academia Sinica, 128 Academia Road, Sec. 2 Nankang, Taipei 115, Taiwan*

Correspondence should be addressed to Chien-Chung Lin; chienchunglin@faculty.nctu.edu.tw
and Hao-Chung Kuo; hckuo@faculty.nctu.edu.tw

Received 13 February 2014; Accepted 2 June 2014; Published 30 June 2014

Academic Editor: Nelson Tansu

The GaN-based high-voltage flip chip light-emitting diode (HVFC-LED) is designed and developed for the purpose of efficiency enhancement. In our design, the distributed Bragg reflector (DBR) is deposited at the bonded substrate to increase the light extraction. After the flip chip process, the general current-voltage characteristics between the flip chip sample and the traditional sample are essentially the same. With the help of great thermal conductive silicon substrate and the bottom DBR, the HVFC-LED is able to enhance the power by 37.1% when compared to the traditional high-voltage LEDs. The wall-plug efficiencies of the HVFC-LED also show good droop reduction as high as 9.9% compared to the traditional devices.

1. Introduction

The availability of high brightness, high power, and large area of GaN-based light-emitting diodes (LEDs) has enabled their applications in exterior automotive lightings, outdoor displays, backlights for liquid crystal display (LCD) TVs, various handheld devices, printers, and rear projection TVs [1]. However, the notorious efficiency droop phenomenon makes the GaN LEDs more power-consuming at higher current and causes the increase of chip cost. Various mechanisms have been proposed as the reasons of this efficiency droop, including electron leakage out of the active region, Auger recombination, carrier delocalization, and poor hole injection [2–5]. To further reduce the production cost and enhance the performance of these LEDs, there is always a great need to improve the external quantum efficiency (EQE) and solve the efficiency droop. Recent studies have substantially alleviated droop by new active region design such as reduced charge separation [6–8], nano/microphotonics structures [9, 10], novel growth and substrate technologies [11], and barrier engineering [12]. In addition, the optimization of the light extraction efficiency is of great importance to achieve large EQE in the nitride-based LEDs. Previously, it has been shown that one can utilize a transparent contact layer (TCL) [13], patterned sapphire substrates (PSSs) [14, 15], surface texturing (ST) [16], and/or flip chip (FC) technology [17–19] to enhance light extraction of nitride-based LEDs. Using TCL, one can reduce absorption of the conventional Ni-Au *p*-contact layer. One can reduce dislocation density in the epitaxial layers and also enhance light scattering at GaN—sapphire interface by PSS technology. With ST technology, photon emission can be randomized by surface scattering due to the roughened top surface of the LED. By FC technology, one can achieve larger LED output power since no bonding pads or wires exist on top of the devices so that photons could be emitted freely from the substrates.

Until recently, the traditional sapphire-based high power LED still dominates the lighting market. Due to poor thermal conductivity of the sapphire substrate, high operational current leads to current-crowding and bad thermal dispersion

Table 1: The R_{th} and T_j comparison of three kinds of LED.

		Conventional HV-LED (Ref-1)	HV-LED with ODR (Ref-2)	HVFC-LED
25°C 350 mA	R_{th} (°C/W)	62.9	55.4	41.7
	T_j (°C)	43.5	39.8	35.3
25°C 700 mA	R_{th} (°C/W)	63.1	55.6	41.8
	T_j (°C)	67.3	59.6	51.5
25°C 1000 mA	R_{th} (°C/W)	63.3	55.7	41.9
	T_j (°C)	97.1	81.3	65.3

problem. These problems are always haunting the high-current performance of the traditional LEDs. Recent research on high-voltage light-emitting diode (HV-LED) has shown that multiple series-connected microdiodes in a single large chip can obtain high forward voltage with a low driving current, thereby reducing current crowing and efficiency droop [20–22]. Moreover, the HV-LED can effectively avoid thermal problem due to relatively low operating current. Another advantage brought by high-voltage/low current operation is the direct utilization of the regular wall plug outlet without further voltage conversion. These features, combined with fewer wire-bonding needed, make HV-LED attractive for commercial applications.

In this study, a high-voltage flip chip LED (HVFC-LED) which consists of *n*-side up multiple series-connected diodes is demonstrated. This design provides high thermal conductivity and high bottom reflection silicon submount. In addition to these features, a high wall-plug efficiency can be expected [22]. In the subsequent text, we will discuss fabrications and performance analysis of this device.

2. Device Fabrication and Measurement

In the experiment, the LEDs were grown on *c*-plane sapphire substrate by metal-organic chemical vapor deposition (MOCVD) system. The structure includes a *n*-GaN layer, an $In_xGa_{1-x}N$/GaN multiple-quantum wells, a *p*-AlGaN electron blocking layer, and a *p*-GaN layer. In the device fabrication, firstly, a 120 nm indium tin oxide (ITO) transparent conductive layer was deposited by e-beam evaporator. Then, the mesa of microchips and *n*-contact area were etched by inductively coupled plasma (ICP) etcher. After that, the 10 μm trenches were etched by ICP between microchips [22–24]. To prevent the short circuit between each microchip, the passivation SiO_2 layer (700 nm) was deposited by plasma enhanced chemical vapor deposition (PECVD), and the interconnected Cr/Pt/Au (50/50/1500 nm) was up to evaporation by e-beam evaporator to serve as cathodes. Until this step, the multiple series-connected diodes are done.

Before connecting the chip and the submount, 15 pairs of SiO_2/TiO_2 distributed Bragg reflector (DBR) were prepared on silicon submount by e-beam evaporator [25]. Finally, through 280°C 15 min thermal reflow, the 45 mil × 45 mil chip is flip mounted on this reflective silicon submount by gold-tin eutectic bonding and then the process is finished. For comparison purpose, two different types of packaged LED chips were prepared: the first one is the conventional HV-LED with patterned sapphire substrate and the other is similar to HV-LED but extra 5.5 pairs of SiO_2/TiO_2 and Al/Ti/Ni/Au omnidirectional reflector (ODR) layer were deposited at the bottom of sapphire substrate. Both types of devices are of the same chip size and referred to as HV-LED and HV-LED + ODR, respectively.

Figure 1 shows the schematic diagrams of the three LEDs [26]. To have a fair comparison, the reflectivities at 455 nm for both DBR and ODR were close to 100%. Both reflectances were shown in Figure 2. The optical and electrical characteristics of the devices were measured at room temperature using a manual probing system with integrating sphere detector and supplying steady DC current by Keithly 2600 [27]. In order to eliminate the thermal effect under continuous DC current which can decimate to lead the light output power, a separate *L-I-V* characteristic under pulse mode with 2.5% duty cycle was performed.

Thermal dispersion of substrate can be analyzed by using T3Ster thermal transient tester to measure thermal resistance (R_{th}) and junction temperature (T_j). From Table 1, the HVFC-LED clearly has a leading edge on both R_{th} and T_j. These data strengthen the claim that HVFC-LED has good thermal dispersion.

3. Results and Discussion

Figure 3 shows the *L-I-V* curves of these three LED devices. At the same 20 mA driving current, the forward voltages of these three LEDs were 49.0~50.0 V. Compared with conventional HV-LED and HV-LED + ODR, the light output power of HVFC-LED is found to be enhanced by 37.1% and 5.1% at the same 20 mA current injection, respectively. There are two main reasons for the large enhancement of power intensity: The configuration of HVFC-LED provides better thermal conductivity by extra high reflection and high thermal conductive silicon submount (silicon~120 W/mK

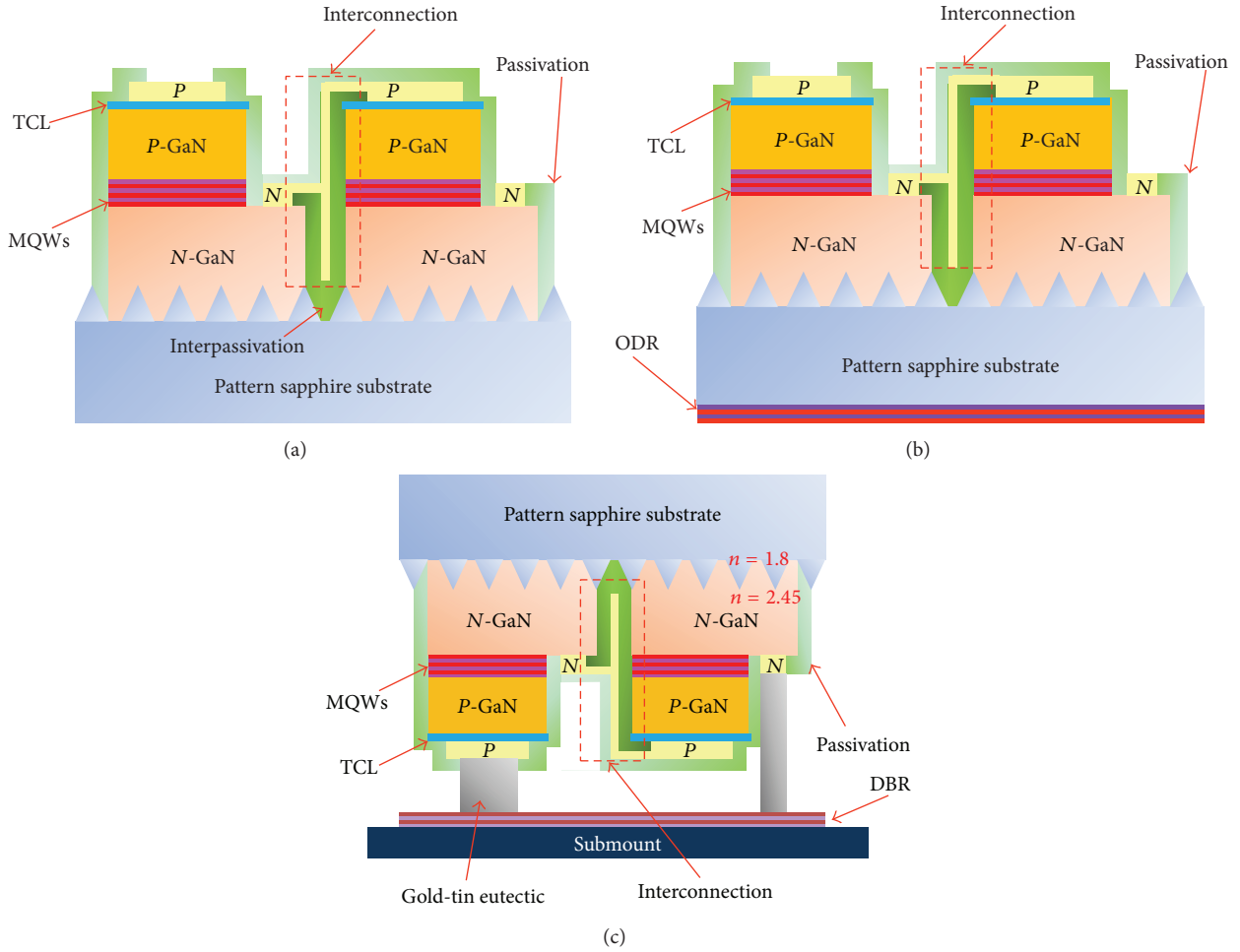

Figure 1: Schematic diagrams of (a) the conventional HV-LED, (b) HV-LED + ODR, and (c) high-voltage flip chip LED (HVFC-LED).

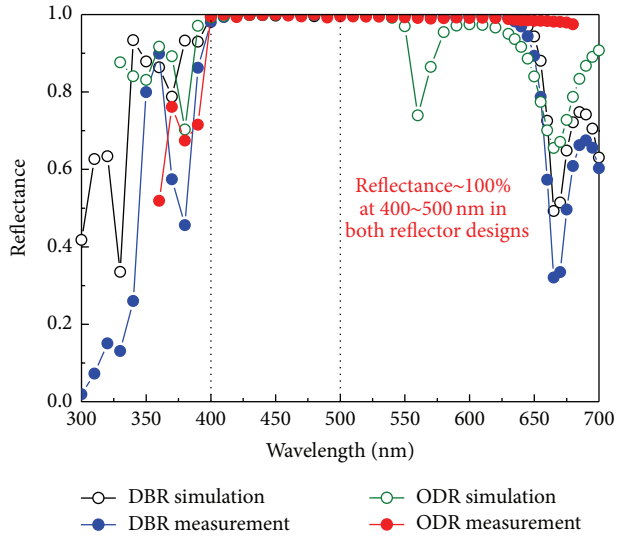

Figure 2: The reflectance in measurement results and simulation data between distributed Bragg reflector (DBR) and omnidirectional reflector (ODR).

Table 2: The wall plug efficiency comparison of three kinds of LED.

	Conventional HV-LED (ref-1)	HV-LED with ODR (ref-2)	HVFC-LED (versus ref-1)	HVFC-LED (versus ref-2)
Peak efficiency	46.9%	59.9%	62.0%	
Efficiency @ 1 watt	31.8%	40.8%	44.0%	
Efficiency @ 3 watt	21.1%	26.5%	29.3%	
ŋ @ 1 watt	32.2%	31.6%	29.0%	
ŋ @ 3 watt	55.0%	55.8%	52.7%	
Droop improve @ 1 watt			9.9%	9.2%
Droop improve @ 3 watt			4.2%	5.6%

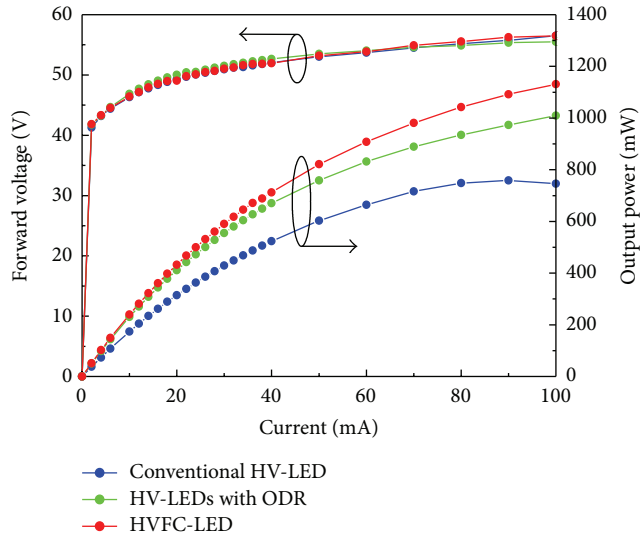

Figure 3: Forward voltage and light output power as a function of current for the three LEDs under pulse current injection.

versus Al_2O_3 ~ 25 W/mK) and not any effect by electrode shadow, thus leading to higher light output power and better efficiency.

Due to different packaging design, even though the reflectances of ODR and DBR are similar, the outcomes are different. In the HV-LED + ODR design, the outgoing photons have to travel through a thick *n*-type GaN and a thick sapphire substrate before hitting the ODR layer structure. This trip through *n*-GaN can effectively reduce the reflected photons by the extra scattering and GaN absorption, and thus the effect of ODR is hindered. On the contrary, in the flip chip bonded device the photons travel much less distance before reaching the DBR layer, and the bouncing of the photons can be more pronounced than HV-LED + ODR case.

All these factors can be seen via the output powers and efficiencies shown in Figures 3 and 4. The device efficiencies of the conventional HV-LED, HV-LED + ODR, and HVFC-LED at the same 1 watt consumed power were calculated as 31.8%, 40.8%, and 44.0%, respectively. The device efficiency droop can be written as

$$\text{droop} = \left(1 - \frac{\eta_{\text{high\_current}}}{\eta_{\max}}\right) \times 100\%. \quad (1)$$

According to (1), the droops of the conventional HV-LED, HV-LED + ODR, and HVFC-LED were calculated as 32.2%, 31.6%, and 29.0%, respectively (Table 2). As a result, the HVFC-LED possesses droop reduction of 9.9% and 9.2% in regard to traditional HV-LED and HV-LED+ODR. At 3 watts consumed power, thedroops of these three devices were calculated as 55.0%, 55.8%, and 52.7%, respectively. The HVFC-LED also improved efficiency droop 4.2% and 5.6% in regard to the other two devices. The major impact comes from the configuration of HVFC-LED which provides better thermal conductivity and photon extraction via silicon substrate and DBR deposition.

Figure 5 shows the measured light pattern of these three LEDs. The light intensity distribution of these three kinds of devices was under the same measurement setting. The power intensity of HVFC-LED and two references were demonstrated in *L-I-V* curve, and the measured values were 432 mW, 411 mW, and 315 mW, respectively. Figure 6 shows the simulated results of these three LED devices by using the optical ray tracing simulation software. The model was composed of 15 units of LEDs with either top or bottom surface emission capabilities, and the emitted rays could

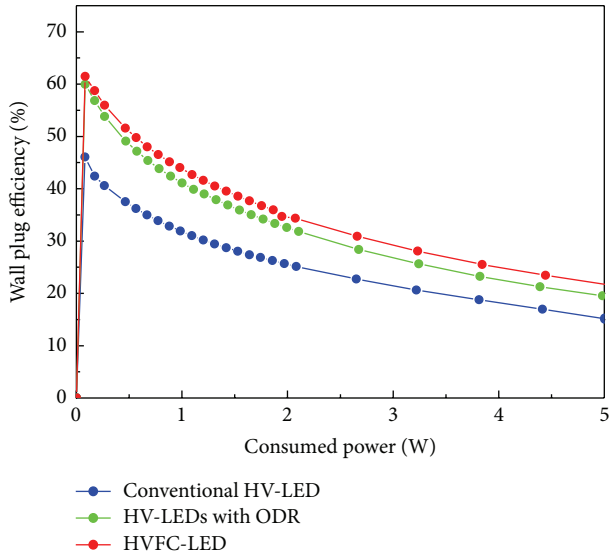

Figure 4: The wall plug efficiency curves of these three LEDs at the same consumed power.

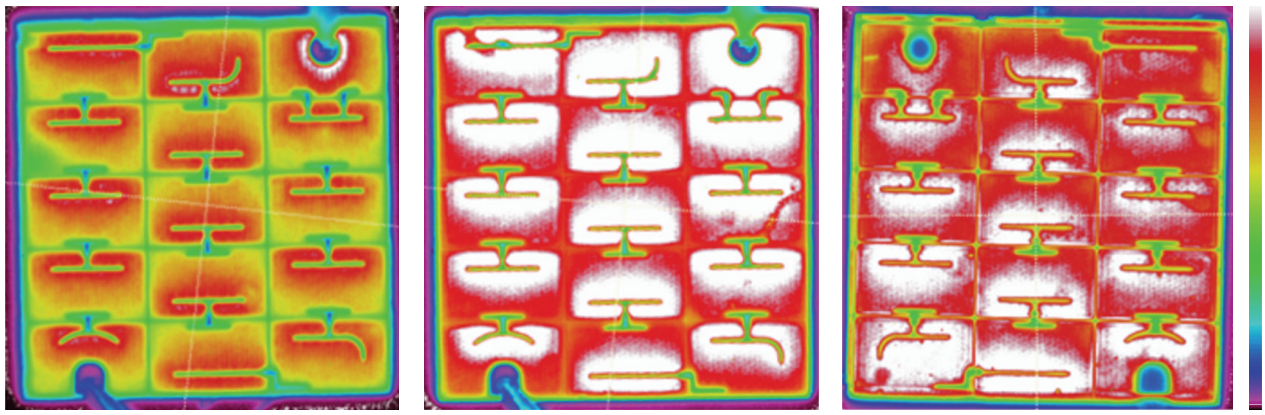

Figure 5: Light intensity distribution map of (a) the conventional HV-LED, (b) HV-LED + ODR, and (c) HVFC-LED.

escape the chip from either surfaces. As we discussed before, three cases were analyzed: (1) the rays directed through the sapphire substrate without any reflector as conventional HV-LED, (2) the rays reflected by reflector on the backside of sapphire as HV-LED + ODR device, and (3) the rays reflected by reflector of submount substrate as HVFC-LED model. As shown in simulation results, the total flux of conventional HV-LED, HV-LED + ODR, and HVFC-LED was approximated 0.0200 lm, 0.0276 lm, and 0.0291 lm, respectively. The enhancement by the HVFC-LED compared to HV-LED and HV-LED + ODR cases is calculated as 45.5% and 5.4%. These values show good agreement with the enhancement of power intensity (37.1% and 5.1%) in experiment data. However, the calculation does not take into account the effects like current spreading or nonideal interface scattering which could erode the actual light extraction enhancement of our HVFC-LED devices. This result confirms that the HVFC-LED design did contribute to increasing flux and power intensity.

4. Conclusion

In conclusion, the high-voltage flip chip light-emitting diodes (HVFC-LED) were investigated, and three types of devices including InGaN HVFC-LED, conventional HV-LED, and HV-LED + ODR were all prepared and tested at the same time. The results indicated HVFC-LED improved the power intensity around 37.1% and 5.1% compared to the other two types of devices under 20 mA drive. At the same time, the efficiency droop of HVFC-LED improved approximation to 9.9% and 9.2% compared to both references. When the consumed power is increased, the droop improvement is not scaled. These measurement and simulation results all point

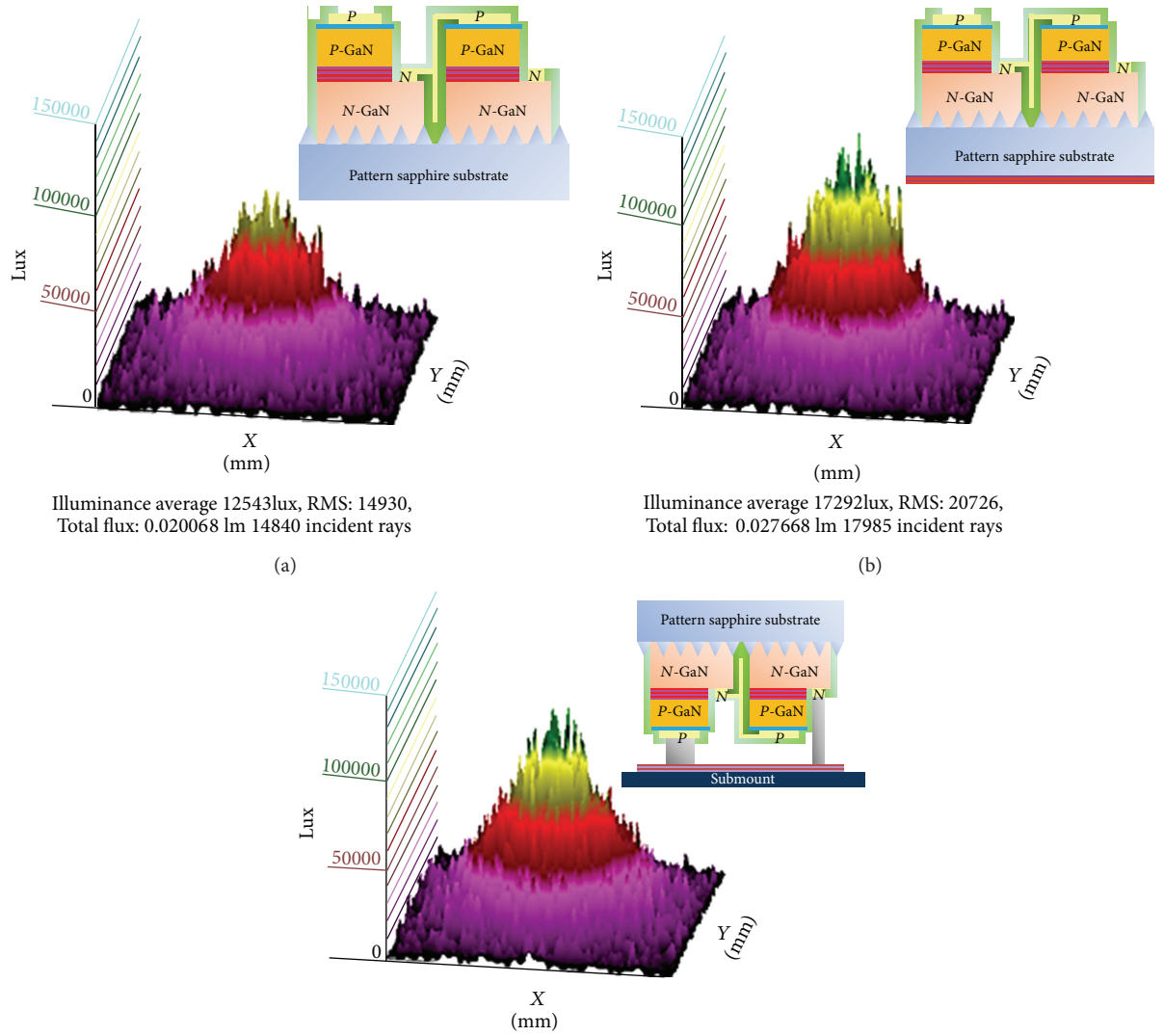

Figure 6: Simulated results of (a) the conventional HV-LED, (b) HV-LED + ODR, and (c) HVFC-LED.

out to the HVFC-LED being indeed a better design in terms of packaging, and we believe this design can be beneficial for the future generation of solid state lighting.

Conflict of Interests

The authors declare that there is no conflict of interests regarding the publication of this paper.

Acknowledgment

This work was supported in part by the National Science Council in Taiwan under Grant nos. NSC-103-3113-E-009-001-CC2 and NSC101-2221-E-009-046-MY3.

References

[1] S. Nakamura, T. Mukai, and M. Senoh, "Candela-class high-brightness InGaN/AlGaN double-heterostructure blue-light-emitting diodes," *Applied Physics Letters*, vol. 64, no. 13, pp. 1687–1689, 1994.

[2] K. J. Vampola, M. Iza, S. Keller, S. P. DenBaars, and S. Nakamura, "Measurement of electron overflow in 450 nm InGaN light-emitting diode structures," *Applied Physics Letters*, vol. 94, no. 6, Article ID 061116, 2009.

[3] C. H. Wang, J. R. Chen, C. H. Chiu et al., "Temperature-dependent electroluminescence efficiency in blue InGaN–GaN light-emitting diodes with different well widths," *IEEE Photonics Technology Letters*, vol. 22, no. 4, pp. 236–238, 2010.

[4] A. David and M. J. Grundmann, "Droop in InGaN light-emitting diodes: a differential carrier lifetime analysis," *Applied Physics Letters*, vol. 96, no. 10, Article ID 103504, 2010.

[5] B. Monemar and B. E. Sernelius, "Defect related issues in the "current roll-off" in InGaN based light emitting diodes," *Applied Physics Letters*, vol. 91, no. 18, Article ID 181103, 2007.

[6] H. Zhao, G. Liu, J. Zhang, J. D. Poplawsky, V. Dierolf, and N. Tansu, "Approaches for high internal quantum efficiency green InGaN light-emitting diodes with large overlap quantum wells," *Optics Express*, vol. 19, no. 14, pp. A991–A1007, 2011.

[7] H. Zhao and N. Tansu, "Optical gain characteristics of staggered InGaN quantum wells lasers," *Journal of Applied Physics*, vol. 107, no. 11, Article ID 113110, 2010.

[8] J. Zhang and N. Tansu, "Improvement in spontaneous emission rates for InGaN quantum wells on ternary InGaN substrate for light-emitting diodes," *Journal of Applied Physics*, vol. 110, no. 11, Article ID 113110, 2011.

[9] E. Rangel, E. Matioli, Y. S. Choi, C. Weisbuch, J. S. Speck, and E. L. Hu, "Directionality control through selective excitation of low-order guided modes in thin-film InGaN photonic crystal light-emitting diodes," *Applied Physics Letters*, vol. 99, Article ID 171106, pp. 081104-1–081104-3, 2011.

[10] X. Li, R. Song, Y. Ee, P. Kumnorkaew, J. F. Gilchrist, and N. Tansu, "Light extraction efficiency and radiation patterns of III-nitride light-emitting diodes with colloidal microlens arrays with various aspect ratios," *IEEE Photonics Journal*, vol. 3, no. 3, pp. 489–499, 2011.

[11] Y. J. Lee, C. H. Chiu, C. C. Ke et al., "Study of the excitation power dependent internal quantum efficiency in InGaN/GaN LEDs grown on patterned sapphire substrate," *IEEE Journal on Selected Topics in Quantum Electronics*, vol. 15, no. 4, pp. 1137–1143, 2009.

[12] H. Zhao, G. Liu, R. A. Arif, and N. Tansu, "Current injection efficiency induced efficiency-droop in InGaN quantum well light-emitting diodes," *Solid-State Electronics*, vol. 54, no. 10, pp. 1119–1124, 2010.

[13] S. J. Chang, C. S. Chang, Y. K. Su et al., "Highly reliable nitride-based LEDs with SPS+ITO upper contacts," *IEEE Journal of Quantum Electronics*, vol. 39, no. 11, pp. 1439–1443, 2003.

[14] K. Tadatomo, H. Okagawa, T. Tsunekawa et al., "High output power InGaN ultraviolet light-emitting diodes fabricated on patterned substrates using metalorganic vapor phase epitaxy," *Physica Status Solidi (A)*, vol. 188, no. 1, pp. 121–125, 2001.

[15] Y. J. Lee, J. M. Hwang, T. C. Hsu et al., "Enhancing the output power of GaN-based LEDs grown on wet-etched patterned sapphire substrates," *IEEE Photonics Technology Letters*, vol. 18, no. 10, pp. 1152–1154, 2006.

[16] T. Fujii, Y. Gao, R. Sharma, E. L. Hu, S. P. DenBaars, and S. Nakamura, "Increase in the extraction efficiency of GaN-based light-emitting diodes via surface roughening," *Applied Physics Letters*, vol. 84, no. 6, pp. 855–857, 2004.

[17] J. Lee, S. Na, J. Jeong et al., "Low resistance and high reflectance Pt/Rh contacts to p-Type GaN for Ga N-based flip chip light-emitting diodes," *Journal of the Electrochemical Society*, vol. 152, no. 1, pp. G92–G94, 2005.

[18] S. J. Chang, W. S. Chen, Y. C. Lin et al., "Nitride-based flip-chip LEDs with transparent ohmic contacts and reflective mirrors," *IEEE Transactions on Advanced Packaging*, vol. 29, no. 3, pp. 403–408, 2006.

[19] C. F. Shen, S. J. Chang, W. S. Chen, T. K. Ko, C. T. Kuo, and S. C. Shei, "Nitride-based high-power flip-chip LED with double-side patterned sapphire substrate," *IEEE Photonics Technology Letters*, vol. 19, no. 10, pp. 780–782, 2007.

[20] K. Chen, H. Kuo, Y. Chiang et al., "Efficiency and droop improvement in hybrid warm white LEDs using InGaN and AlGaInP high-voltage LEDs," *IEEE/OSA Journal of Display Technology*, vol. 9, no. 4, pp. 280–284, 2013.

[21] K. J. Chen, H. T. Kuo, H. C. Chen et al., "High thermal stability of correlated color temperature using current compensation in hybrid warm white high-voltage LEDs," *Optics Express*, vol. 21, article S2, pp. A201–A207, 2013.

[22] C. H. Wang, D. W. Lin, C. Y. Lee et al., "Efficiency and droop improvement in GaN-based high-voltage light-emitting diodes," *IEEE Electron Device Letters*, vol. 32, no. 8, pp. 1098–1100, 2011.

[23] Y. Ding, W. Guo, Y. Zhu, Y. Liu, J. Liu, and W. Yan, "Fabrication of high-voltage light emitting diodes with a deep isolation groove structure," *Journal of Semiconductors*, vol. 33, no. 9, Article ID 094007, 2012.

[24] J. M. Hong, X. Y. Li, and P. J. Niu, "Review of recent HV-LED technology," *Applied Mechanics and Materials*, vol. 220–223, pp. 2075–2078, 2012.

[25] S. J. Chang, C. F. Shen, M. H. Hsieh et al., "Nitride-based LEDs with a hybrid Al mirror $+TiO_2/SiO_2$ DBR backside reflector," *Journal of Lightwave Technology*, vol. 26, no. 17, pp. 3131–3136, 2008.

[26] Y. P. Hsu, S. J. Chang, Y. K. Su et al., "InGaN/GaN light-emitting diodes with a reflector at the backside of sapphire substrates," *Journal of Electronic Materials*, vol. 32, no. 5, pp. 403–406, 2003.

[27] W. L. Guo, W. W. Yan, Y. X. Zhu et al., "Analysis on electrical characteristics of high-voltage GaN-based light-emitting diodes," *Chinese Physics B*, vol. 21, no. 12, Article ID 127201, 2012.

Hindawi Publishing Corporation
International Journal of Photoenergy
Volume 2014, Article ID 574270, 6 pages
http://dx.doi.org/10.1155/2014/574270

Research Article

Implementation and Test of a LED-Based Lamp for a Lighthouse

Luca Mercatelli, David Jafrancesco, Franco Francini, Daniela Fontani, Elisa Sani, Stefano Coraggia, Marco Meucci, and Paola Sansoni

CNR-INO National Institute of Optics, 6 Largo E. Fermi, 50125 Firenze, Italy

Correspondence should be addressed to Paola Sansoni; paola.sansoni@ino.it

Received 12 February 2014; Accepted 2 June 2014; Published 24 June 2014

Academic Editor: Nelson Tansu

A novel sustainable source was developed for an existing Italian lighthouse, exploiting the light emitting diode (LED) technology and the norms evolution. The research work started with the optical design of the device, while this work concerns the realization, installation, and test of the new LED lamp. The lamp recombines multiple separated LEDs, realizing a quasipunctual localized source. After installation in the lighthouse, specific photometric tests verified that the proposed power-saving source satisfied the illumination requirements of the marine signaling norms. The advantages of the LED-based lamp are reduced energy consumption, enhanced efficiency, longer life, decreased faults, slower aging, and lower maintenance costs. The obtained LED signalling device is more durable and reliable. In the future the application of these power-saving long-life sources could be extended to other maritime signaling devices or to other traffic signs.

1. Introduction

During the last years, the illumination industry is experiencing an epochal transformation, basically due to the introduction of LED (light emitting diode) technology. This novel artificial luminous source is changing the scenario of lighting applications, thanks to the properties of the LED emission spectrum [1]. In many different applications [2–4], for indoor and outdoor lighting, LED-based lamps are gradually becoming the most efficient light source, substituting both incandescent and fluorescent lamps.

In general the purpose of sustainable sources is to fulfil the application requirements reducing consumptions and costs. Concerning the light sources, these are rapidly evolving towards very-high-efficiency and long-lifetime lamps, with a view to bring down the substitution operations for faults and aging. Currently, LED sources appear to be the most promising solution for energy saving and environmental sustainability; in fact, LED-based sources are more efficient than fluorescent lamps, discharge lamps, halogen tungsten lamps, and traditional incandescent lamps. The key characteristic of a LED is the form of its emission spectrum, which creates and maintains its efficiency. The advantages of LED lamps are reduced energy consumption, enhanced efficiency, longer life, decreased faults, slower aging, and lower maintenance costs.

Lamp replacement is an important intervention in the lighting sector, because of the need not only to save energy but also to limit light pollution and to reduce maintenance costs [3, 5–8]. In the perspective of sustainable progress, the research for more efficient lighting devices is stimulated also by political actions. In practice, laws and regulations are acknowledging the recent technical progress undergone in the lighting industry, adapting norms [9, 10] and standards to the new commercial products emerging on the market.

The area of applicability of the proposed LED-based device is maritime signaling; the light source was designed to be mounted into the lighthouse of Tino Island, located in the north-west of Italy. Optical project and mechanical design were developed to fulfil the strict requirements of the norms for marine signaling [9, 10] and to adapt the novel sustainable source to replace the old lighthouse lamp [11, 12]. The LED-based lamp was realised and appropriate photometric tests [13–15] verified that the required illumination levels were distributed in agreement with the pertinent norm. It was then mounted on the lighthouse of Tino Island and several

field measurements certified the validity of this swap of the lighthouse lamp. The intent is to be able to substitute in an existing lighthouse the usual high-consuming short-life lamps with power-saving long-life LED-based sources [2, 5, 7]. This operation of lamp replacement is foreseen also for other lighthouse typologies and can be extended to other traffic signaling systems.

2. Photometric Tests

A prototype of the proposed LED lamp was realised on the basis of the optical project [11, 12], especially developed as luminous source of Tino Island lighthouse. The new lamp has a duration longer than an incandescent lamp and its power consumption is 135 W, versus some hundreds of Watts for a discharge lamp or 1000 W for a halogen lamp [13, 15]. The fail of one or few LEDs does not affect the operability of the lighthouse; it only appears as a gradual reduction of emitted light, while most of usual lamps would be switched off. This LED-based lamp is resistant to transportation and storage, and its installation in the lighthouse of Tino Island does not need mechanical changes in the existing lamp frame. The weaknesses with respect to traditional lamps are higher costs and slightly lower illumination level actually obtainable using commercial products.

Photometric measurements are of primary importance to comprehend if the novel source works correctly [16, 17] and if it complies with the maritime signaling norms [9, 10, 13]. Initially the functionality of the new LED source was tested in laboratory, referring to its optical design; successively specific field tests, executed on the LED-based lamp installed in the lighthouse, assessed its emission features on the field, in working condition.

The next sections describe optical tests and measurements performed on the LED device, which are listed below in order of execution:

(i) photometric measurements in laboratory,

(ii) measurement of the illumination produced on the inner surface of the Fresnel lens of the lighthouse, in relation to identical measurements performed with the traditional source (incandescent lamp),

(iii) assessment of the luminous range of the lighthouse through observations made from the sea,

(iv) measurement of temporal behaviour of the lighthouse flash.

3. Source Installation and Laboratory Tests

3.1. Mechanical Sizes and Distances. The working principle used to optically design the new LED-based source is that it recombines the light of a circular LED matrix to obtain a quasipunctual localized source. The rays coming from the LEDs, placed on a flat plate, are combined by a concave mirror near its focal point. A second mirror, with the shape of a cone, located near the first mirror focus, guides the rays in an annulus centered on the cone axis.

Lamp working principle and luminous rays' path are illustrated in Figure 1, where the flat plate mounting the LEDs matrix is shown at the bottom. A complete image of the new source is presented in Figures 2(a) and 2(b). The photometric centre of the optical system is considered at midheight of the cone (18.1 cm height from the LED plate). The emission angles are geometrically calculated with respect to the photometric centre (theoretical point inside the cone where the light reflected from the upper mirror would be focused), taking into account the dimensions of the structure. In fact, due to the LED plate and the upper mirror, which screen the emission, the maximum upper and lower angles (referring to the horizontal line) of aperture are, respectively, 15.8° and 49.4°. It must however be emphasized that, since the real photometric centre is not punctiform, the source can generate also rays outside of the geometric emission angles.

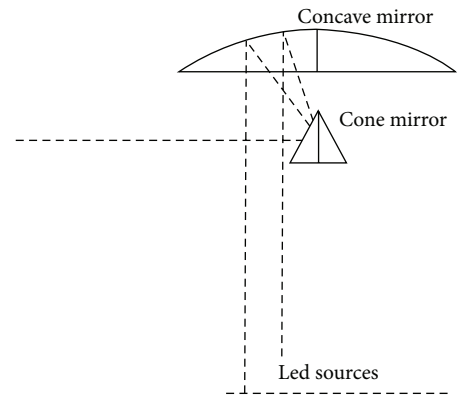

Figure 1: Working principle of the LED-based source.

3.2. Beam Width. In order to measure the effective vertical width of the beam that starts from the cone, appropriate measurements were performed by means of a diode laser and a screen. The experimental apparatus is described in Figure 3. A laser diode, with case size of a few centimetres, was positioned to emit a vertical beam. The laser was placed in correspondence with the plate mounting the LEDs matrix and it is moved along a radius of the plate. For each point of the radius (in steps of 1 cm), starting from the innermost one (at the base of the cone) up to the outer one, the position of the point where the laser beam encountered a screen placed at fixed distance was recorded. The radius, starting from the plate, is firstly reflected by the concave mirror, then from the cone, and then hits the screen.

The distance D between the screen and the centre of the cone is 182.7 cm.

From the obtained data the total angle of emission results to be 54.8 deg (18° above horizontal line, 36.8° below).

3.3. Luminous Intensity. The measurements of light intensity on the vertical plane were performed by measuring the *illuminance* produced by the source on a screen placed at 166.2 cm from the photometric centre of the lamp. The measurements were initially carried out with the source in normal operating conditions, with the cone obscured, in order to evaluate the light portion due to the reflection only on the concave mirror and the stray light in general, which does not contribute to the efficiency of the source.

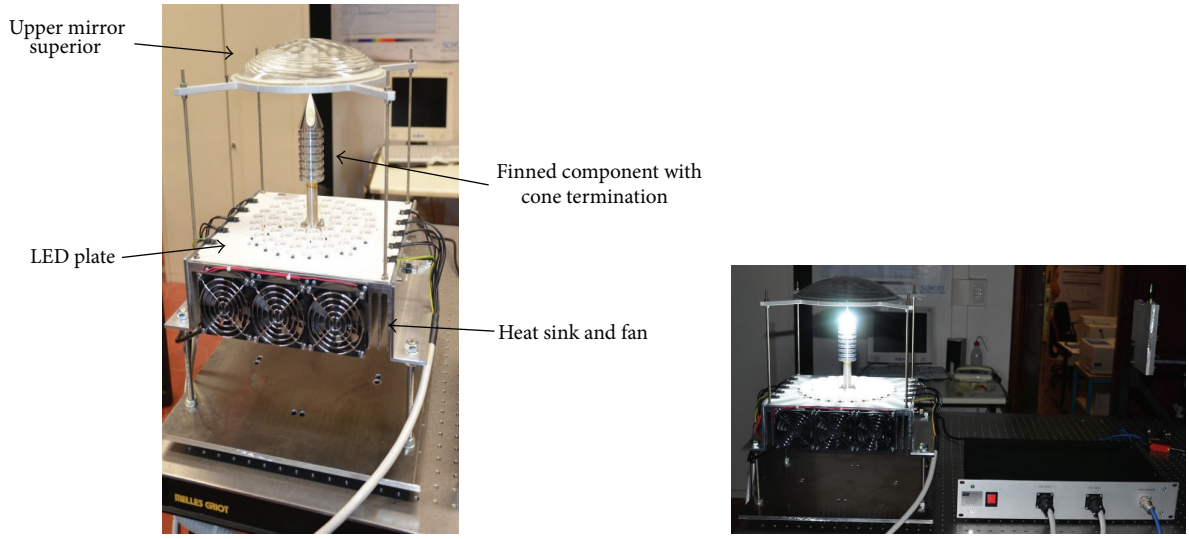

Figure 2: (a) Assembled LED-based lamp. (b) The LED lamp assembled and running.

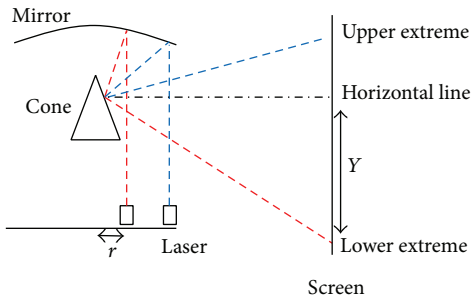

Figure 3: Experimental set-up to measure the angle of vertical emission.

The results are shown in Figure 4, as normalized light intensity, in arbitrary units. The solid line indicates the contribution due only to the cone, obtained for difference. The figure evidences the contribution due to the light coming directly from the concave mirror (stray light), especially below −30°.

The maximum value of the luminous intensity, corresponding to the horizontal direction, is 1000 ± 50 Cd.

From previous measurements, it is possible to evaluate, approximately, the difference between the new source and the former incandescent lamp. Indeed, the latter had a power of 1000 W, which means, considering luminous efficiency of 20 lm/W, a radiant flux of 20000 lm. This radiant flux value corresponds to a luminous intensity (equal in each direction) of about 1470 Cd, compared to an average value in the area of interest of the new source of about 1000 Cd that is 68% of the original luminous intensity. It is in a good agreement with the theoretical previsions.

4. On-Site Source Installation and Illuminance Tests

4.1. Mounting the Source inside the Lighthouse. The new LED source was assembled and installed in the lighthouse of Tino

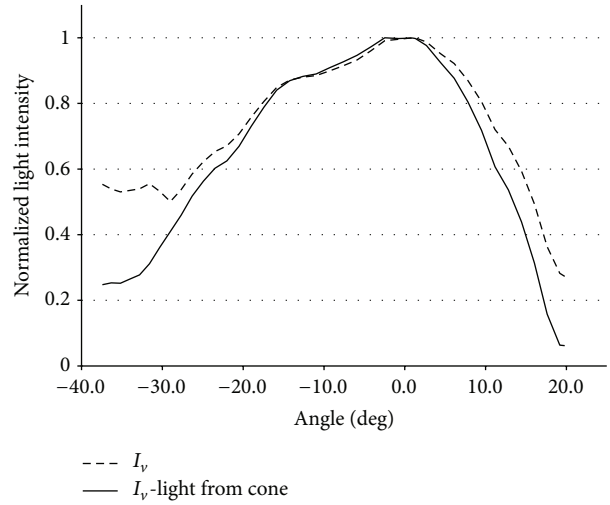

Figure 4: Normalized light intensity, in arbitrary units. Solid line: contribution only from the cone. It can be seen that beyond the range −29/18 deg the contribution is largely due to the light coming directly from the concave mirror (stray light).

Island (La Spezia, Italy) at the end of August 2012. The first step was to replace the incandescent bulb with the realised LED-based lamp. The second step was to correctly place the LED source; it was achieved by aligning the centre of the source, the centre of the Fresnel lens, and the horizon [13, 14].

The picture in Figure 5 illustrates the source mounted on Tino Island's lighthouse.

4.2. Illuminance on the Inner Surface of the Fresnel Lens. Illuminance measurements were performed on the Fresnel lens with a portable light meter Minolta T10, in order to evidence differences of the LED lamp behaviour with respect to the incandescent source. In practice, the light emerging from the point source that impinges on the Fresnel lens, will be, after refraction, redirected toward the horizon outside the

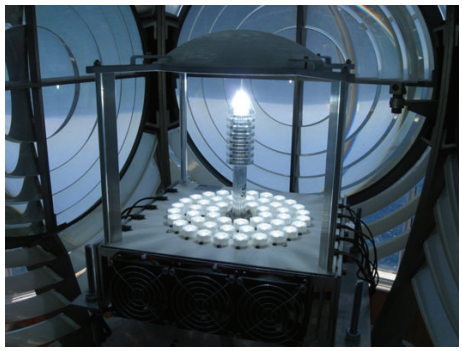

Figure 5: New source placed in the lighthouse, 3/4 view from above.

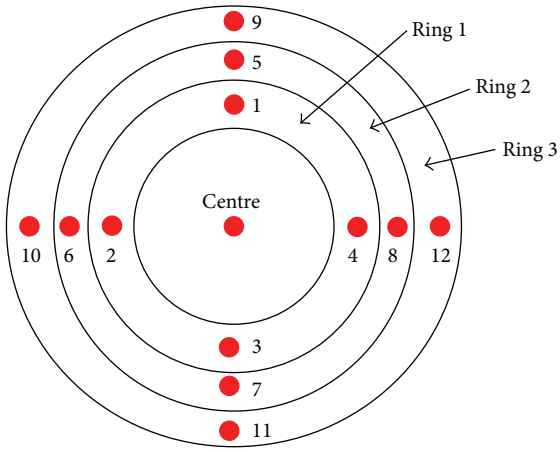

Figure 6: Measuring points on the inner surface of the Fresnel lens.

lighthouse. Due to the particularity of the application, the intensity measurements are not easy to perform, so this is a good evaluation of the differences between incandescent lamp and LED source. The measuring points are marked, each with its own number, in Figure 6, which depicts the central part of the Fresnel lens (inner surface), view from the inside of the lighthouse.

Figure 7 reports the difference, in percentage, between the illuminance obtained using LED lamp and incandescent lamp; points 1–4 are located in the inner ring; points 5–8 belong to the medium ring, while points 9–12 are sited on the external ring (see Figure 6). The variation of illuminance difference among the measurement points in the case of LED lamp and incandescent lamp depends on both the beam shape of the LED lamp, slightly downward-oriented due to the ray blocking of the top mirror (see Figure 3), and the dimming due to the top mirror supports. The highest percentage difference with respect to the case of incandescent source was in fact measured in points 1, 5, and 9 and points 7, 11: the first three points represent the upper part of the lens, less irradiated because of being near the maximum upper emission angle; analogously for points 7 and 11 in the lower part of the lens.

The new LED source illuminance on the inner surface of the Fresnel lens results, as average value, 68.8% of the illumination obtained with the incandescent lamp. This illuminance percentage is in excellent agreement with the

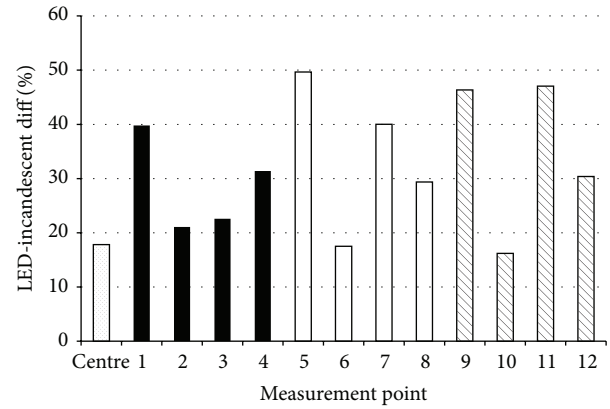

Figure 7: Percentage illuminance difference on the Fresnel lens between incandescent lamp and LED lamp.

evaluations performed starting from laboratory measurements (Sections 3.2-3.3). Hence a decrease of more than 30% on luminous intensity could be expected, as evidenced also in the simulations [11] executed to define the optical design of the LED-based lamp.

5. Measurements and Assessments at a Distance

5.1. Qualitative Analysis: Visual Evaluation from the Sea. In order to evaluate the range of the new beam of the lighthouse, in the night between April 17 and 18, 2013, exploiting a ship provided by the Italian Navy, visual assessments were performed from the sea.

The night was clear, moonless, and with good visibility (qualitative assessment). The deck of the ship was about 3 meters over the water's surface.

To give the maximum of objectivity to the visual assessment, this was performed simultaneously by five subjects and repeated, navigating the vessel at a distance between 20 and 30 nautical miles (1 nautical mile = 1852 meters) from the lighthouse on Tino Island.

Considering that the height of the light H above sea level is 117 m and that the observer is placed at a height h of about 4.7 m (= 3 m + 1.7 m), the geographical range D is estimated at 26.5 nautical miles through the following relation [18]:

$$D = 2.04\left(\sqrt{h} + \sqrt{H}\right). \quad (1)$$

In the worst case, the source was visible from all subjects up to a distance of 26.6 miles and at a distance of 27.4 nautical miles was no longer visible by any observer. In the best case, the source was visible from three subjects up to 28.5 miles. D values greater than the mentioned observations may depend on refractive phenomena in the atmosphere. Therefore the distance range is definitely greater than 26.5 nautical miles and it can reasonably be set equal to 27 nautical miles. An important observation is that all subjects indicated that the flashes were sharp and well distinguishable from the context.

Owing to vibrations caused by the engine and the roll/pitch of the vessel, it was not possible to perform measurements with the instrumentation described in the

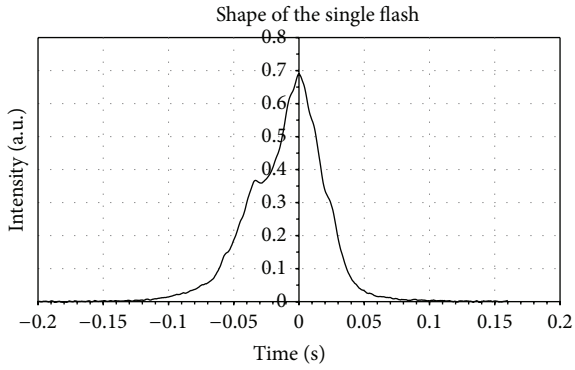

Figure 8: Average time trend ("form") of each flash intensity.

next section. For this reason some photometric measurements were executed from the ground with the purpose of quantifying the optical characteristics of the lighthouse emission.

5.2. Qualitative Analysis: Beam Width and Light Intensity Assessment from the Ground. In the night between 13 and 14 May, 2013, quantitative measurements of shape and duration of the flashes were carried out from the mainland. These measurements were performed from a height of about 50 m above sea level at a distance of 7.44 km from the lighthouse itself. Due to the angular aperture of the beam, it was fully visible even if the observation did not occur exactly at the same height of the lighthouse source (which is placed at 117 m above sea level).

The lighthouse was pointed through a telescope (Meade STX90, with pupil diameter $D = 90$ mm, focal length $F = 1250$ mm, f-number $f/13.8$). The telescope STX90 has two outputs: one (*output 1*) for an eyepiece for direct vision and one (*output 2*) for shooting photos or video; a folding mirror allows selecting the desired output. Thanks to a special adapter a photodiode was mounted on *output 2* and the photodiode output, properly preamplified, was displayed on an oscilloscope (TDS3032 Tektronic), which also had the ability to save the resulting track on the disc. Several temporal shapes of the flashes were recorded by means of this equipment.

Averaging the various recorded flash shapes, a fairly reliable shape of the mean flash, shown in Figure 8, was obtained.

It can, therefore, be evinced that the average FWHM duration of a single flash is 0.06 seconds. Given that the system of lenses of the lighthouse is moving at an angular velocity of 24 deg/s, it can easily be obtained that the beam width (FWHM) is 1.44 deg. This value is in good agreement with the estimation calculated during the design phase: about 1.4 deg of beam width.

In order to evaluate the intensity of the light emitted by the lighthouse from the seaside location Fiascherino, the sensor of the experimental apparatus was replaced with a fast calibrated flash luxmeter (LMT, mod. SF100).

Given the difference in altitude (above sea level) of the observation point with respect to the lighthouse (difference = 47 m), the measurement is not performed on the emission peak but at an angular distance of about 0.4 deg from the maximum. According to the emission profile resulting from the simulations, the measured values must be multiplied by a factor R equal to 1.259 to obtain the measurement on the maximum peak.

The maximum illuminance recorded by the sensor is equal to 0.4 lux, which, considering the conversion factor due to the entrance and exit pupil areas of the telescope and its transfer function, leads to an illuminance E_{ts} on the entrance pupil of the telescope equal to 0.00174 lux.

The formula to obtain the *candela* (Cd) value corresponding to an illuminance value at a distance of 7.46 km is [13]

$$I_{7.46\,\mathrm{km}} = R \times E_{ts} \times 7460^2 = 122000\,\mathrm{Cd}. \quad (2)$$

In order to be able to estimate the luminous intensity at the exit of the lens, it is essential to assess the averaged transparency of the atmosphere in the 7.46 examined kilometres at the time of measurement. This transparency is affected by the quantity of suspension in the atmosphere (fog, humidity, etc.).

In practice the output intensity I_0 from the lantern and the intensity $I_{7.46\,\mathrm{km}}$ at 7.46 km of distance are related by the Lambert-Beer formula:

$$I_{7.46\,\mathrm{km}} = I_0 e^{-\mu_e \cdot 7.46}, \quad (3)$$

where μ_e is the extinction coefficient in km^{-1}.

In order to determine the extinction coefficient, it is necessary to refer to the atmospheric condition during that night. In fact the data in "IALA Recommendation E-200-2 On Marine Signal Lights Part 2—Calculation, definition and notation of luminous range" [10] report the relation between extinction coefficient and moisture: extinction coefficients versus wavelength for the marine aerosol model for different relative humidity values and constant number density of particles. The data available for the day 13/05/2013, measured in the hinterland (Luni-Sarzana meas. station, historical meteorological database, http://www.ilmeteo.it/) are: average temperature 19°C, average visibility 10 km.

Reasonably, on the sea and at night, when the measurements were made, it can be supposed to have humidity over the maximum humidity recorded, since the data refer to the hinterland. Assuming a humidity value between 90 and 95% (on the coast, in Livorno, 65 km south, 94% humidity that night), at visible wavelengths, the extinction coefficient results are between 0.25 and 0.35, on average equal to 0.3. This leads to estimating the output luminous intensity from the lens as follows:

$$I_0 = \frac{I_{7.46\,\mathrm{km}}}{e^{-\mu_e \cdot 7.46}} = \frac{122'000\,\mathrm{Cd}}{e^{-0.3 \cdot 7.46}} = 1'144'000\,\mathrm{Cd}. \quad (4)$$

This quantity must absolutely be considered a rough estimation since the atmospheric attenuation varies dramatically with the weather conditions at the time and therefore the value may vary greatly within the same night. However, the documentation IALA and in particular the "Recommendation E-200-2 ON Marine Signal Lights Part 2—Calculation, definition and notation of luminous range" [10] show that

the luminous intensity for a distance range around 26 nautical miles is greater than 10^6 Cd, in agreement with the observations made from the ship (Section 5.1).

6. Conclusion

All surveys, visual and quantitative, confirm both the substantial agreement between implementation and project and the effectiveness of the new source as a possible substitute, in maritime lighthouses, of incandescent lamps. The new sustainable LED device offers significant advantages reducing energy consumption, improving reliability, and limiting maintenance costs. There is a little disadvantage consisting in a decrease in the luminous intensity of about 30%, which slightly changes the theoretical range of the LED-based lamp, although marine observations show no substantial modification of the luminous range with respect to the case of incandescent lamp.

The proposed system is also open to possible modifications that can further improve performance, particularly with regard to power-saving and reliability. A subsequent engineering work may also lead to greater compactness of the source (with performance advantages) and a decrease in costs. Finally, the availability of new LEDs with higher efficiencies and/or increasing luminous power could allow a further enhancement in performance.

Conflict of Interests

The authors declare that there is no conflict of interests regarding the publication of this paper.

Acknowledgments

The authors wish to thank the Italian Navy and especially the Technical Office of Lighthouses ("Ufficio Tecnico dei Fari," MARITECNOFARI La Spezia), in particular Dir. C.V. Barbetta, T. V. Napolione, Eng. Chianura, and Mr. Petacco. The authors wish to thank the CNR-INO technicians: Mr. M. D'Uva, Mr. S. Acciai, and Mr. M. Pucci for their help in the construction of the prototype.

References

[1] Y. Ohno, "Color rendering and luminous efficacy of white LED spectra," in *4th International Conference on Solid State Lighting*, vol. 5530 of *Proceedings of SPIE*, pp. 88–98, Bellingham, Wash, USA, August 2004.

[2] R. Lenk and C. Lenk, *Practical Lighting Design with LEDs*, IEEE Press Series on Power Engineering, John Wiley & Sons, New York, NY, USA, 2011.

[3] "Professional Lighting Design," Magazine for Professional Lighting Design, VIA, 2012.

[4] Luce&design., *lighting Review*, Tecniche Nuove, Milano, Italy, 2012.

[5] S. Trevor and M. Mathers, *The Basis for Efficient Lighting—A Reference Manual for Training in Efficient Lighting Principles*, National Framework for Energy Efficiency, Australia, 1st edition, 2009.

[6] İ. Şahin and S. C. İnan, "Probe of unparticles at the LHC in exclusive two lepton and two photon production via photon-photon fusion," *Journal of High Energy Physics*, no. 9, article 69, 2009.

[7] R. Haitz and J. Y. Tsao, "Solid-state lighting: "the case" 10 years after and future prospects," *Physica Status Solidi (A): Applications and Materials Science*, vol. 208, no. 1, pp. 17–29, 2011.

[8] R. Haitz, F. Kish, J. Tsao, and J. Nelson, "The case for a national research program on semiconductor lighting," in *Proceedings of the Annual Forum of the Optoelectronics Industry Development Association*, Washington, DC, USA, 1999.

[9] "IALA Recommendation E-200-2—Notation of Luminous Intensity and Range," International Association of Marina Aids to Navigation and Lighthouse Authorities AISM-IALA, 2008.

[10] *IALA Recommendation E-200-2 on Marine Signal Lights. Part 2—Calculation, Definition and Notation of Luminous Range*, International Association of Marina Aids to Navigation and Lighthouse Authorities AISM-IALA, 1st edition, 2008.

[11] D. Jafrancesco, L. Mercatelli, P. Sansoni et al., "Optical design of a LED lamp for a lighthouse of maritime signaling," submitted to International Journal of Photoenergy for the special issue on "Solid-State Lighting with High Brightness, High Efficiency, and Low Cost".

[12] D. Jafrancesco, L. Mercatelli, P. Sansoni, D. Fontani, E. Sani, and F. Francini, "Lighting device comprising an array of optoelectronic sources," European Patent EP 2671755A1, 2013.

[13] C. DeCusatis, *Handbook of Applied Photometry*, AIP Press, Woodbury, NY, USA, 1997.

[14] D. Killinger, J. H. Churnside, and L. S. Rothman, "Atmospheric optics," in *Handbook of Optics*, M. Bass, Ed., chapter 44, McGraw-Hill, New York, NY, USA, 1995.

[15] D. DiLaura, K. Houser, R. Mistrick, and G. Steffy, *The Lighting Handbook*, Illuminating Engineering Society of North America, 10th edition, 2011.

[16] J. Gunn, R. Blackburn, and P. J. Taylor, *Forensic Psychiatry: Clinical, Legal and Ethical Issues*, Butterworth-Heinemann, Oxford, UK, 1993.

[17] R. Ganslandt and H. Hofmann, *Handbook of Lighting Design*, ERCO Edition, 1992.

[18] *IALA Aids to Navigation Manual NAVGUIDE*, Saint-Germain-en-Laye, France, AISM-IALA, 2010.

Hindawi Publishing Corporation
International Journal of Photoenergy
Volume 2014, Article ID 796253, 7 pages
http://dx.doi.org/10.1155/2014/796253

Research Article

Performance of InGaN Light-Emitting Diodes Fabricated on Patterned Sapphire Substrates with Modified Top-Tip Cone Shapes

Hsu-Hung Hsueh,[1] Sin-Liang Ou,[2] Chiao-Yang Cheng,[3] Dong-Sing Wuu,[2] and Ray-Hua Horng[1,4]

[1] *Graduate Institute of Precision Engineering, National Chung Hsing University, 250 Kuo Kuang Road, Taichung 40227, Taiwan*
[2] *Department of Materials Science and Engineering, National Chung Hsing University, Taichung 40227, Taiwan*
[3] *Wafer Works Optronics Corporation, Taoyuan 32542, Taiwan*
[4] *Advanced Optoelectronic Technology Center, National Cheng Kung University, Tainan 70101, Taiwan*

Correspondence should be addressed to Ray-Hua Horng; huahorng@nchu.edu.tw

Received 14 February 2014; Revised 5 June 2014; Accepted 6 June 2014; Published 19 June 2014

Academic Editor: Hao-Chung Kuo

InGaN light-emitting diodes (LEDs) were fabricated on cone-shaped patterned sapphire substrates (PSSs) by using low-pressure metalorganic chemical vapor deposition. To enhance the crystal quality of the GaN epilayer and the optoelectronic performance of the LED device, the top-tip cone shapes of the PSSs were further modified using wet etching. Through the wet etching treatment, some dry-etched induced damage on the substrate surface formed in the PSS fabrication process can be removed to achieve a high epilayer quality. In comparison to the LEDs prepared on the conventional sapphire substrate (CSS) and cone-shaped PSS without wet etching, the LED grown on the cone-shaped PSS by performing wet etching for 3 min exhibited 55% and 10% improvements in the light output power (at 350 mA), respectively. This implies that the modification of cone-shaped PSSs possesses high potential for LED applications.

1. Introduction

In recent years, InGaN light-emitting diodes (LEDs) have been used in a wide range of optoelectronic applications such as traffic signals, automobiles, full-color displays, solid-state lighting, and backlights of liquid-crystal displays [1–3]. To apply for these applications, an LED device with high luminescence efficiency is required. Nevertheless, depositing a GaN epilayer on lattice-mismatched substrates consisting of sapphire and silicon carbide has resulted in a high threading dislocation (TD) density with a range from 10^9 to 10^{11} cm^{-2} [4, 5]. The high TD density created in the GaN epilayer causes a considerable deterioration of LED performance, including electron mobility, device lifetime, and the quantum efficiency of radiative recombination. Consequently, decreasing the TD density may be a key process in achieving high-efficiency LEDs.

To reduce the TD density of the GaN epilayer to a range of 10^6-10^7 cm^{-2}, several methods including epitaxial lateral overgrowth (ELOG), pendeoepitaxy, and facet-controlled ELOG have been developed. Moreover, because of its single-growth process with no interruption, the patterned sapphire substrate (PSS) technique is another promising method for achieving a GaN epilayer with high crystal quality. However, as the GaN epilayer is grown on PSS, a long period is required for merging the GaN epilayers grown on etched and nonetched sapphire and subsequently obtaining a smooth film surface. Based on previous reports [6–8], InGaN/GaN epilayers with high crystal quality can be achieved by using metalorganic chemical vapor deposition (MOCVD) on a

cone-shaped PSS. At the first step of GaN growth on a cone-shaped PSS, the epitaxial film is merely deposited on the flat basal of the sapphire substrate. Furthermore, the GaN growth on the cone regions has no preferential orientation. This indicates that the growth time of a GaN epilayer with a smooth surface on a cone-shaped PSS is less than that required for using the conventional PSS.

In this study, cone-shaped PSSs were fabricated using dry and wet etching processes and then employed for growing InGaN LED epitaxial structures. In addition, to improve the epilayer quality and LED performance, the wet etching process was applied to modify the top-tip shape of the PSSs by changing the etching time. The epilayer quality, light extraction characteristic, and optoelectronic performance were investigated in detail for these InGaN LEDs fabricated on PSSs with modified top-tip cone shapes.

2. Experimental Procedure

For the fabrication of PSSs with modified top-tip cone shapes, the dry and wet etching processes were employed in sequence, which are described as follows. First, a thick photoresist was deposited on the (001) sapphire through spin-coating, and then a thermal photoresist reflow process was used to create the cone-shaped pattern array. The photoresist array was used as the mask layer to transfer the pattern on the sapphire by applying an inductively coupled plasma reactive ion etching (ICP-RIE) system using reactive Cl_2 gas. The diameter, interval, and height of each cone-shaped pattern were set to 2.4, 0.5, and 1.5 μm, respectively. After performing ICP-RIE, the cone-shaped PSSs were further chemically etched using a mixture of $H_2SO_4 : H_3PO_4$ (3 : 1) solution at 250°C for 3, 5, 7, and 10 min to form the various top-tip shapes. To clean the substrate surface, these PSSs were soaked in the $H_2SO_4 : H_2O_2$ (3 : 1) solution at 120°C for 10 min and in deionized water at room temperature for 10 min in sequence.

For growing the LED epitaxial structure, the epilayers were on these PSSs and on a conventional sapphire substrate (CSS) employed as the contrast sample by using low-pressure MOCVD. The LED epitaxial structure included a 3 μm thick layer of undoped GaN (u-GaN), a 2 μm thick layer of n-type GaN:Si, 6 periods of InGaN/GaN multiple quantum wells, a 100 nm thick p-type AlGaN layer, and a 0.2 μm thick p-type GaN:Mg layer. To fabricate the LED device, a 24 × 45 mil.^{2} mesa pattern was defined and prepared using standard photolithography and dry etching processes. Subsequently, the ITO film used as the transparent conducting layer was deposited on the p-type GaN layer. Finally, the Cr/Au metal was prepared as both the n- and p-pad electrodes.

The epilayer quality of the flat u-GaN was measured using X-ray diffraction (XRD) combined with the analyses of the (002) and (102) planes. The surface morphology and pattern feature of these PSSs were observed using scanning electron microscopy (SEM). The microstructure and electron diffraction pattern of the GaN epilayers grown on PSSs were investigated using transmission electron microscopy (TEM). The typical current-voltage (I-V) characteristic of the fabricated InGaN LED device was analyzed using a semiconductor parameter analyzer (Keithley, 2400 sourcemeter), and the measurement of light output power was conducted using a calibrated integrating sphere.

3. Results and Discussion

Figure 1 shows the surface morphologies of the fabricated PSSs with various cone shapes. Figure 1(a) presents the cross-sectional SEM image of the cone-shaped PSS that was not subjected to the wet etching process. We determined that the actual diameter and height of each cone-shaped pattern were 2.421 and 1.488 μm, respectively. The plane-view SEM images of the cone-shaped PSSs after further wet etching treatments administered using etching times of 3, 5, 7, and 10 min are shown in Figures 1(b), 1(c), 1(d), and 1(e), respectively. After conducting the wet etching process for 3 min, the top-tip surface of the cone pattern was smooth. By increasing the etching time to 5–10 min, we observed that the top-tip shape became increasingly angular. Additionally, the diameter of each cone pattern was enlarged and the interval between these patterns was decreased as the etching time was increased. Furthermore, inclined planes were formed on the sidewalls of the patterns when the etching time was increased, particularly for the samples that underwent 7–10 min of wet etching (Figures 1(d) and 1(e)).

The crystal quality of the GaN epilayer was evaluated using the full-width at half-maximum (FWHM) values for the XRD rocking curves. The XRD rocking curves derived on the GaN (002) and GaN (102) planes of all the samples are displayed in Figures 2(a) and 2(b), respectively. When the GaN epilayer was grown on the CSS, the FWHM values at the (002) and (102) planes were determined to be 412 and 593 arcsec, respectively. After growing the GaN epilayers on the PSSs by performing wet etching for 0, 3, 5, 7, and 10 min, the FWHM values at the (002) plane were analyzed and determined to be 318, 272, 279, 293, and 305 arcsec, respectively. The FWHM values at the (102) plane of the GaN epilayers deposited on these PSSs were 362, 285, 292, 322, and 336 arcsec, respectively. The crystal quality of the GaN epilayer can clearly be improved by adopting the design for a cone-shaped PSS. In addition, we observed that the crystal quality of the GaN epilayer was further enhanced by performing the wet etching treatment on the PSS. According to our knowledge, some dry-etched induced damage on the substrate surface occurred when the ICP-RIE process was conducted to fabricate the PSS. Consequently, by performing the wet etching treatment on the PSS, both the modification of the top tip of the cone-shaped PSS and the removal of the dry-etched induced damage can be achieved. This is the reason that the crystal quality of the GaN epilayer was further improved by using the cone-shaped PSS combined with wet etching treatment. In addition, as mentioned previously, the inclined planes gradually formed on the sidewalls of the PSS as the wet etching time increased (Figure 1). These inclined planes clearly formed on the PSSs when wet etching was performed for 7–10 min. The result indicates that the epilayer can most likely be deposited on both the bottom (c-plane)

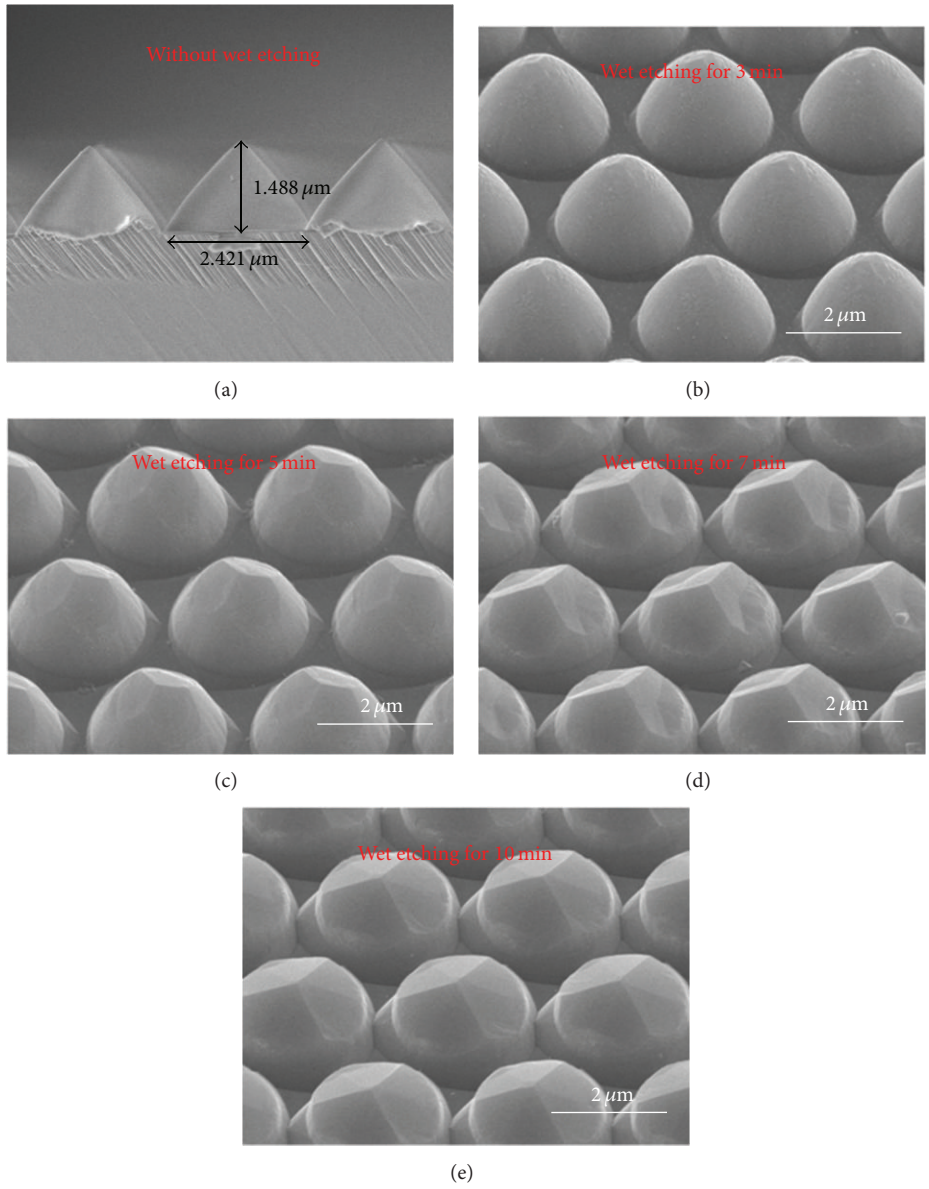

FIGURE 1: (a) Cross-sectional SEM image of cone-shaped PSS without treatment by wet etching and plane-view SEM images of cone-shaped PSSs subjected to wet etching for (b) 3 min, (c) 5 min, (d) 7 min, and (e) 10 min.

and the angular cone region at the initial stage, which results in an increased dislocation density and the deterioration of crystal quality in the epilayer.

Figures 3(a), 3(b), and 3(c) display the cross-sectional TEM images of the GaN epilayers grown on the PSSs subjected to wet etching for 0, 3, and 10 min, respectively. In comparison to Figures 3(a) and 3(c), an obvious difference can be observed in Figure 3(b) (i.e., the formations of protrusions and voids on the sidewalls of the cone pattern). Furthermore, we determined that no protrusion or void formed on the sidewalls of the cone pattern when the PSSs were wet-etched for 0, 5, 7, and 10 min (the images of the GaN epilayers grown on the PSSs subjected to wet etching for 5 and 7 min are not shown here). This indicates that the special structure feature only appears in the GaN epilayer prepared on a PSS subjected to wet etching treatment for 3 min. In addition, the right protrusion in Figure 3(b) was chosen to be examined using a selected area electron diffraction pattern, as shown in Figure 3(d). The single crystalline electron diffraction dots in Figure 3(d) indicate that the protrusion possesses the $[\bar{1}101]$ zone axis of GaN. Figures 4(a) and 4(b) show the cross-sectional SEM images before and after epilayer growth occurred on the PSS subjected to wet etching for 3 min, respectively. We observed that the sidewalls of the cone patterns were smooth before wet etching, and the protrusions and voids were formed during epilayer growth. When we chose one of the cone patterns in Figure 4(b) (marked with a green circle) and enlarged the SEM magnification, the features of the protrusions and voids could be observed clearly, as shown in Figure 4(c).

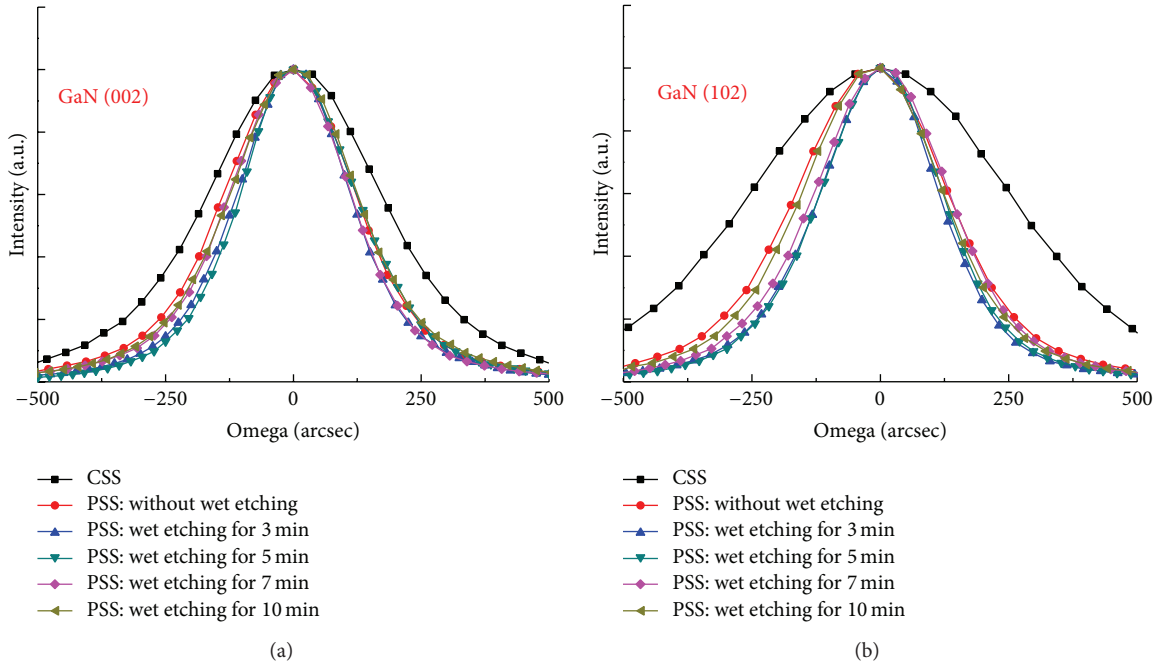

FIGURE 2: XRD FWHM values for the (a) (002) and (b) (102) reflections of GaN epilayers prepared on the CSS and various cone-shaped PSSs.

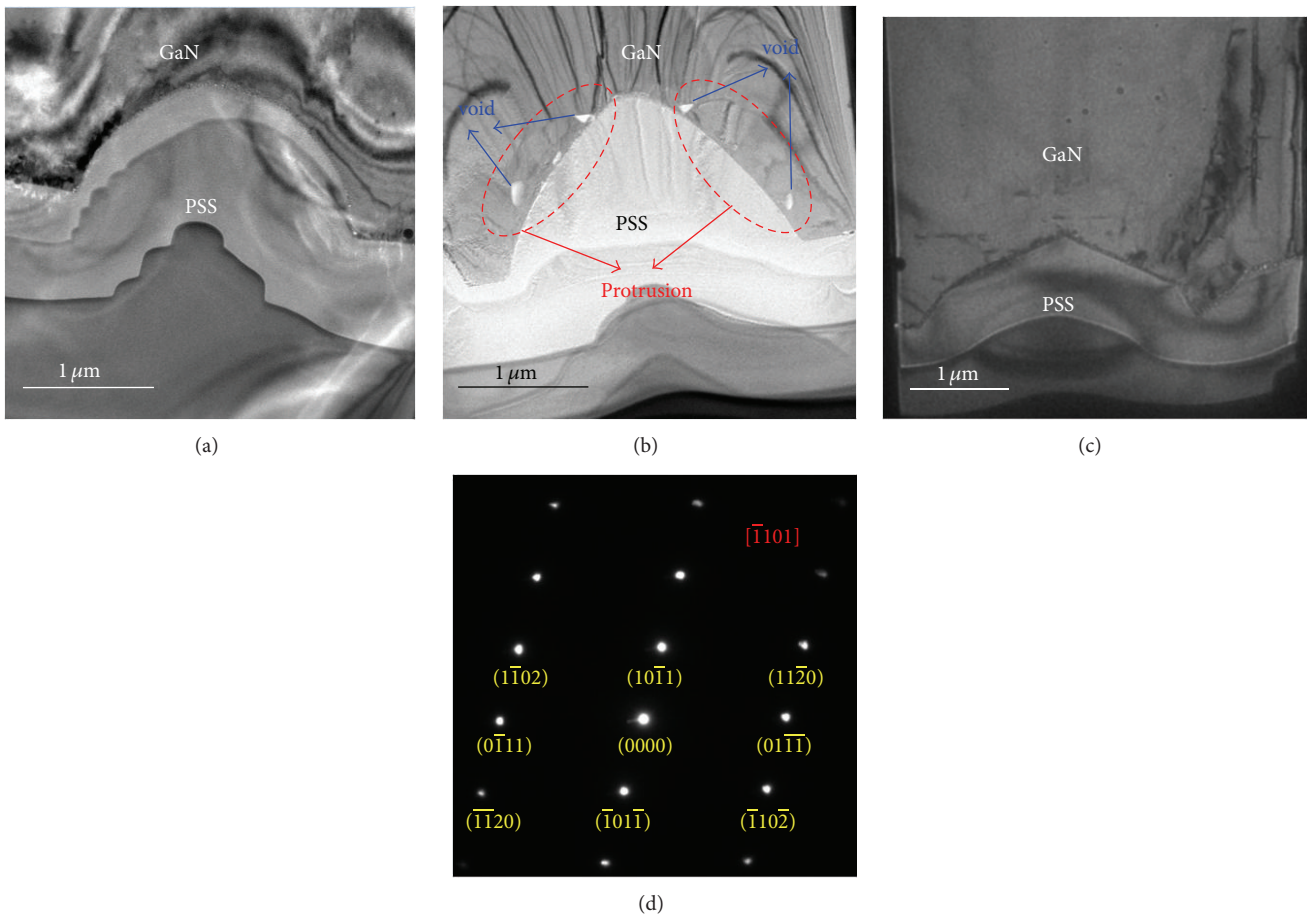

FIGURE 3: Cross-sectional TEM images of the GaN epilayers grown on the PSSs subjected to wet etching for (a) 0 min, (b) 3 min, and (c) 10 min. (d) Selected area electron diffraction pattern of the right protrusion in (b).

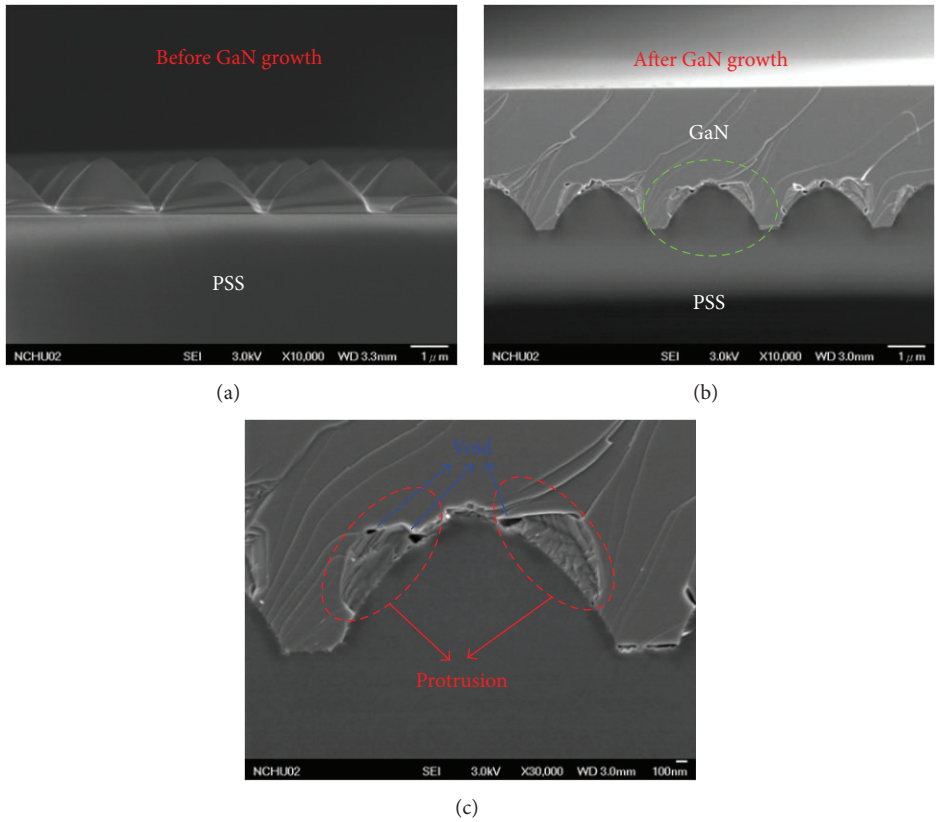

FIGURE 4: Cross-sectional SEM images (a) before and (b) after epilayer growth on PSS subjected to wet etching for 3 min and (c) SEM image taken at the cone pattern in (b) (marked with green circle) with higher magnification.

In this study, the formations of protrusions and voids were observed in the GaN growth on the cone-shaped PSS subjected to wet etching for 3 min. The effects of the protrusions and voids on the epilayer quality and LED device performance are discussed. When the PSSs were employed, the GaN growth primarily occurred in the bottom regions (*c*-plane), and the ELOG process was used to merge the GaN films [9–11], leading to an improvement in the crystal quality of GaN epilayer. As the wet etching process was performed on the cone-shaped PSS for 3 min, the indistinct angular planes formed on the sidewalls of the cone patterns. Subsequently, after growing the GaN epilayer on this PSS, the protrusions and voids were generated on the sidewalls of the cone patterns. Park et al. have proposed a detailed investigation of the microstructures of GaN epilayer grown on the cone-shaped PSS [12]. It indicates that the recrystallized GaN islands and nanovoids were formed on the inclined surface of the cone-shaped PSS. Based on our observation, the features of the "recrystallized GaN islands and nanovoids" presented in Park et al. research are very similar to those of the "protrusions and voids" observed in our study. Additionally, the recrystallized GaN island was examined using a selected area electron diffraction pattern via the TEM measurement, and it revealed that the electron diffraction dots generated from the recrystallized GaN island possessed the $[\bar{1}101]$ zone axis of GaN. Consequently, we can confirm that the protrusions observed in our work are equivalent to the recrystallized GaN islands found in Park et al. research. According to Park et al. investigation, there is a 9° rotation of the recrystallized GaN island to GaN epilayer and Al_2O_3 substrate, leading to further decrease in the lattice mismatch at the interfaces of Al_2O_3/recrystallized GaN island and recrystallized GaN island/GaN epilayer. (Here, the GaN epilayer is meant for the GaN film with (002) growth orientation deposited on the recrystallized GaN island.) The 9° rotation would result in a significant reduction of the misfit dislocation from the interface between the recrystallized GaN island and GaN epilayer. Furthermore, the crystal quality of GaN epilayer can be improved via the formation of recrystallized GaN islands. This implies that the protrusions observed in our study also play a key role in improving the quality of GaN epilayer and optoelectronic performance of LED. Besides, the enhancement in light extraction by embedding or forming voids in the LED structure has been reported in several studies [13–15]. Based on the aforementioned discussion, the formations of protrusions and voids in our work are indeed helpful for the improvements of epilayer quality and LED device performance. The device performance was discussed later, as shown in Figure 6. As discussed in Figure 2, with increasing the wet etching time on the PSS, the epilayer could be grown on both the bottom and the angular cone region at the initial stage, causing a degradation of the epilayer quality.

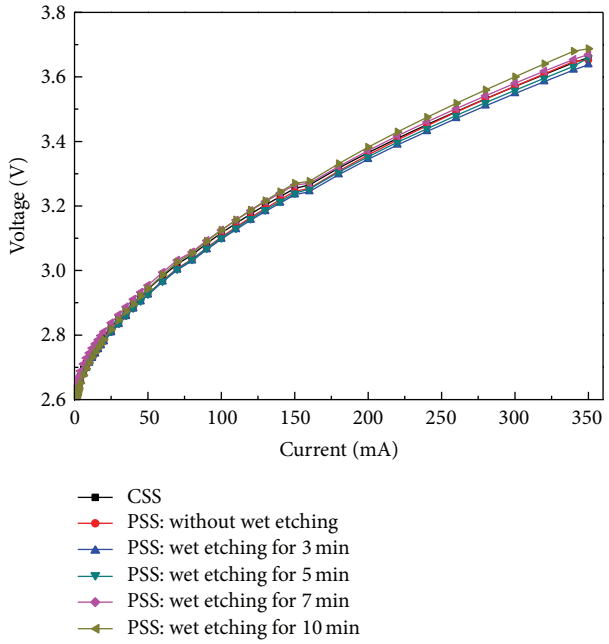

Figure 5: *I-V* characteristics of the InGaN LEDs prepared on the CSS and various cone-shaped PSSs subjected to wet etching from 0 to 10 min.

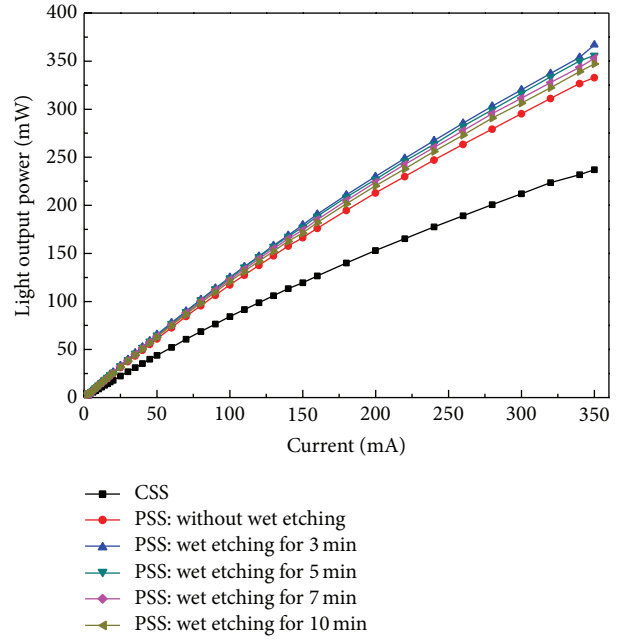

Figure 6: Light output power as a function of injection current of the InGaN LEDs prepared on the CSS and various cone-shaped PSSs subjected to wet etching from 0 to 10 min.

Moreover, the disappearance of GaN protrusions is the other reason for the degradation of the epilayer quality.

Figure 5 presents the *I-V* characteristics of the LED samples fabricated on both the CSS and various cone-shaped PSSs. As the injection current increased to 350 mA, the forward voltages of the LED samples prepared on the CSS and PSSs subjected to wet etching for 0, 3, 5, 7, and 10 min were determined to be 3.66, 3.65, 3.64, 3.66, 3.67, and 3.69 V, respectively. Figure 6 shows the light output power as a function of injection current ranging from 0 to 350 mA for the InGaN LEDs fabricated on both the CSS and various cone-shaped PSSs. As shown in Figure 2, the crystal quality of the GaN epilayer was enhanced efficiently by using the cone-shaped PSSs. A similar trend was observed in the device performance. Compared with the LED prepared on the CSS, the light output power of the LED grown on the cone-shaped PSS was substantially improved. Moreover, the light output power of the LED was further enhanced when the PSS was treated with wet etching because of the improvement in crystal quality of the GaN epilayer. Nevertheless, as the PSS was wet-etched for 5–10 min, the LED device exhibited a slight decrease in light output power. This was attributed to the deterioration of epilayer quality. At an injection current of 350 mA, the light output power of the LED fabricated on a CSS was measured to be 237 mW. In addition, the light output powers of the LEDs fabricated on PSSs subjected to wet etching for 0, 3, 5, 7, and 10 min were determined to be 333, 367, 356, 353, and 347 mW, respectively. Compared with the LEDs prepared on the CSS and PSS without wet etching, the LED grown on the PSS subjected to wet etching for 3 min exhibited 55% and 10% improvements in light output power (at 350 mA), respectively.

4. Conclusion

In summary, InGaN LEDs were grown on the PSSs with modified top-tip cone shapes. The effects of various cone shapes on the epilayer quality and device performance were also investigated. Performing the wet etching treatment on the cone-shaped PSS resulted in the modification of the top tip of the pattern shape and the removal of dry-etched induced damage on the substrate surface. This led to the enhanced crystal quality of GaN growth and improved device performance. The optimal wet etching time for the cone-shaped PSSs was determined to be 3 min. The LED device prepared on this PSS demonstrated the most improvement in both epilayer quality and light extraction compared with those demonstrated by the other PSSs. This indicates that using the wet etching treatment on the cone-shaped PSSs is potentially useful in LED applications.

Conflict of Interests

The authors declare that there is no conflict of interests regarding the publication of this paper.

Acknowledgments

This work was supported by the Ministry of Economic Affairs under Grant no. 102-E0605 and National Science Council (Taiwan) under the Contract no. 102-2221-E-005-072-MY3.

References

[1] S. Nakamura, T. Mukai, and M. Senoh, "Candela-class high-brightness InGaN/AlGaN double-heterostructure blue-light-emitting diodes," *Applied Physics Letters*, vol. 64, no. 13, pp. 1687–1689, 1994.

[2] H. X. Jiang, S. X. Jin, J. Li, J. Shakya, and J. Y. Lin, "III-nitride blue microdisplays," *Applied Physics Letters*, vol. 78, no. 9, pp. 1303–1305, 2001.

[3] C. Pan, C. Lee, J. Liu, G. Chen, and J. Chyi, "Luminescence efficiency of InGaN multiple-quantum-well ultraviolet light-emitting diodes," *Applied Physics Letters*, vol. 84, no. 25, pp. 5249–5251, 2004.

[4] X. A. Cao, S. F. LeBoeuf, M. P. D'Evelyn et al., "Blue and near-ultraviolet light-emitting diodes on free-standing GaN substrates," *Applied Physics Letters*, vol. 84, no. 21, pp. 4313–4315, 2004.

[5] M. Iwaya, T. Takeuchi, S. Yamaguchi, C. Wetzel, H. Amano, and I. Akasaki, "Reduction of etch pit density in organometallic vapor phase epitaxy-grown GaN on sapphire by insertion of a low-temperature-deposited buffer layer between high-temperature-grown GaN," *Japanese Journal of Applied Physics*, vol. 37, no. 3B, pp. L316–L318, 1998.

[6] Y. B. Tao, T. J. Yu, Z. Y. Yang et al., "Evolution and control of dislocations in GaN grown on cone-patterned sapphire substrate by Metal Organic Vapor PhaseEpitaxy," *Journal of Crystal Growth*, vol. 315, no. 1, pp. 183–187, 2011.

[7] M. T. Wang, F. Brunner, K. Y. Liao, Y. L. Li, S. H. Tseng, and M. Weyers, "Optimization of GaN wafer bow grown on cone shaped patterned sapphire substrates," *Journal of Crystal Growth*, vol. 363, pp. 109–112, 2013.

[8] J. Lee, D. Lee, B. Oh, and J. Lee, "Comparison of InGaN-based LEDs grown on conventional sapphire and cone-shape-patterned sapphire substrate," *IEEE Transactions on Electron Devices*, vol. 57, no. 1, pp. 157–163, 2010.

[9] J. Lee, J. T. Oh, Y. C. Kim, and J. Lee, "Stress reduction and enhanced extraction efficiency of GaN-based LED grown on cone-shape-patterned sapphire," *IEEE Photonics Technology Letters*, vol. 20, no. 18, pp. 1563–1565, 2008.

[10] K. Hiramatsu, K. Nishiyama, M. Onishi et al., "Fabrication and characterization of low defect density GaN using facet-controlled epitaxial lateral overgrowth (FACELO)," *Journal of Crystal Growth*, vol. 221, no. 1–4, pp. 316–326, 2000.

[11] H. Lahrèche, P. Vennéguès, B. Beaumont, and P. Gibart, "Growth of high-quality GaN by low-pressure metal-organic vapour phase epitaxy (LP-MOVPE) from 3D islands and lateral overgrowth," *Journal of Crystal Growth*, vol. 205, no. 3, pp. 245–252, 1999.

[12] J. S. Park, J. M. Yang, K. J. Park et al., "Transmission electron microscopy study of microstructural properties and dislocation characterization in the GaN film grown on the cone-shaped patterned Al_2O_3 substrate," *Microscopy*, vol. 63, no. 1, pp. 15–22, 2014.

[13] C. Cho, M. Kwon, I. Park et al., "High-efficiency light-emitting diode with air voids embedded in lateral epitaxially overgrown GaN using a metal mask," *Optics Express*, vol. 19, no. 4, pp. A943–A948, 2011.

[14] C. H. Chiu, C. C. Lin, H. V. Han et al., "High efficiency GaN-based light-emitting diodes with embedded air voids/SiO_2 nanomasks," *Nanotechnology*, vol. 23, no. 4, Article ID 045303, 2012.

[15] S. M. Kim, K. H. Lee, and G. Y. Jung, "Epitaxial lateral overgrowth on the air void embedded SiO_2 mask for InGaN light-emitting diodes," *CrystEngComm*, vol. 15, no. 31, pp. 6062–6065, 2013.

Hindawi Publishing Corporation
International Journal of Photoenergy
Volume 2014, Article ID 829284, 5 pages
http://dx.doi.org/10.1155/2014/829284

Research Article

Thermal Characteristics of InGaN/GaN Flip-Chip Light Emitting Diodes with Diamond-Like Carbon Heat-Spreading Layers

Pai-Yang Tsai,[1] Hou-Kuei Huang,[1] Chien-Min Sung,[2] Ming-Chi Kan,[2] and Yeong-Her Wang[1]

[1] *Institute of Microelectronics, Department of Electrical Engineering, Advanced Optoelectronic Technology Center, National Cheng Kung University, Tainan 701, Taiwan*
[2] *Department of DLC Technology, RiteDia, Hsin Chu 303, Taiwan*

Correspondence should be addressed to Yeong-Her Wang; yhw@ee.ncku.edu.tw

Received 6 February 2014; Revised 23 April 2014; Accepted 2 June 2014; Published 18 June 2014

Academic Editor: Nelson Tansu

The temperature-dependent optical, electrical, and thermal properties of flip-chip light emitting diodes (FCLEDs) with diamond-like carbon (DLC) heat-spreading layers were investigated. On the basis of the measured results in the 20°C to 100°C temperature range, a significant performance improvement can be achieved for FCLEDs with DLC heat-spreading layers (DLC-FCLED) compared with FCLEDs without DLC heat-spreading layers (non-DLC-FCLED). The external quantum efficiency (EQE) of the DLC-FCLED improves by 9% at an injection current of 1000 mA and a temperature of 100°C. The forward voltage and spectra variations are smaller than those of non-DLC-FCLEDs. The DLC-FCLED provides high efficiency and high stability performance for high-power and high-temperature applications.

1. Introduction

GaN-based light emitter diodes (LEDs) are widely used for automotive lighting, solid-state lighting, and as light engines for other illumination tools [1, 2]. LEDs should operate at high injection currents and employ a large chip size when used for high-power applications. Therefore, the generated heat in LED chip and package is significant and cannot be neglected. The chip characteristics of conventional lateral LEDs are limited by technical problems; that is, the sapphire substrate suffers from poor electric and thermal properties [3]. For flip-chip LEDs (FCLED), both the p and n pads are attached to a high thermal conductivity substrate by eutectic bonding or solder bumps. However, the current crowding is still not improved because the current circuit of the p and n pads is almost the same as conventional lateral LEDs [4]. Therefore, the generated heat in the hot spot of the current crowding area significantly degrades the electric and optical properties of a device. Diamond-like carbon (DLC) possesses high thermal conductivity, thermal diffusivity, and thermal radiation; furthermore, the coefficient of thermal expansion (CTE) of DLC is similar to that of GaN. DLC has very good thermal conductivity (600 W/mK) and thermal diffusivity (370 mm^2/s), that is, 1.5 and 3.3 times higher than that of copper [5, 6]. The DLC can be very effective for heat dissipation and hot spot removal. Therefore, the DLC improves chip performance at high injection current densities [7, 8].

In this study, the DLC was used as a heat-spreading layer between the mirror and eutectic material. For the fabricated DLC-FCLEDs, the temperature-dependent chip performance was discussed and compared with a FCLED without a DLC heat-spreading layer (non-DLC-FCLED).

2. Experimental

The schematic of the LED cross section is shown in Figure 1. The GaN LED epilayers were grown by metal-organic chemical vapor depositions onto (0001) sapphire substrates. The LED structure consisted of a low-temperature 200 nm thick GaN buffer layer, a 2 μm thick undoped GaN layer, a 2 μm thick and highly conductive n-type GaN layer, an InGaN-GaN multiple-quantum-well (MQW) active layer, and a

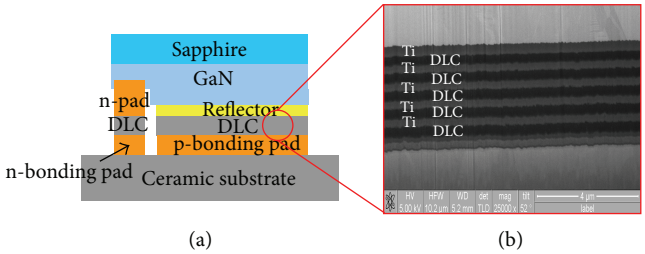

FIGURE 1: (a) Schematics of the FCLED with DLC heat-spreading layer. (b) Cross-sectional DLC heat-spreading layer SEM image for FCLED.

0.5 μm thick p-type GaN layer. A $1 \times 1\,\text{mm}^2$ square isolation structure was created by using an inductively coupled plasma etcher (ICP) for electrical isolation. The p-GaN was etched by an ICP to expose the n-GaN for electrode deposition. Cr/Pt/Au were deposited on the n-GaN as n pads, and the Ni/Ag/Ti/Au metals were deposited on the p-GaN film. These metals acted as the ohmic contact and reflective mirrors formed by electron beam (E-beam) evaporation. The SiO_2 film was used to passivate the sidewall of the LED device through plasma-enhanced chemical vapor deposition. The Ti/DLC (250 nm/200 nm) materials were used as heat-spreading layers by physical vapor deposition after passivation. The use of a Ti-layer can increase the adhesion and electrical conductivity of the DLC heat-spreading layer. Finally, Ti/Ni/AuSn was used as the bonding material layer for die attachment. To measure the temperature dependent on the FCLED characteristics, the FCLED was attached to a ceramic substrate by using AuSn eutectic bonding.

The LED chip was loaded onto a thermal plate composed of a copper stage, thermoelectric cooler, and thermistor. The temperature ranged from 20°C to 100°C for measuring purposes. The optical, spectral, and electric characteristics were measured by using an integrated sphere at various heat sink temperatures.

3. Results and Discussion

The performances of the split-wafer DLC-FCLED and the non-DLC-FCLED were investigated. The light output power, injection current, and forward voltage (L-I-V) characteristics at room temperature are shown in Figure 2. At 350 mA, the forward voltage (V_F) of the DLC-FCLED is 2.88 V, whereas the forward voltage (V_F) of the non-DLC-FCLED is 2.86 V. The current-voltage curves are almost the same. The light output power is 414.2 mW for the DLC-FCLED and 401.3 mW for the non-DLC-FCLED. The corresponding wall-plug efficiencies (light output power/injection current × forward voltage) of DLC-FCLED and non-DLC-FCLED at 350 mA are 41.1% and 40.1%, respectively. No significant difference was observed in the device performance of the DLC-FCLED and non-DLC-FCLED. The heat generated in the epilayers is almost the same.

The light output power of the DLC-FCLED is higher than the non-DLC-FCLED at an injection current of 1,000 mA.

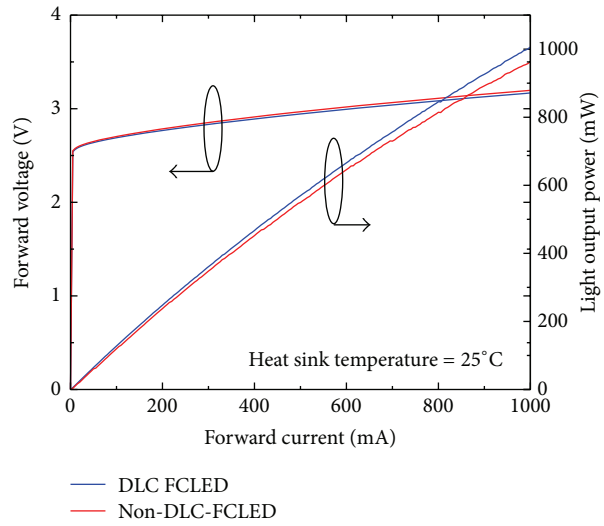

FIGURE 2: L-I-V characteristics of the DLC-VLED and non-DLC-VLED.

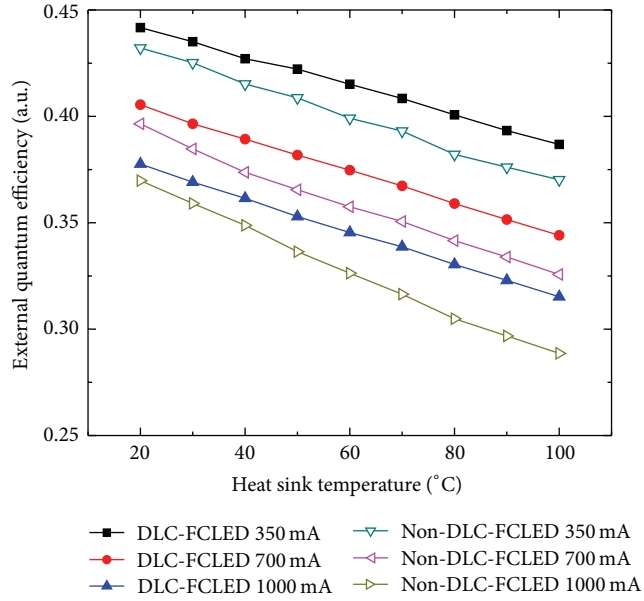

FIGURE 3: Three EQEs of the DLC-FCLED and non-DLC-FCLED as functions of the heat sink temperature at different injection currents (350, 700, and 1,000 mA).

The DLC can provide better thermal conductivity and thermal radiation. Furthermore, the heat of the MQW can be uniformly spread on the DLC film and can be transferred to the ceramic substrate. The light output power can be further improved by using the DLC heat-spreading layers at high injection currents.

Figure 3 shows the external quantum efficiency (EQE, (light output power/$h\nu$)/(injection current/e), where h is the Planck constant, ν is frequency, and e is the elementary charge) of the DLC-FCLED and non-DLC-FCLED as a function of the heat sink temperature at injection currents of 350, 700, and 1,000 mA. At an injection current of 350 mA

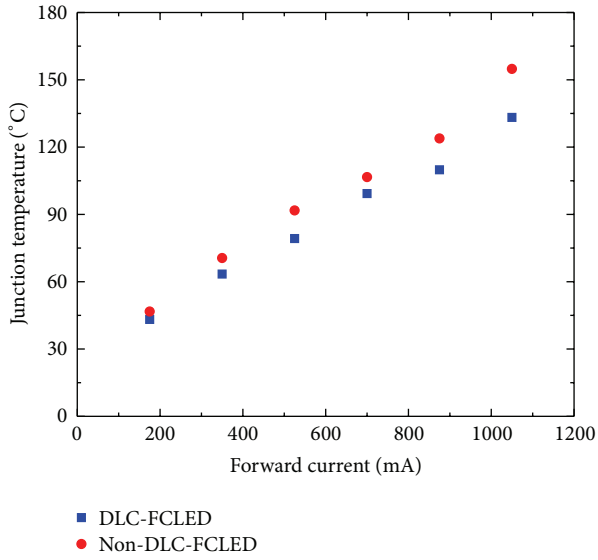

Figure 4: Junction temperature as a function of the injection current for the DLC-FCLED and the non-DLC-FCLED.

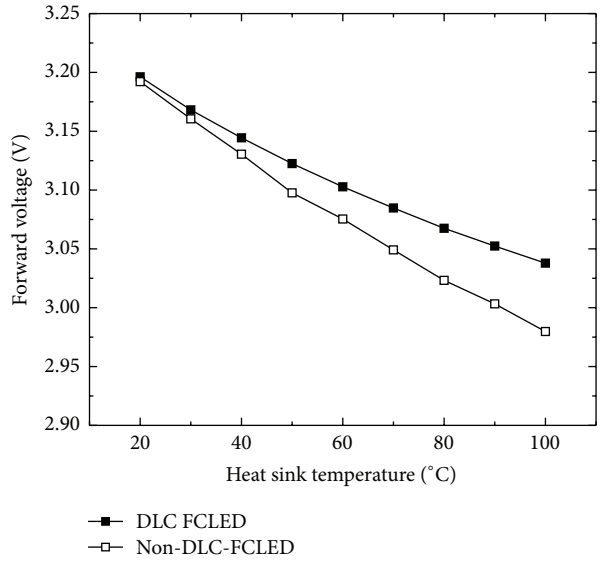

Figure 5: The forward voltage as a function of the heat sink temperature at an injection current of 1,000 mA.

and with a heat sink temperature of 20°C, the EQE of the DLC-FCLED and non-DLC-FCLED are 44.1% and 43.2%, respectively. The EQE of the DLC-FCLED is slightly higher than the EQE of the non-DLC-FCLED. At a heat sink temperature of 100°C, the EQE decreases to 38.6% and 37% for the DLC-FCLED and non-DLC-FCLED, respectively. The EQE of the DLC-FCLED improves by 5%. The heat from the chip can be removed by the DLC heat-spreading layer and ceramic substrate. At an injection current of 1,000 mA and at a heat sink temperature of 20°C, the EQE of the DLC-FCLED and non-DLC-LED decreases by 37.7% and 36.9%, respectively. All sample efficiencies decrease with increasing heat sink temperature. The droop rate of the EQE for the DLC-FCLED was lower than that of the non-DLC-FCLED. The EQE of the non-DLC-FCLED is 36.9% and decreased to 28.8% at 1,000 mA, thus indicating a droop rate of 21.9%. The droop rate of the DLC-FCLED EQE is 16.5%. The effect of the DLC heat-spreading layer on the light extraction performance of the FCLED is significant at high injection currents within a particular heat sink temperature range.

The junction temperatures of the DLC-FCLED and non-DLC-FCLED are measured by the forward voltage method. Figure 4 shows the junction temperature as a function of the injection current for the DLC-FCLED and non-DLC-FCLED. For the non-DLC-LED, the junction temperatures are 70.5 and 154.8°C at 350 and 1,000 mA, respectively. However, the DLC-FCLED exhibited lower junction temperatures with 63.4 and 133.2°C at 350 and 1,000 mA, respectively. Thus, a lower junction temperature is achieved for the DLC-FCLED. This result can be attributed to the better thermal conductivity, thermal diffusivity, and thermal radiation of the DLC. The high thermal diffusivity can effectively remove the generated heat and decrease temperature differences. Therefore, the heat generated at a junction is efficiently spread by the DLC layer on the ceramic substrate. According to the Stefan-Boltzmann equation, the power of black body radiation may be calculated as $5.67 \times 10^{-8}\ T(K)^4\ W/m^2$, and the power radiated is about $0.15\ W/cm^2$. This value is about 5% of the input power of devices.

Figure 5 shows that the forward voltage changes according to the heat sink temperature. The forward voltage decreases with increasing heat sink temperature because of chip heating. At 1,000 mA, the forward voltage of the DLC-FCLED decreases from 3.19 V to 3.03 V with increasing heat sink temperature from 20°C to 100°C. By contrast, the voltage for the non-DLC-FCLED decreases from 3.19 V to 2.97 V. The energy band gap narrows with decreasing forward voltage because of the internally generated heat of the chip. The forward voltage of the DLC-FCLED slightly decreases with increasing heat sink temperature from 20°C to 100°C. This can be attributed to the better thermal dissipation of the DLC heat-spreading layer.

The FCLED with a DLC heat-spreading layer can decrease wavelength shifts with increasing heat sink temperature. The electroluminescence (EL) spectra of the DLC-FCLED and non-DLC-FCLED at various heat sink temperatures and at an injection current of 1,000 mA are shown in Figure 6. The EL intensities decrease with increasing heat sink temperature; this result may be caused by the heating of the chip. The increase in heat sink temperature decreases the energy band gap. The EL spectra are represented by a red shift (Figures 6(a) and 6(b)). The wavelength peak of the DLC-FCLED is 448.4 nm at 20°C, and the EL spectra shifted to 451.9 nm at 100°C. The wavelength shifted by 3.5 nm at heat sink temperatures of 20°C to 100°C. The wavelength peak of non-DLC-FCLED is 448.2 nm at 20°C and its EL spectra shifts to 452.1 nm at 100°C. The wavelength shifted by 3.9 nm in heat sink temperatures between 20°C and 100°C.

To validate the effect of DLC heat-spreading layers, each 10 random selected chips for DLC-FCLED and non-DLC-FCLED were adopted for the junction temperature measurement. As results show in Figure 7 at an injection

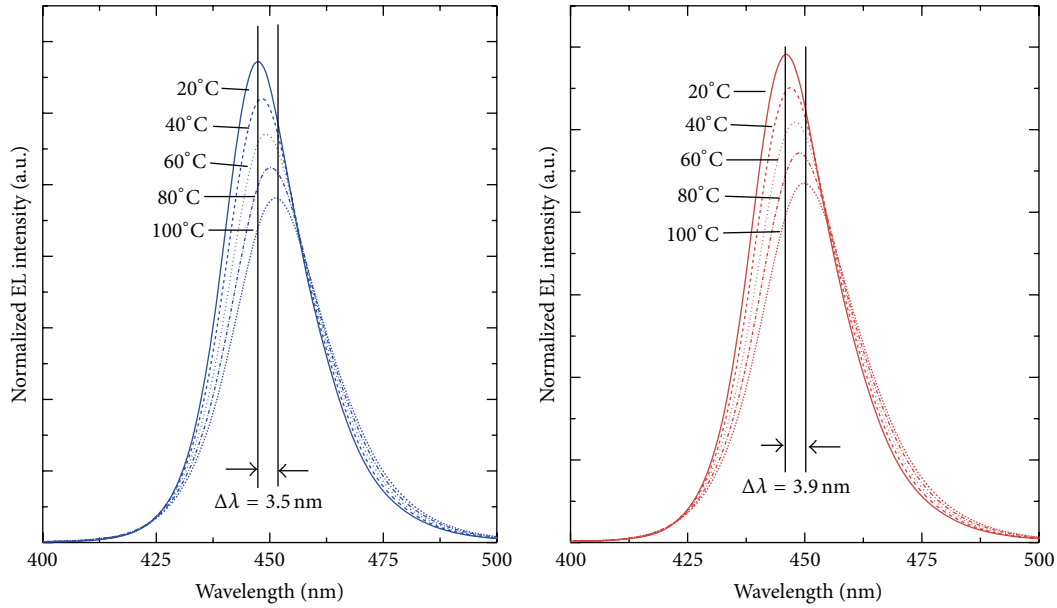

Figure 6: Normalized EL spectra as a function of the heat sink temperature for the (a) DLC-FCLED and (b) non-DLC-FCLED with an injection current of 1000 mA.

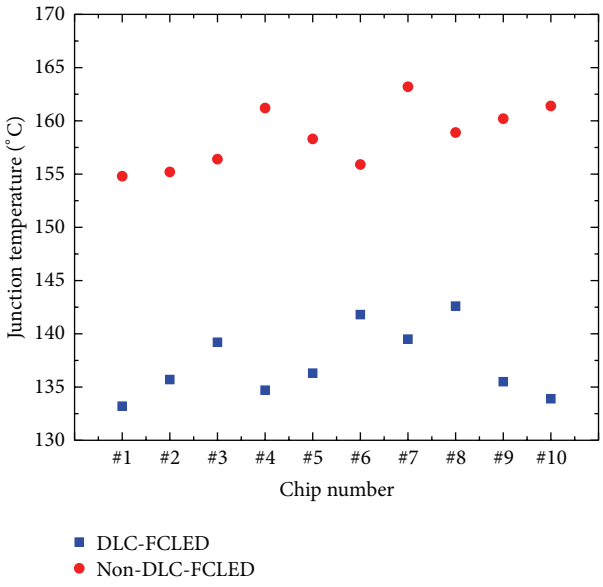

Figure 7: Junction temperature measurements for 10 DLC-FCLED and 10 non-DLC-FCLED chips at an injection current of 1000 mA. The chips were randomly selected.

current of 1000 mA, the FCLED with DLC heat-spreading layer shows the lower junction temperature as compared to that of non-DLC-FCLED. The trend is very consistent which indicates the role of the DLC heat-spreading layers is very effective in heating dissipation and hot spot removal. The performance difference is unlikely to be related to the process variation.

4. Conclusions

This paper demonstrates that the use of DLC heat-spreading layers can improve the optical and thermal properties of FCLEDs. The temperature-dependent device performance of the DLC-FCLED is significantly improved compared with the performance of the non-DLC-FCLED. At an injection current of 1,000 mA, the light output power and EQE are 952.1 mW and 28.8% for the non-DLC-FCLED. By contrast, the light output power and EQE increase to 1,006.3 mW and 31.5%, respectively, for the DLC-FCLED. The forward voltage and EL spectra variations are smaller for the DLC-FCLED. At heat sink temperatures between 20°C and 100°C, the forward voltage decreases by 0.17 V, which is less than the voltage for the non-DLC-FCLED at an injection current of 1,000 mA. The EL spectra of the DLC-FCLED show the red shift of only 3.5 nm. This shift is less than the shift of the non-DLC-FCLED at 0.4 nm. These results demonstrate the stable optical, electrical, and thermal properties of FCLEDs in high-power or high-temperature applications.

Conflict of Interests

The authors declare that there is no conflict of interests regarding the publication of this paper.

References

[1] D. F. Feezell, J. S. Speck, S. P. Denbaars, and S. Nakamura, "Semipolar (2021) InGaN/GaN light-emitting diodes for high-efficiency solid-state lighting," *IEEE/OSA Journal of Display Technology*, vol. 9, no. 4, pp. 190–198, 2013.

[2] C.-T. Lee, U.-Z. Yang, C.-S. Lee, and P.-S. Chen, "White light emission of monolithic carbon-implanted InGaN-GaN light-emitting diodes," *IEEE Photonics Technology Letters*, vol. 18, no. 19, pp. 2029–2031, 2006.

[3] T. Egawa, B. Zhang, and H. Ishikawa, "High performance of InGaN LEDs on (111) silicon substrates grown by MOCVD," *IEEE Electron Device Letters*, vol. 26, no. 3, pp. 169–171, 2005.

[4] O. B. Shchekin, J. E. Epler, T. A. Trottier et al., "High performance thin-film flip-chip InGaN-GaN light-emitting diodes," *Applied Physics Letters*, vol. 89, no. 7, Article ID 071109, 2006.

[5] K. M. Leung, A. C. Cheung, B. C. Liu et al., "Measuring thermal conductivity of CVD diamond and diamond-like films on silicon substrates by holographic interferometry," *Diamond and Related Materials*, vol. 8, no. 8-9, pp. 1607–1610, 1999.

[6] C. M. Sung and M. C. Kan, "Cold cathode fluorescence light with amorphous diamond coated electrodes," *Nano Science and Technology Institute-Nanotech*, vol. 1, pp. 239–243, 2006.

[7] P. Y. Tsai, H. K. Huang, C.-M. Sung, M. C. Kan, and Y. H. Wang, "InGaN/GaN vertical light-emitting diodes with diamondlike carbon/titanium heat-spreading layers," *IEEE Electron Device Letters*, vol. 34, no. 8, pp. 1029–1031, 2013.

[8] R. H. Horng, K. C. Shen, C. H. Tien, S. C. Lin, and D. S. Wuu, "Performance of Cu-plating vertical LEDs in heat dissipation using diamond-like carbon," *IEEE Electron Device Letters*, vol. 35, no. 2, pp. 169–171, 2014.

Hindawi Publishing Corporation
International Journal of Photoenergy
Volume 2014, Article ID 621789, 8 pages
http://dx.doi.org/10.1155/2014/621789

Research Article

Void Shapes Controlled by Using Interruption-Free Epitaxial Lateral Overgrowth of GaN Films on Patterned SiO_2 AlN/Sapphire Template

Yu-An Chen, Cheng-Huang Kuo, Li-Chuan Chang, and Ji-Pu Wu

Institute of Lighting and Energy Photonics, National Chiao Tung University, Tainan 71150, Taiwan

Correspondence should be addressed to Cheng-Huang Kuo; kuoch@mail.nctu.edu.tw

Received 20 February 2014; Revised 26 April 2014; Accepted 2 June 2014; Published 18 June 2014

Academic Editor: Nelson Tansu

GaN epitaxial layers with embedded air voids grown on patterned SiO_2 AlN/sapphire templates were proposed. Using interruption-free epitaxial lateral overgrowth technology, we realized uninterrupted growth and controlled the shape of embedded air voids. These layers showed improved crystal quality using X-ray diffraction and measurement of etching pits density. Compared with conventional undoped-GaN film, the full width at half-maximum of the GaN (0 0 2) and (1 0 2) peaks decreased from 485 arcsec to 376 arcsec and from 600 arcsec to 322 arcsec, respectively. Transmission electron microscopy results showed that the coalesced GaN growth led to bending threading dislocation. We also proposed a growth model based on results of scanning electron microscopy.

1. Introduction

III-V compound semiconductors of AlN, GaN, and InN are suitable materials for light-emitting diodes (LEDs) because of their wurtzite crystal structures and direct band gap characteristics [1]. LEDs used for backlighting sources of liquid crystal displays demand solid-state lighting technology [2]. However, large lattice mismatches between substrates and epitaxial layers lead to the formation of threading dislocations (TDs), which decrease the lifetime of diodes and deteriorate the quality of crystals [3]. Epitaxial films with high crystal qualities are necessary for next-generation applications. Hence, reducing the TD density of epitaxial films is a primary challenge.

Recent studies have proposed several useful growth techniques to improve the crystal quality, such as epitaxial lateral overgrowth (ELOG) [4–6], pendeo-epitaxy (PE) [7], maskless PE [8], cantilever epitaxy [9], facet-controlled epitaxial lateral overgrowth (FACELO) [10, 11], SiN_x/GaN buffer layer [12], abbreviated growth mode [13–15], and freestanding GaN substrates [16–18]. Patterned sapphire substrate [19] and embedded air voids method [20, 21] have been developed to further enhance the light extraction efficiency (LEE) of light-emitting diodes (LEDs). However, embedded air voids method has been widely used. Several kinds of lateral overgrowth techniques have been reported to create air voids, such as using nanocolumns [22], nanorod [23], PE, or ELOG technique [24]. Ali et al. also showed that void shapes can be controlled using different hexagonally patterned maskless GaN templates. The TDs near the voids were bent differently with the various hexagonally patterned maskless GaN templates [25, 26]. Martinez-Criado et al. used the ELOG technique to embed air voids into GaN substrate and recommended the stress relaxation and crack suppression [16]. Dai et al. reported the higher light escaping probability with the chemical etched embedded rhombus-like air voids in light-emitting structures [27]. In addition, embedded air voids play a key role in freestanding GaN substrate fabrication. Lin et al. employed the GaN films grown on patterned sapphire substrate with large voids on the top region in the chemical lift-off process and found that the embedded voids can accelerate the wet etching process [17]. Bohyama et al. acquired spontaneously separated freestanding GaN substrate by concentrating the compressive stress at the seeds

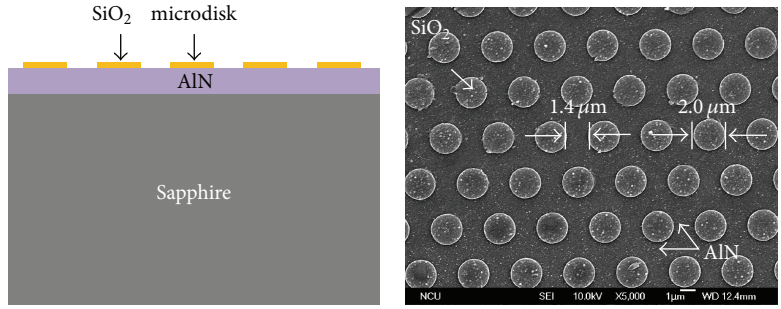

(a) (b)

Figure 1: (a) Cross-sectional structure of patterned SiO_2 AlN/sapphire template. (b) Tilted SEM image of patterned SiO_2 AlN/sapphire template.

because of the intentional formation of voids [18]. Nevertheless, the above-mentioned techniques inevitably suffer from growth interruption and complicated procedures. In ELOG technique, a 2 μm-thick GaN epitaxial layer is deposited on the substrate, followed by photolithography with dry etching and photoresist techniques to obtain the templates [4–6]. To satisfy the next-generation application, a high efficiency with a low-cost fabrication method is required. Recently, Lai et al. reported an *ex situ* AlN buffer layer deposited by sputter, which yielded an interruption-free GaN epitaxy [28]. To further improve the light extraction efficiency, Sheu et al. implanted Ar into a sputtered AlN nucleation layer, and their results showed that the GaN-based epitaxial layer grown on implanted regions has lower growth rates than the implantation-free regions, which eventually form the embedded air voids [29–31].

In this study, we introduced the interruption-free epitaxial lateral overgrowth (IFELOG) technology, a relatively efficient technique developed to simplify template fabrication while keeping the advantages of ELOG. This technology can also control void shapes using a patterned SiO_2 AlN/sapphire template and obtain an uninterrupted growth in metal-organic chemical vapor deposition (MOCVD).

2. Experimental Procedure

GaN films used in this study were all prepared by Thomas Swan ($3 \times 2''$) MOCVD. A 25 nm thick AlN buffer layer was initially deposited on a c-plane sapphire substrate by sputter. The AlN plates on the separated sputtering guns were used as the sputtering targets for AlN buffer layer deposition. An 80 nm-thick SiO_2 film was deposited on the AlN surface by plasma-enhanced chemical vapor deposition. The sample was subsequently patterned by photolithography with photoresist and dry etching processes to form patterned SiO_2 microdisks. High-density plasma was used for SiO_2 etching. Figure 1(a) shows the specification of the patterned SiO_2 AlN/sapphire template. The pitch and the diameter of the patterned SiO_2 microdisk were 3.4 and 2 μm. Figure 1(b) shows the tilted view of the scanning electron microscope (SEM) image of the patterned SiO_2 AlN/sapphire template.

In this study we controlled void shapes by IFELOG comprising three growth steps, with each step having a specific function. The first step (Step 1) involved the initial formation of GaN seeds exposed on PVD AlN buffer layer. The second step (Step 2) involved the growth performed only against the c-plane growth, and the final step (Step 3) involved the coalescence. Trimethylgallium (TMGa) and ammonia (NH_3) were, respectively, used as gallium and nitrogen sources during growth. The GaN epitaxial layer grown on a patterned SiO_2 AlN/sapphire template with rectangular, triangular, and pillar voids was labeled as sample-R, sample-T, and sample-P, respectively.

At the onset of GaN growth, the growth temperature and chamber pressure in Step 1 were set at 1050°C and 400 torr. The growth times of sample-R, sample-T, and sample-P in the same step were 1500, 750, and 1500 s, respectively. The growth temperature and chamber pressure in Step 2 were 1050°C and 100 torr. Pulsed growth technique was applied to obtain c-plane growth in this step, which is generally used to grow GaN nanorod arrays [32]. Hence, this technique enhances the c-plane growth direction. The respective pulsed growth periods of sample-R, sample-T, and sample-P were 60, 60, and 360, respectively. The flow rates of TMGa and NH_3 were 17 sccm and 3.5 slm; the injection times of TMGa and NH_3 were 3 and 5 s. Following the pulsed growth, Step 3 was performed with growth temperature and chamber pressure set at 1080°C and 400 torr. Conventional undoped-GaN with neither IFELOG technology nor patterned SiO_2 AlN/sapphire template was prepared (i.e., sample-C) for comparative purposes.

The samples were examined by optical microscopy (OM), SEM, X-ray diffraction (XRD), atomic force microscopy (AFM), and transmission electron microscopy (TEM) to discuss the distribution of IFELOG in detail.

3. Results and Discussion

Figure 2 shows the cross-sectional SEM images of GaN epitaxial layers with differently shaped air voids utilizing IFELOG on the same template. Figure 2(a) shows the cross-sectional SEM images of sample-R with embedded rectangular air voids, each having a width and height of 1.00 and

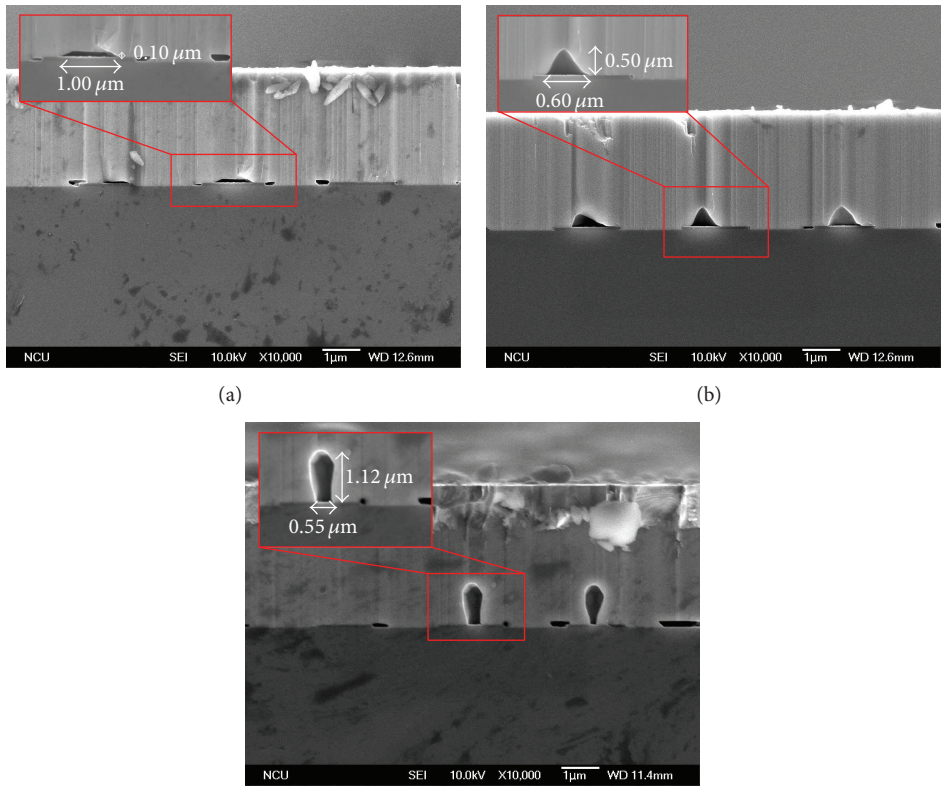

Figure 2: Cross-sectional SEM images of (a) sample-R, (b) sample-T, and (c) sample-P.

0.10 μm. Figure 2(b) shows the cross-sectional SEM images of sample-T with embedded triangular air voids, each having a width and height of 0.60 and 0.50 μm; the angle of inclination of the voids was 54°. Figure 2(c) shows the cross-sectional SEM images of sample-P with embedded pillar-shaped air voids, each having a width and height of 0.55 and 1.12 μm.

Figure 3(a) shows the growth model of the GaN epitaxial layer with various air voids. At the onset of IFELOG, we obtained different distances between GaN seeds by adjusting the growth time in Step 1 (Figures 3(a-2) and 3(b-2)). We also controlled the void heights by changing the pulsed growth periods in Step 2 (Figures 3(a-3) and 3(c-3)). Figure 4 shows the tilted and cross-sectional SEM images of the GaN epitaxial layers of sample-R after Step-2 growth in the IFELOG technology. The standing GaN seeds confirmed that this technique induced c-plane growth. We also found that the GaN seeds were not able to deposit the entire AlN area during Step-1 growth, which will be discussed in more detail in Figure 7. Considering that the samples had different growth time combinations in between steps, we obtained the various diameters and heights of GaN seeds. Ali etal. reported that the diameter of hexagonal holes between GaN affects void shape control [25]. In other words, the distances between GaN seeds define the void shape after coalescence. Figures 3(a-4), 3(b-4), and 3(c-4) show the coalesced growth in Step-3 growth. Narrowing the gap inhibits the source gas molecules from diffusing to the bottom, which eventually forms the embedded air voids that are responsible for the formation of differently shaped air voids (i.e., sample-R, sample-T, and sample-P) [33].

Table 1: Full width at half-maximum values of ω rocking curves measured by XRD.

Sample	FWHM (arcsecs)				
	(002)	(004)	(006)	(102)	(105)
Sample-C	485	479	480	600	603
Sample-R	376	362	355	322	384
Sample-T	433	454	420	408	459
Sample-P	416	420	409	360	426

The crystal quality of the GaN epitaxial layer was investigated by XRD and AFM. Heying et al. reported the pure edge TD to be insensitive to the symmetric (0 0 l) rocking curves with l nonzero and to distort only the (h k l) planes with either h or k nonzero. In other words, the decrease in the FWHM values is regarded as a reduction in TDs [34–36]. Table 1 shows the respective values of full width at half maximum (FWHM) of the GaN (0 0 2) peak, GaN (0 0 4) peak, GaN (0 0 6) peak, GaN (1 0 2) peak, and GaN (1 0 5) peak for sample-C, sample-R, sample-T, and sample-P, respectively. All of the XRD results showed an improvement in IFELOG, particularly for sample-R, which

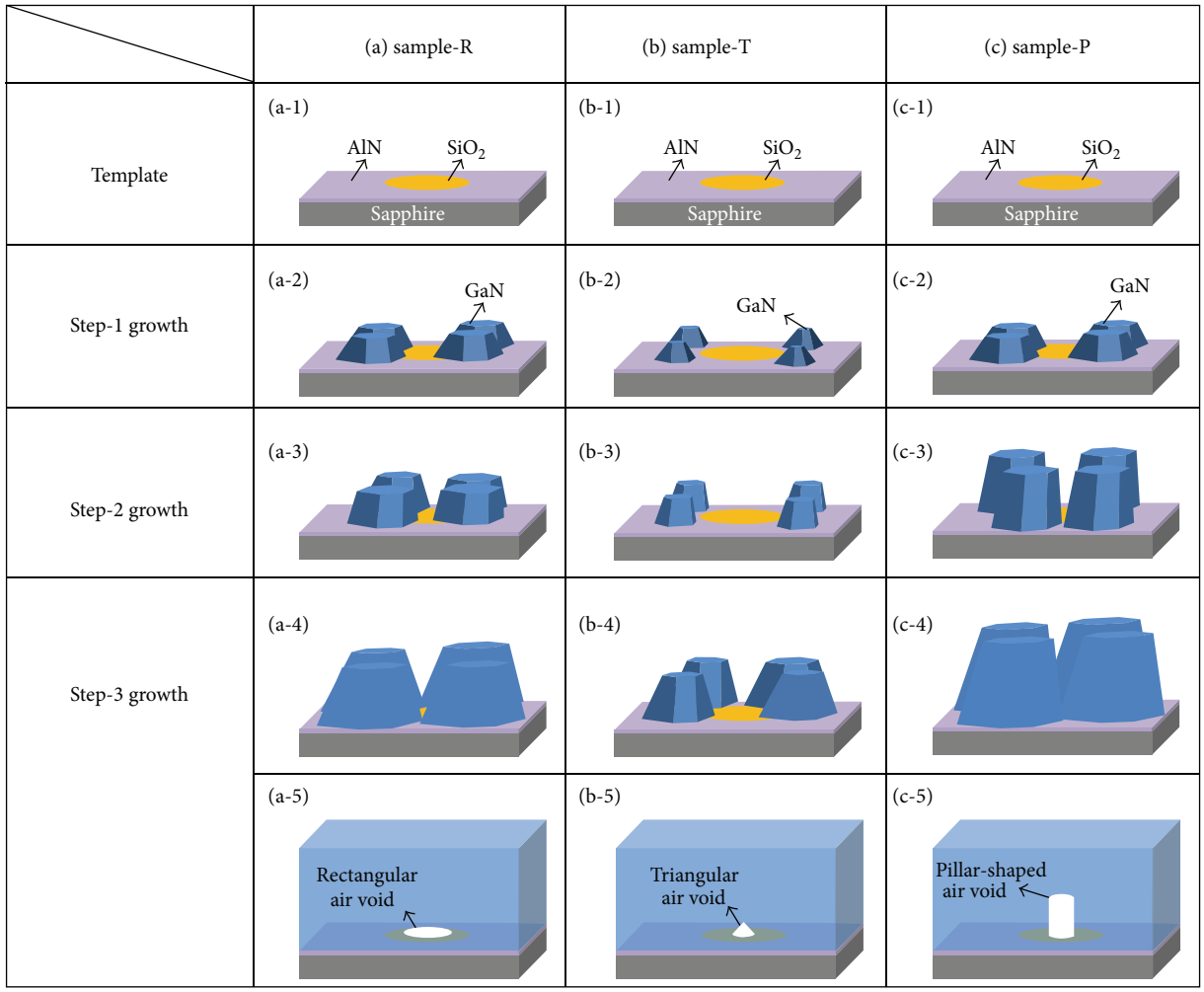

Figure 3: The proposed growth model of (a) sample-R, (b) sample-T, and (c) sample-P.

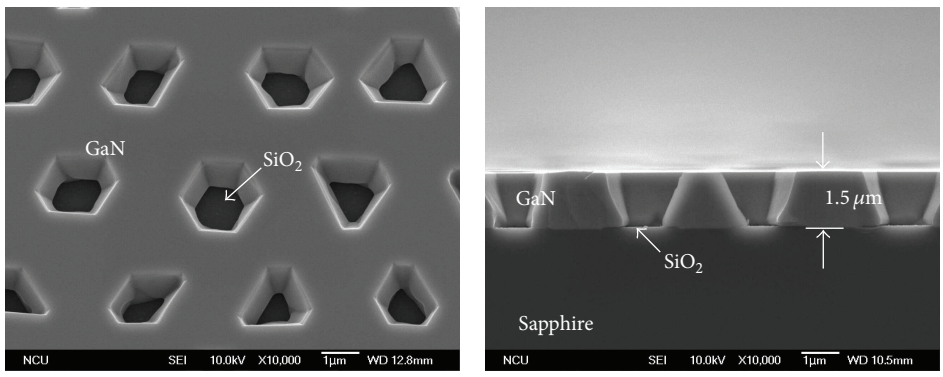

(a) (b)

Figure 4: (a) Tilted and (b) cross-sectional SEM images of the sample-R GaN epitaxial layers after Step-1 and Step-2 growth in the IFELOG technology.

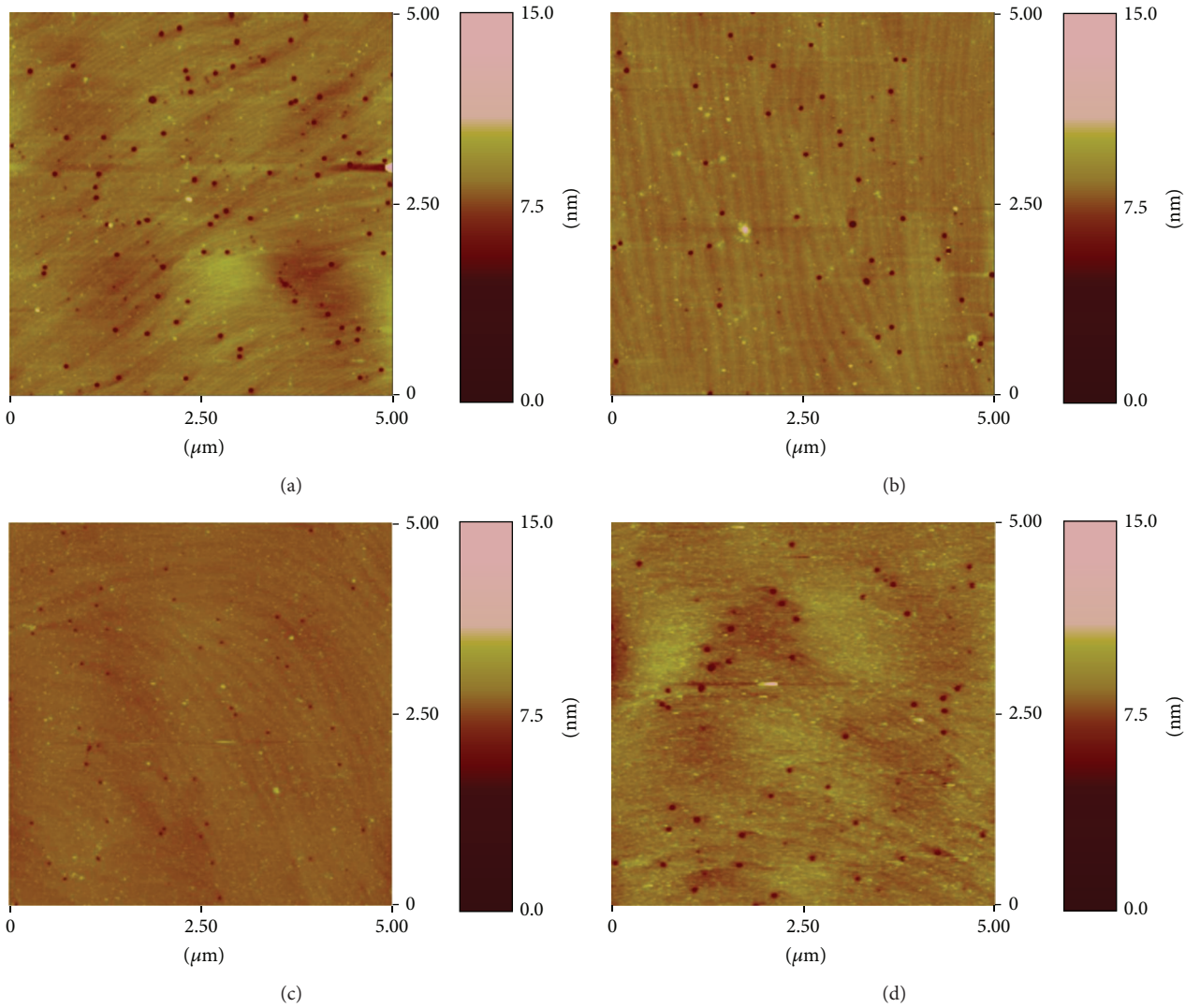

Figure 5: The EPD images over $5 \times 5\,\mu m^2$ scanning area of (a) sample-C, (b) sample-R, (c) sample-T, and (d) sample-P.

reduced the GaN (1 0 2) from 600 arcsec to 322 arcsec. XRD data showed that IFELOG significantly enhanced the crystal quality due to the lateral growth beside the embedded air voids. The bending dislocations were observed in the TEM images.

A wet etching experiment was conducted in H_3PO_4 solution at 250°C to determine the etching pit densities (EPDs) for GaN samples, and the samples were then examined using AFM. After wet etching, numerous hexagonal etching pits were observed on the surface. These etching pits were produced by the threading dislocations propagating to the surface of GaN, which originate from the interface between GaN and substrate. Figure 5 shows the EPD images over a $5 \times 5\,\mu m^2$ scanning area of sample-C, sample-R, sample-T, and sample-P. The EPDs of sample-C, sample-R, sample-T, and sample-P were 5.3×10^8, 2.4×10^8, 2.7×10^8, and $2.2 \times 10^8/cm^2$, respectively. These results indicated that the dislocation densities could be reduced in GaN epilayer using IFELOG technology, which also corresponded to the XRD result.

TEM was used to analyze the reduction in the dislocation density. Figure 6 shows the TEM images of the GaN epitaxial layer overgrown on the patterned SiO_2 AlN/sapphire template. The bended TDs were led by the coalesced growth beside the voids [26], which eventually developed into stacking faults (inset of Figure 6(c). Recent studies have reported that TDs can be blocked by SiO_2 and stacking faults mentioned above [37, 38]. Based on the TEM images, the decrease in FWHM of the GaN peak and EPDs was caused by the significant decrease in TDs of the GaN epitaxial layer through IFELOG.

Figures 7(a), 7(b), and 7(c) show the OM images of sample-R, sample-T, and sample-P, respectively. The OM images show that the patterned SiO_2 microdisk was surrounded by expanded voids. Among all the samples, sample-R and sample-T had the most and least numbers of expanded

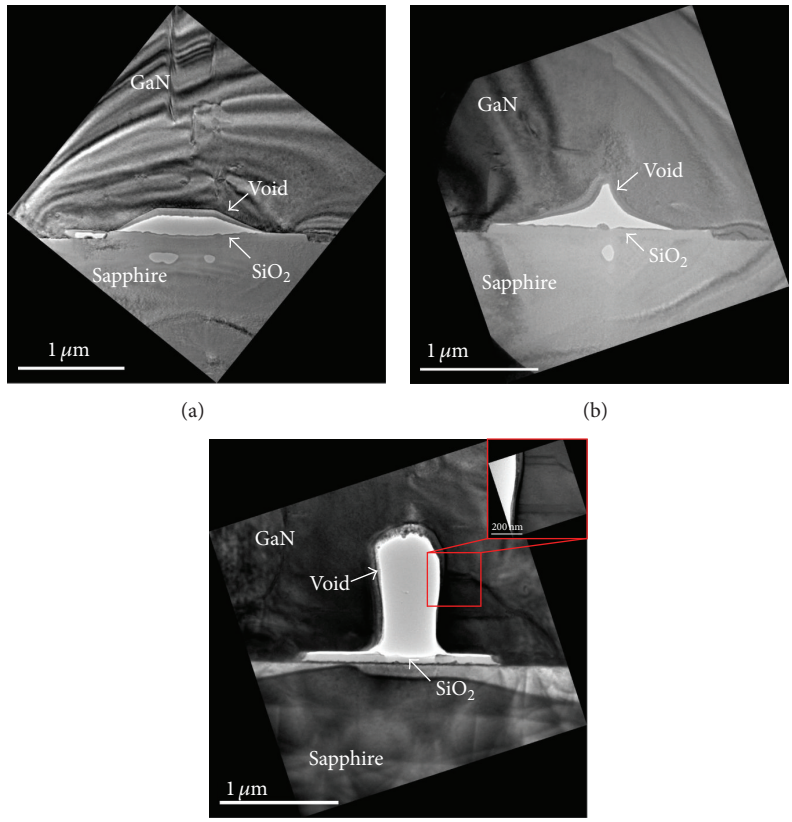

Figure 6: The TEM images of (a) sample-R, (b) sample-T, and (c) sample-P.

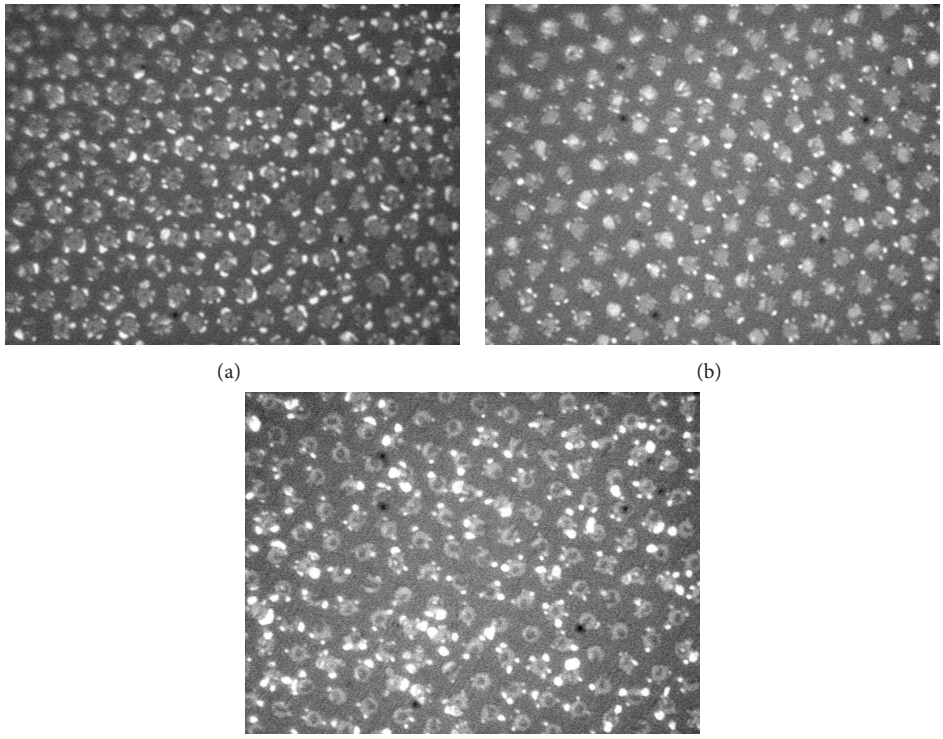

Figure 7: The OM images of (a) sample-R, (b) sample-T, and (c) sample-P.

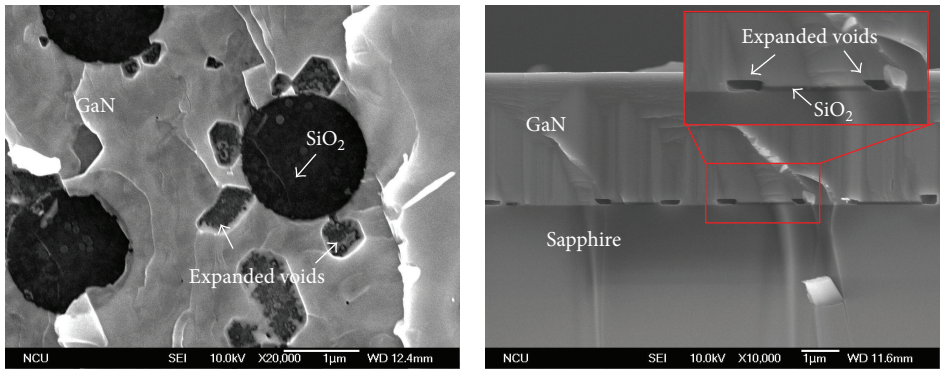

(a) (b)

Figure 8: (a) The SEM image of sample-R lifted off by diamond cutter. (b) The cross-sectional SEM image of sample-R.

voids. Lift-off template surface and cross-section SEM measurements were performed to further clarify the cause of the expanded voids that surrounded the patterned SiO_2 microdisk. Sample-R was lifted off by a diamond cutter and it was found that the expanded voids surrounded the patterned SiO_2 microdisk (Figure 8(a)). Figure 8(b) shows the cross-sectional SEM images prepared to clearly observe the interface between SiO_2 and the GaN epitaxial layer. The formation of expanded voids was caused by the discontinuous island-type growth characteristic of the GaN seed layer in the beginning. In other words, GaN seeds were not able to deposit the entire AlN area during Step-1 growth, which resulted in residual vacancies beside the patterned SiO_2 microdisk. These vacancies were converted into expanded voids, which had the similar function with the voids generated from the nanorod template [23]. Such behavior can increase the lateral growth and lower the TDs. These expanded voids were suggested to have positive effects on the quality of the GaN epitaxial layer because of the enhancement in XRD data and EPD result of sample-R, which had the most number of expanded voids.

4. Conclusion

We successfully demonstrated an interruption-free epitaxial lateral overgrowth technology by combining sputter AlN buffer layer and pulsed growth method. By adjusting Step-1 growth time and the periods of Step-2 growth, we easily controlled the void shape by the same template. The growth model was proposed to explain the formation of differently shaped air voids based on the SEM results. AFM images show that the epitaxial layer grown by IFELOG technology has lower etching pit densities, thereby increasing the volume of defect-free regions and bending TDs. XRD data suggests that we can decrease the FWHM of the GaN (0 0 2) and (1 0 2) peaks from 485 arcsec to 376 arcsec and from 600 arcsec to 322 arcsec in sample-R. IFELOG technology not only simplified the fabrication of templates, but also greatly enhanced the quality of the GaN epitaxial layer and yielded an uninterrupted growth.

Conflict of Interests

The authors declare that there is no conflict of interests regarding the publication of this paper.

Acknowledgment

The authors would like to acknowledge the financial support from National Science Council of Taiwan for their research Grants of NSC 101-2221-E-009-028-MY3 and NSC-3113-P-009-007-CC2.

References

[1] T. Mukai, M. Yamada, and S. Nakamura, "Characteristics of InGaN-based UV/blue/green/amber/red light-emitting diodes," *Japanese Journal of Applied Physics, Part 1: Regular Papers and Short Notes and Review Papers*, vol. 38, no. 7, pp. 3976–3981, 1999.

[2] Y. Narukawa, I. Niki, K. Izuno, M. Yamada, Y. Murazaki, and T. Mukai, "Phosphor-conversion white light emitting diode using InGaN near-ultraviolet chip," *Japanese Journal of Applied Physics, Part 2: Letters*, vol. 41, no. 4, pp. L371–L373, 2002.

[3] Y. P. Hsu, S. J. Chang, Y. K. Su et al., "Lateral epitaxial patterned sapphire InGaN/GaN MQW LEDs," *Journal of Crystal Growth*, vol. 261, no. 4, pp. 466–470, 2004.

[4] D. Kapolnek, S. Keller, R. Vetury et al., "Anisotropic epitaxial lateral growth in GaN selective area epitaxy," *Applied Physics Letters*, vol. 71, no. 9, pp. 1204–1206, 1997.

[5] T. S. Zheleva, O.-H. Nam, M. D. Bremser, and R. F. Davis, "Dislocation density reduction via lateral epitaxy in selectively grown GaN structures," *Applied Physics Letters*, vol. 71, no. 17, pp. 2472–2474, 1997.

[6] M. Hansen, P. Fini, M. Craven, B. Heying, J. S. Speck, and S. P. DenBaars, "Morphological and optical properties of InGaN laser diodes on laterally overgrown GaN," *Journal of Crystal Growth*, vol. 234, no. 4, pp. 623–630, 2002.

[7] I.-H. Kim, C. Sone, O.-H. Nam, Y.-J. Park, and T. Kim, "Crystal tilting in GaN grown by pendoepitaxy method on sapphire substrate," *Applied Physics Letters*, vol. 75, no. 26, pp. 4109–4111, 1999.

[8] A. M. Roskowski, E. A. Preble, S. Einfeldt, P. M. Miraglia, and R. F. Davis, "Investigations regarding the maskless Pendeo-epitaxial growth of GaN films prior to coalescence," *IEEE Journal of Quantum Electronics*, vol. 38, no. 8, pp. 1006–1016, 2002.

[9] C. I. H. Ashby, C. C. Mitchell, J. Han et al., "Low-dislocation-density GaN from a single growth on a textured substrate," *Applied Physics Letters*, vol. 77, no. 20, pp. 3233–3235, 2000.

[10] H. Miyake, R. Takeuchi, K. Hiramatsu et al., "High quality GaN grown by facet-controlled ELO, (FACELO) technique," *Physica Status Solidi (A)*, vol. 194, pp. 545–549, 2002.

[11] K. Hiramatsu, K. Nishiyama, M. Onishi et al., "Fabrication and characterization of low defect density GaN using facet-controlled epitaxial lateral overgrowth (FACELO)," *Journal of Crystal Growth*, vol. 221, no. 1–4, pp. 316–326, 2000.

[12] Y.-B. Lee, T. Wang, Y.-H. Liu et al., "High-performance 348 nm AlGaN/GaN-based ultraviolet-light-emitting diode with a SiN buffer layer," *Japanese Journal of Applied Physics, Part 1: Regular Papers and Short Notes and Review Papers*, vol. 41, no. 7, pp. 4450–4453, 2002.

[13] Y.-K. Ee, J. M. Biser, W. Cao, H. M. Chan, R. P. Vinci, and N. Tansu, "Metalorganic vapor phase epitaxy of III-nitride light-emitting diodes on nanopatterned AGOG sapphire substrate by abbreviated growth mode," *IEEE Journal on Selected Topics in Quantum Electronics*, vol. 15, no. 4, pp. 1066–1072, 2009.

[14] Y.-K. Ee, X.-H. Li, J. Biser et al., "Abbreviated MOVPE nucleation of III-nitride light-emitting diodes on nano-patterned sapphire," *Journal of Crystal Growth*, vol. 312, no. 8, pp. 1311–1315, 2010.

[15] W. Cao, J. M. Biser, Y.-K. Ee et al., "Dislocation structure of GaN films grown on planar and nano-patterned sapphire," *Journal of Applied Physics*, vol. 110, no. 5, Article ID 053505, 2011.

[16] G. Martinez-Criado, M. Kuball, M. Benyoucef et al., "Free-standing GaN grown on epitaxial lateral overgrown GaN substrates," *Journal of Crystal Growth*, vol. 255, no. 3-4, pp. 277–281, 2003.

[17] C.-F. Lin, J.-J. Dai, M.-S. Lin et al., "An AlN sacrificial buffer layer inserted into the GaN/patterned sapphire substrate for a chemical lift-off process," *Applied Physics Express*, vol. 3, no. 3, Article ID 031001, 2010.

[18] S. Bohyama, H. Miyake, K. Hiramatsu, Y. Tsuchida, and T. Maeda, "Freestanding GaN substrate by advanced facet-controlled epitaxial lateral overgrowth technique with masking side facets," *Japanese Journal of Applied Physics, Part 2: Letters*, vol. 44, no. 1–7, pp. L24–L26, 2005.

[19] W.-K. Wang, D.-S. Wuu, W.-C. Shih et al., "Near-ultraviolet InGaN/GaN light-emitting diodes grown on patterned sapphire substrates," *Japanese Journal of Applied Physics, Part 1: Regular Papers and Short Notes and Review Papers*, vol. 44, no. 4, pp. 2512–2515, 2005.

[20] W.-C. Lai, Y.-Y. Yang, L.-C. Peng, S.-W. Yang, Y.-R. Lin, and J.-K. Sheu, "GaN-based light emitting diodes with embedded SiO_2 pillars and air gap array structures," *Applied Physics Letters*, vol. 97, no. 8, Article ID 081103, 2010.

[21] M. Ali, O. Svensk, L. Riuttanen et al., "Enhancement of near-UV GaN LED light extraction efficiency by GaN/sapphire template patterning," *Semiconductor Science and Technology*, vol. 27, no. 8, Article ID 082002, 2012.

[22] S. D. Hersee, X. Y. Sun, X. Wang, M. N. Fairchild, J. Liang, and J. Xu, "Nanoheteroepitaxial growth of GaN on Si nanopillar arrays," *Journal of Applied Physics*, vol. 97, no. 12, Article ID 124308, 2005.

[23] C. H. Kuo, Y. A. Chen, J. P. Wu, and L. C. Chang, "Efficiency improvement of near-ultraviolet nitride-based light-emitting-diode prepared on GaN nano-rod arrays by metalorganic chemical vapor deposition," *IEEE Journal of Quantum Electronics*, vol. 50, no. 3, article 129, 2014.

[24] Z. Liliental-Weber, X. Ni, and H. Morkoc, "Structural perfection of laterally overgrown GaN layers grown in polar- and non-polar directions," *Journal of Materials Science: Materials in Electronics*, vol. 19, no. 8-9, pp. 815–820, 2008.

[25] M. Ali, A. E. Romanov, S. Suihkonen et al., "Void shape control in GaN re-grown on hexagonally patterned mask-less GaN," *Journal of Crystal Growth*, vol. 315, no. 1, pp. 188–191, 2011.

[26] M. Ali, A. E. Romanov, S. Suihkonen et al., "Analysis of threading dislocations in void shape controlled GaN re-grown on hexagonally patterned mask-less GaN," *Journal of Crystal Growth*, vol. 344, no. 1, pp. 59–64, 2012.

[27] J.-J. Dai, C.-F. Lin, G.-M. Wang, and M.-S. Lin, "Enhanced the light extraction efficiency of an InGaN light emitting diodes with an embedded rhombus-like air-void structure," *Applied Physics Express*, vol. 3, no. 7, Article ID 071002, 2010.

[28] C.-H. Yen, W.-C. Lai, Y.-Y. Yang et al., "GaN-based light-emitting diode with sputtered AlN nucleation layer," *IEEE Photonics Technology Letters*, vol. 24, no. 4, pp. 294–296, 2012.

[29] Y. H. Yeh, J. K. Sheu et al., "InGaN flip-chip light emitting diodes with embedded air voids as light-scattering layer," *IEEE Electron Device Letters*, vol. 34, no. 12, pp. 1542–1544, 2013.

[30] J.-K. Sheu, Y.-H. Yeh, S.-J. Tu, M.-L. Lee, P. C. Chen, and W.-C. Lai, "Improved output power of GaN-based blue LEDs by forming air voids on Ar-implanted sapphire substrate," *Journal of Lightwave Technology*, vol. 31, no. 8, Article ID 6464504, pp. 1318–1322, 2013.

[31] J.-K. Sheu, S.-J. Tu, Y.-H. Yeh, M.-L. Lee, and W.-C. Lai, "Gallium nitride-based light-emitting diodes with embedded air voids grown on Ar-implanted AlN/sapphire substrate," *Applied Physics Letters*, vol. 101, no. 15, Article ID 151103, 2012.

[32] S. D. Hersee, X. Sun, and X. Wang, "The controlled growth of GaN nanowires," *Nano Letters*, vol. 6, no. 8, pp. 1808–1811, 2006.

[33] H. J. Oh, S. W. Rhee, and I. S. Kang, "Simulation of CVD process by boundary integral technique," *Journal of the Electrochemical Society*, vol. 139, no. 6, pp. 1714–1720, 1992.

[34] H. Heinke, V. Kirchner, S. Einfeldt, and D. Hommel, "X-ray diffraction analysis of the defect structure in epitaxial GaN," *Applied Physics Letters*, vol. 77, no. 14, pp. 2145–2147, 2000.

[35] Y. Iyechika, M. Shimizu, T. Maeda, H. Miyake, and K. Hiramatsu, "X-ray analysis of twist and tilt of GaN prepared by facet-controlled epitaxial lateral overgrowth (FACELO)," *Japanese Journal of Applied Physics, Part 2: Letters*, vol. 42, no. 7, pp. L732–L734, 2003.

[36] B. Heying, X. H. Wu, S. Keller et al., "Role of threading dislocation structure on the x-ray diffraction peak widths in epitaxial GaN films," *Applied Physics Letters*, vol. 68, article 643, 1995.

[37] C. H. Chiu, H. H. Yen, C. L. Chao et al., "Nanoscale epitaxial lateral overgrowth of GaN-based light-emitting diodes on a SiO_2 nanorod-array patterned sapphire template," *Applied Physics Letters*, vol. 93, no. 8, Article ID 081108, 2008.

[38] D. S. Wuu, W. K. Wang, K. S. Wen et al., "Fabrication of pyramidal patterned sapphire substrates for high-efficiency InGaN-based light emitting diodes," *Journal of the Electrochemical Society*, vol. 153, no. 8, Article ID 063608JES, pp. G765–G770, 2006.

Hindawi Publishing Corporation
International Journal of Photoenergy
Volume 2014, Article ID 407239, 6 pages
http://dx.doi.org/10.1155/2014/407239

Research Article

Color Rendering Index Thermal Stability Improvement of Glass-Based Phosphor-Converted White Light-Emitting Diodes for Solid-State Lighting

Chun-Chin Tsai

Department of Optoelectronic Engineering, Far East University, Tainan 744, Taiwan

Correspondence should be addressed to Chun-Chin Tsai; tsaichunchin@gmail.com

Received 29 January 2014; Revised 18 March 2014; Accepted 1 April 2014; Published 5 June 2014

Academic Editor: Ray-Hua Horng

High color rendering index performance has been required for phosphor-converted warm-white light-emitting diodes (PC-WWLEDs) in lighting industry. The characteristics of low-temperature fabricated phosphor (yellow: Ce^{3+}:YAG, green: Tb^{3+}:YAG, and red: $CaAlClSiN_3$:Eu^{2+}) doped glass were presented for applications to high color rendering index warm-white-light-emitting diodes. Color coordinates (x, y) = (0.36, 0.29), quantum yield (QY) = 55.6%, color rending index (CRI) = 85.3, and correlated color temperature (CCT) = 3923 K were characterized. Glass-based PC-WWLEDs was found able to maintain good thermal stability for long-time high-temperature operation. QY decay, CRI remenance, and chromaticity shift were also analyzed for glass- and silicone-based high-power PC-WLEDs by thermal aging at 150°C and 250°C for industrial test standard's aging time 1008 hours. Better than the silicone's, thermal stability of glass-based PC-WLEDs has been improved. The resulted high color rendering index (CRI) glass phosphor potentially can be used as a phosphor layer for high-performance and low-cost PC-WLEDs used in next-generation indoor solid-state lighting applications.

1. Introduction

For liquid crystal displays and outdoor lightings, white light-emitting diodes (WLEDs) have been extensively used as backlight source due to their eco-friendly features, compact size, and high reliability compared to conventional light sources, such as incandescent bulbs and fluorescent lamps [1–4]. The so-called "white light" emission can be typically generated by the mixture of three primary colors (red, green, and blue) or two complimentary colors (e.g., blue and yellow), based on the principle of additive color mixing [5–7]. Subjected to the physical structure of WLED modules, the strategy of realizing white light can be categorized into two major technologies: (1) combination of multiple LEDs and (2) phosphor-converted LEDs (PC-LEDs). In the first strategy of white light emission, two or three monochromatic LEDs are used to generate preferred white light. Dynamic color control is achievable by electronically adjusting the driving current of each LED individually. Its high quantum efficiency is also an advantage of the multiple LEDs technique without Stokes shift which is due to photonic energy downconversion [8, 9]. However, cost of multiple LEDs technique is much higher than other techniques, so multiple LEDs technique is only used in some special applications. Therefore, PC-LEDs technology dominates the market today because of significantly low cost, compact structure, and simple driving circuit, although the quantum efficiency of PC-LEDs is slightly lower than that of multiple LEDs. PC-LEDs are in a configuration with a short-wavelength-emitting LED as the excitation sources in the visible [10, 11] and/or UV [12, 13] spectral regimes, and a wavelength converter such as phosphor, which converts the light from excitation sources to generate white light. The correlated color temperature and color rendering property of the PC-LEDs can be determined upon the composition and concentration of the phosphor in the wavelength converters. Full development of phosphor materials significantly contributed to LED lightings. Yellow phosphors, such as broadband YAG phosphors, have been extensively studied on the integration with the complementary blue LEDs to form white light. However, color rendering

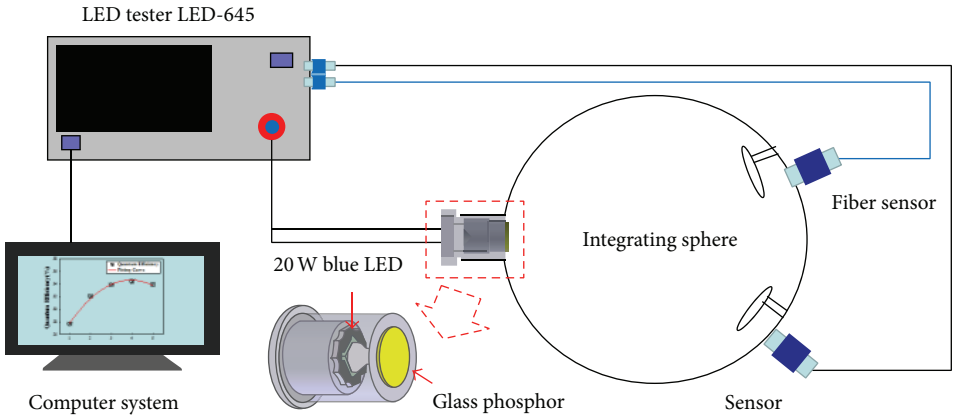

Figure 1: The test chamber schematic for optical measurement.

index (CRI) of the WLEDs is usually less than 70, which is not acceptable for general interior illumination and some special lighting including medical applications and architectural lighting. To achieve high color rendering properties, multiphosphors such as red/yellow and orange/yellow have to be added into the color conversion layer. Multiphosphor-doped silicone as the color conversion layer of the high-CRI WLED has been fabricated to demonstrate the above purpose [14, 15], but the poor thermal stability of the silicone matrix weakens the superiority for high-luminance lighting applications, due to the lower glass transition temperature of silicone (150°C). In the previous works for yellow light emission to mix with blue light from LED, we have demonstrated novel glass-based phosphors with excellent thermal stability for the applications of high-power WLEDs [16], but the resulted CRI values were normally as low as 70s with single phosphor powder.

Remote phosphor was studied as an alternative technology for white light LED. Kuo et al. investigated patterned structure of remote phosphor for phosphor-converted white light LEDs [17]. This patterned structure was designed to reduce the angular-dependent correlated color temperature (CCT). Intematix Company reported polycarbonate-based remote phosphor layer around source LED [18], though glass-based remote phosphor product could be under development.

In this study, we fabricated a thermally stable multiphosphor-doped glass (MPDG) for the goal. The results showed that the glass-based PC-WLEDs exhibited good thermal stability in lumen loss, chromaticity shift, CRI, and QE characteristics. Then we compared with the silicone-based high-power PC-WLEDs under thermal aging at lower temperature of 150°C, 250°C, 350°C, and 450°C. The results demonstrated that the thermal stability of glass-based PC-WLEDs outperformed the silicone-based PC-WLEDs. The novel development of glass-based PC-WLEDs is essentially critical to the application of LED modules in the area where absolute reliability is required and where silicone simply cannot stand the heat, humidity, or other deteriorating factors due to its low thermal stability. The multiphosphors layer of glass as an encapsulating material may be advanced for many applications where the LED modules with high reliability are required.

2. Experiment and Measurement

The glass matrix was composed of SiO_2, Na_2CO_3, Al_2O_3, and CaO to be mixed and then melt at 1300°C for 1 hour in a platinum crucible. The cooled cullet glass (SiO_2-Na_2O-Al_2O_3-CaO) was milled into powders and kept dried. Yellow ($Y_3Al_5O_{12}:Ce^{3+}$, YAG based), green ($Lu_3Al_5O_{12}:Ce^{3+}$, LuAG based), and red ($CaAlSiN_3:Eu^{2+}$, nitride based) phosphors of different ratio were uniformly mixed into the matrix glass powder followed by melting at 680°C for 6 hours, labeled as $Y_1G_0R_0DG$, $Y_1G_1R_1DG$, $Y_2G_1R_1DG$, $Y_1G_2R_1DG$, and $Y_1G_1R_2DG$ according to the composition ratio among yellow/green/red phosphor in the glass phosphors. These glass phosphor samples were then polished to 0.5 mm of thickness after quenching down to room temperature. With 15 mm in diameter and 0.5 mm thick, the solidified glass phosphor circular disks were entirely covered over the LED and the reflective cup to form a WLED module. An integrating sphere equipped with an optical fiber and a CCD detector was employed to measure the optical spectra of the WLED module.

For thermal aging tests (its setup as shown in Figure 1), eleven phosphor disk samples from low-temperature glass CeYDG were aging at 150°C, 250°C, 350°C, and 450°C for 1008 hours. All the samples of MPDG ($Y_1G_1R_1DG$) with diameter, thickness, and chromaticity coordinates were 15 mm (±0.25), 0.5 mm (±0.025), and (0.36 ± 0.005, 0.29 ± 0.005), as shown in Table 1.

Thermal aging tests were measured periodically in order to characterize the degradation of phosphor materials on lumen, CIE, and CRI. The data of all samples were obtained through the LED-645 test system (Lightports). The quantum yield (QY) is one of the major parameters used as a selected

Table 1: High CRI sample counts of accelerated test.

Aging temperature (°C)	150	250	350	450
Sample quantity (pcs.)	11	11	11	11
Chromaticity coordinates	(0.35, 0.28)	(0.35, 0.28)	(0.35, 0.28)	(0.35, 0.28)
Diameter (mm)	15	15	15	15
Thickness (mm)	0.5	0.5	0.5	0.5

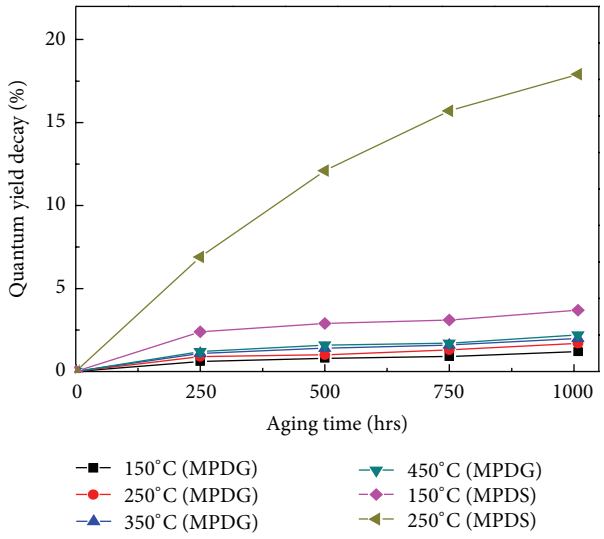

Figure 2: Quantum yield decay (%) versus aging time for PC-WLEDs of MPDG and MPDS samples at different temperatures.

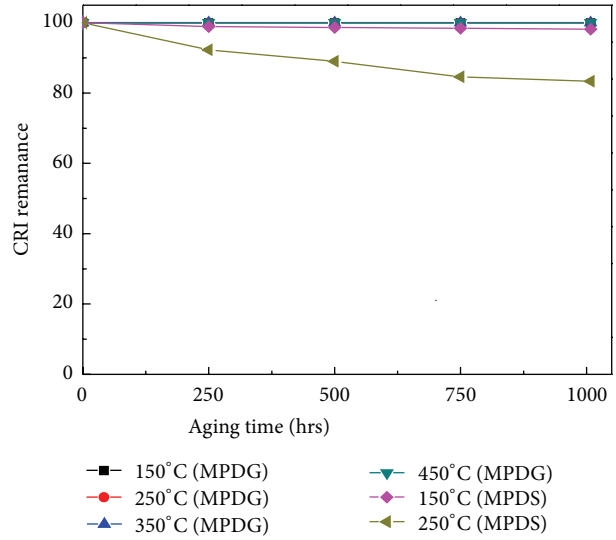

Figure 3: The CRI remanence versus aging time for PC-WLEDs of MPDG and MPDS samples at different temperatures.

criterion of luminescence materials in solid-state lighting applications, as shown in the following:

$$\mathrm{QY} = \frac{N_{\mathrm{erm}}}{N_{\mathrm{Abs}}}, \tag{1}$$

where the QY of the wavelength converting materials is defined as the ratio of the number of photons emitted (N_{erm}) to the number of photons absorbed from the emission of the pumping light sources (N_{Abs}), where the number of photons in each wavelength, $N(\lambda)$ (cps/nm), can be obtained through dividing spectrum distribution $P(\lambda)$ (mW/nm) by photon energy $h\nu$ (J) [19].

CRI remanence is defined as the measured value of CRI after thermal degradation.

The chromaticity shift is defined as

$$\Delta E = \sqrt{\left(u'_f - u'_i\right)^2 + \left(v'_f - v'_i\right)^2 + \left(w'_f - w'_i\right)^2}, \tag{2}$$

where $u' = 4x/(3 - 2x + 12y)$, $v' = 9y/(3 - 2x + 12y)$ and $w' = 1 - u' - v'$. The u' and v' are the uniform chromaticity coordinates [20], the x and y are the chromaticity coordinates (CIE 1931), and the i and f are the chromaticity shift before and after test, respectively. A schematic diagram of the test chamber for optical measurements is shown in Figure 2. The test chamber consisted of a 5 W GaN blue-light LED, a heat sink, a removable phosphor layer, and an integral sphere. LED and phosphor layer were integrated together. This setup is to ensure the thermal aging effect on phosphor layer after thermal aging tests that can be obtained precisely. Lumen degradation, chromaticity shift, and CRI loss at the wavelength of 460 nm were recorded and compared before and after each thermal test.

3. Results and Discussion

Table 2 shows optical properties of the WLEDs utilizing MPDG. The color coordinates and color temperature of the WLED utilizing Y1G1R1DG are (0.358, 0.288; 3923 K) with high color rendering index up to 85 suitable for interior lighting.

3.1. Thermal Stability of High CRI Glass Phosphors. The thermal stability test results of both types of samples were carried out at 150°C, 250°C, 350°C, and 450°C for 1008 hours. Due to silicone material carbonized above 280°C, MPDS samples can merely be characterized under this temperature. Thus, MPDS can only be compared with MPDG below such critical temperature, while the characteristics of MPDG will be still presented at 350°C and 450°C.

3.1.1. Quantum Yield Decay. To investigate the reliability of the high CRI phosphor with the glass and silicone, QY decay was measured as a function of aging time after thermal aging

Table 2: Optical properties of MPDG based WLED.

MPDG type	Top view	CIE (x, y)	CCT (K)	CRI	QY (%)
$Y_1G_0R_0DG$		(0.321, 0.325)	6043	68.58	68.36
$Y_1G_1R_1DG$		(0.358, 0.288)	3923	85.25	55.57
$Y_2G_1R_1DG$		(0.405, 0.363)	3248	73.96	59.40
$Y_1G_2R_1DG$		(0.375, 0.334)	3803	81.25	55.31
$Y_1G_1R_2DG$		(0.428, 0.302)	2182	70.16	47.24

Table 3: Characteristics of MPDG and MPDS based WLED samples accelerated thermal aging after 1008 hours.

Characteristics	Phosphor layer type	150°C	250°C	350°C	450°C
QY decay (%)	MPDG	1.2	1.7	2	2.2
	MPDS	3.7	17.9	N.A.	N.A.
CRI remanence	MPDG	100	100	100	100
	MPDS	98.2	83.4	N.A.	N.A.
CIE shift (10^{-3})	MPDG	3.5	4.2	4.6	5.5
	MPDS	10.1	151.8	N.A.	N.A.

at 150 and 250°C for MPDG and MPDS shown in Figure 2, at measurement period 250 hours. After 1080-hour aging, the QY losses of MPDG were 1.2%, 1.7%, 2%, and 2.2% at 150°C, 250°C, 350°C and 450°C, respectively. The QY losses of MPDS were 3.7 and 17.9 times higher than MPDG at 150°C and 250°C, respectively. MPDG samples maintained good thermal stability in QY characteristic.

3.1.2. Color Rendering Index Remanence. CRI remanence was measured as a function of aging time of the MPDG and MPDS after thermal aging at 150°C, 250°C, 350°C, and 450°C at measurement period 250 hours shown in Figure 3. After 250-hour aging, the CRI remanence of MPDS was 98.2% and 83.4% at 150°C and 250°C, respectively, while CRI attenuation was almost undetectable in the case of MPDG, indicating that

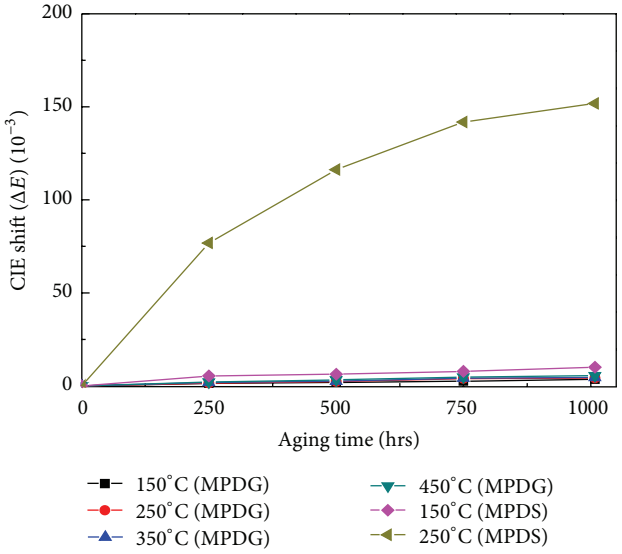

Figure 4: Chromaticity shift versus aging time for PC-WLEDs of MPDG and MPDS samples at different temperatures.

the MPDG samples maintained good thermal stability in CRI characteristic.

3.1.3. Chromaticity Shift. The chromaticity shift was measured as a function of aging time of the MPDG and MPDS after thermal aging at 150°C, 250°C, 350°C, and 450°C as shown in Figure 4 for period of 1080 hours. The chromaticity shifts of MPDG were 3.2, 4.2, 4.6, and 5.5 all in the order of 10^{-3} at 150°C, 250°C, 350°C, and 450°C, respectively. After 1008 hrs aging test, the chromaticity shifts of MPDS were 10.1×10^{-3} and 151.8×10^{-3} at 150°C and 250°C, respectively. The chromaticity of MPDG samples was thermally stable than MPDS's.

3.1.4. Emission Spectrum. The emission spectrum was measured, with integrating sphere spectrometer, as a function of aging time for the MPDG and MPDS after thermal aged at 150°C, 250°C, 350°C, and 450°C, (a) and (b), respectively, shown in Figure 5. After industrial test standard 1008-hour aging, better than MPDS's, all 4 samples of MPDG did not have significant intensity decay, as 2% and 3% at 150°C and 250°C, respectively, less than 7% and 35% of MPDS, respectively. This indicates that the MPDG sample maintained good thermal stability regarding spectrum.

In Table 3, for both MPDG and MPDS, the accelerated thermal aging test results of QY loss, CRI remanence, and CIE shift were summarized as regarding aging temperature at 150°C, 250°C, 350°C, and 450°C. Due to a higher T_g of glass matrix, it is also expected that internal strain is less in glass materials than in silicone under similar thermal stress owing to glass's lower thermal expansion coefficient. Since silicone matrix material tends to be carbonized by higher temperature aging [18], its thermal induced optical characteristic deterioration, such as CRI dropping, and so forth, will be prominent. These results showed that MPDG

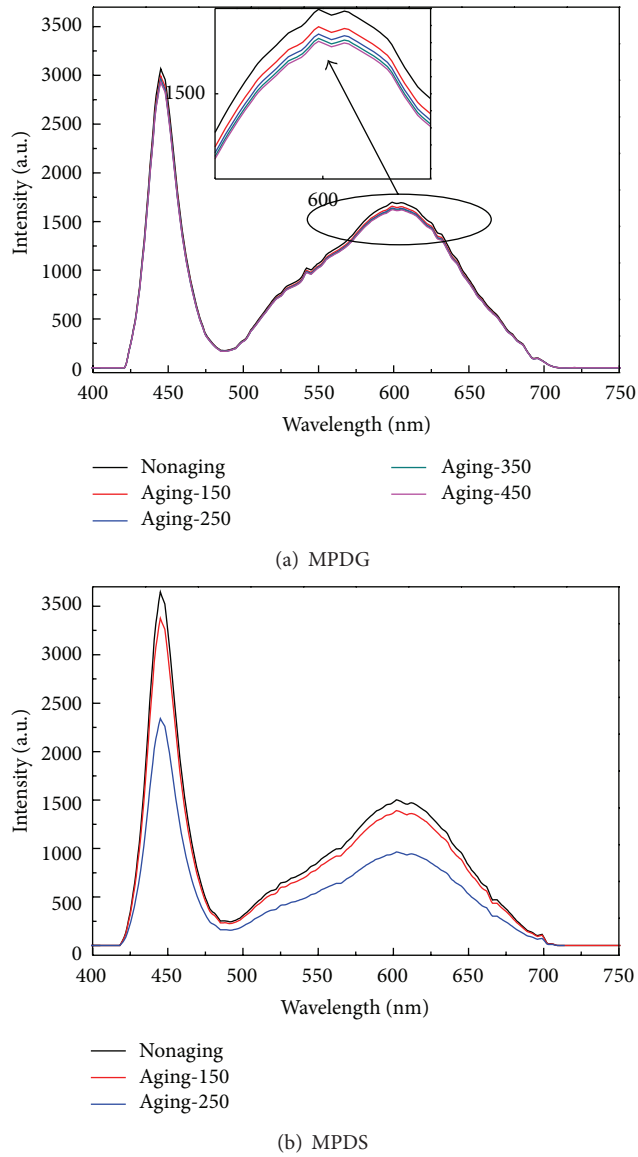

Figure 5: Emission spectrum versus aging time for PC-WLEDs of MPDG and MPDS samples at different temperatures.

phosphor conversion layer is effective for long-time high-temperature operation, and high CRI potentially for use in highly efficient and high output power LEDs.

4. Conclusion

The highly thermal stable phosphor-doped glass material has been successfully developed with both higher CRI and QY than those made of silicone. CRI remanence and CIE shift in glass-based high-power PC-WLEDs outperformed silicone base under thermal aging at 150, 250, 350, and 450°C for industrial test standard 1008 hours. The results showed that the glass-based PC-WLEDs held better thermal stability in QY decay, CRI remanence, and chromaticity shift than the silicone-based PC-WLED, due to higher glass transition temperature (T_g) of glass material property. More thermally

stable phosphor layer of glass encapsulation material may be beneficial for many applications where LED modules with high power and high reliability are demanded for the next-generation solid-state lighting industry.

Conflict of Interests

The author declares that there is no conflict of interests regarding the publication of this paper.

Acknowledgments

This work was supported by the Science Park Administration under the Grant 102A10, the National Science Council under the Grants NSC 101-2218-E-269-001, NSC 101-2622-E-269-020-CC2, and NSC 101-3113-E-110-002-CC2, and the Advanced Optoelectronic Technology Center, National Cheng Kung University, Taiwan.

References

[1] D. A. Steigerwald, J. C. Bhat, D. Collins et al., "Illumination with solid state lighting technology," *IEEE Journal on Selected Topics in Quantum Electronics*, vol. 8, no. 2, pp. 310–320, 2002.

[2] J. K. Kim and E. F. Schubert, "Transcending the replacement paradigm of a solid-state lighting," *Optics Express*, vol. 16, no. 26, pp. 21835–21842, 2008.

[3] M. R. Krames, O. B. Shchekin, R. Mueller-Mach et al., "Status and future of high-power light-emitting diodes for solid-state lighting," *IEEE/OSA Journal of Display Technology*, vol. 3, no. 2, pp. 160–175, 2007.

[4] S.-R. Lim, D. Kang, O. A. Ogunseitan, and J. M. Schoenung, "Potential environmental impacts from the metals in incandescent, compact fluorescent lamp (CFL), and light-emitting diode (LED) bulbs," *Environmental Science and Technology*, vol. 47, no. 2, pp. 1040–1047, 2013.

[5] J. K. Sheu, S. J. Chang, C. H. Kuo et al., "White-light emission from near UV InGaN-GaN LED chip precoated with blue/green/red phosphors," *IEEE Photonics Technology Letters*, vol. 15, no. 1, pp. 18–20, 2003.

[6] S. Muthu, F. J. P. Schuurmans, and M. D. Pashley, "Red, green, and blue LEDs for white light illumination," *IEEE Journal on Selected Topics in Quantum Electronics*, vol. 8, no. 2, pp. 333–338, 2002.

[7] K. S. Ramaiah, Y. K. Su, S. J. Chang, and C. H. Chen, "A comparative study of blue, green and yellow light emitting diode structures grown by metal organic chemical vapor deposition," *Solid-State Electronics*, vol. 50, no. 2, pp. 119–124, 2006.

[8] J. P. You, N. T. Tran, and F. G. Shi, "Light extraction enhanced white light-emitting diodes with multi-layered phosphor configuration," *Optics Express*, vol. 18, no. 5, pp. 5055–5060, 2010.

[9] R. Mueller-Mach, G. O. Mueller, M. R. Krames, and T. Trottier, "High-power phosphor-converted light-emitting diodes based on III-nitrides," *IEEE Journal on Selected Topics in Quantum Electronics*, vol. 8, no. 2, pp. 339–345, 2002.

[10] J. Zhang and N. Tansu, "Improvement in spontaneous emission rates for InGaN quantum wells on ternary InGaN substrate for light-emitting diodes," *Journal of Applied Physics*, vol. 110, no. 11, Article ID 113110, 2011.

[11] H. Zhao, G. Liu, J. Zhang, J. D. Poplawsky, V. Dierolf, and N. Tansu, "Approaches for high internal quantum efficiency green InGaN light-emitting diodes with large overlap quantum wells," *Optics Express*, vol. 19, no. 14, pp. A991–A1007, 2011.

[12] E. Rangel, E. Matioli, Y.-S. Choi, C. Weisbuch, J. S. Speck, and E. L. Hu, "Directionality control through selective excitation of low-order guided modes in thin-film InGaN photonic crystal light-emitting diodes," *Applied Physics Letters*, vol. 98, no. 8, Article ID 081104, 2011.

[13] Y.-K. Ee, P. Kumnorkaew, R. A. Arif, H. Tong, J. F. Gilchrist, and N. Tansu, "Light extraction efficiency enhancement of InGaN quantum wells light-emitting diodes with polydimethylsiloxane concave microstructures," *Optics Express*, vol. 17, no. 16, pp. 13747–13757, 2009.

[14] R.-J. Xie, N. Hirosaki, N. Kimura, K. Sakuma, and M. Mitomo, "2-phosphor-converted white light-emitting diodes using oxynitride/nitride phosphors," *Applied Physics Letters*, vol. 90, no. 19, Article ID 191101, 2007.

[15] S. Nizamoglu, G. Zengin, and H. V. Demir, "Color-converting combinations of nanocrystal emitters for warm-white light generation with high color rendering index," *Applied Physics Letters*, vol. 92, no. 3, Article ID 031102, 2008.

[16] C.-C. Tsai, W.-C. Cheng, J.-K. Chang et al., "Ultra-high thermal-stable glass phosphor layer for phosphor-converted white light-emitting diodes," *IEEE/OSA Journal of Display Technology*, vol. 9, no. 6, pp. 427–432, 2013.

[17] H.-C. Kuo, C.-W. Hung, H.-C. Chen et al., "Patterned structure of remote phosphor for phosphor-converted white LEDs," *Optics Express*, vol. 19, no. 14, pp. A930–A936, 2011.

[18] INTEMATIX Report, *ChromaLit Remote Phosphor for Downlight Applications*, 2013.

[19] S. Fujita, A. Sakamoto, and S. Tanabe, "Luminescence characteristics of YAG glass-ceramic phosphor for white LED," *IEEE Journal on Selected Topics in Quantum Electronics*, vol. 14, no. 5, pp. 1387–1391, 2008.

[20] J.-S. Wang, C.-C. Tsai, J.-S. Liou et al., "Mean-time-to-failure evaluations of encapsulation materials for LED package in accelerated thermal tests," *Microelectronics Reliability*, vol. 52, no. 5, pp. 813–817, 2012.